Synthetic Aperture Radar Image Simulator for Interferometry

Lisa Shannon Wray

A dissertation submitted to the Department of Electrical Engineering,
University of Cape Town, in fulfilment of the requirements
for the degree of Master of Science in Engineering.

Cape Town, February 2001

Declaration

I declare that this dissertation is my own, unaided work. It is being submitted for the degree of Master of Science in Engineering in the University of Cape Town. It has not been submitted before for any degree or examination in any other university.

Signature of Author Signed by candidate .....

Cape Town
16 February 2001

Abstract

An interferometric synthetic aperture radar (SAR) simulator was created for the purposes of experimenting with and demonstration of the interferometric process, mission planning and radar image interpretation. The simulation method employs image statistics and terrain geometry to form a synthetic image and requires inputs of a digital elevation model (DEM), flight path description, radar parameters, a terrain classification map and temporal decorrelation factors. Output images include the following images: radar cross section, power, total coherence, temporal coherence factor, geometrical coherence factor, absolute phase, interferograms and flattened interferograms.

The simulated images are compared with actual SAR images from the European Space Agency's ERS (Earth Remote Sensing) imaging satellites to which a good correlation can be seen. The simulator's strength is in portraying regions of rocky terrain and sparse to moderate vegetation, where the geometric information provided by the terrain model is the primary contributor to the image statistics. An empirically derived backscatter model and a speckle generation program were implemented to further develop more realistic greytone and texture. Upgrades to incorporate a general flight path and a model for the receiver transfer function and other future improvements are discussed.

Acknowledgements

> Mortal as I am, I know that I am born for a day. But when I follow at my pleasure the serried multitude of stars in their circular course, my feet no longer touch the earth.
>
> —PTOLEMY

To all who have helped in the process of providing intellectual and emotional grounding while allowing my fingers/imagination/curiosity to reach beyond this pale blue dot. Special thank-yous to my UCT teachers Professor Michael R. Inggs and Dr. Andrew Boy Wonder Wilkinson. And in recognition of my fellow apprentices with starry hats and coloured dreams.

> Don't Panic!
>
> —THE HITCHHIKER'S GUIDE TO THE GALAXY

Contents

List of Figures

List of Tables

List of Symbols

a	Slant range curve index
$a(x,\eta)$	Complex independent Gaussian random variable
$a(x,y,z)$	Scattering object
A_{GR}	Ground range resolution cell area
A_{SR}	Slant range resolution cell area
$b(x,\eta)$	Complex independent Gaussian random variable
BW	Bandwidth of transmitted pulse
c	Speed of light
$c(x,\eta)$	Complex independent Gaussian random variable
dAz	Azimuth projection of slant range area A_{SR}
dx	DEM azimuth spacing
dy	DEM range spacing
dz'	Component of A_{SR} perpendicular to dx
$E\{\cdot\}$	Statistical expectation operator
f_0	Centre frequency of transmitted pulse
fe_n	Slant range distance from antenna n to point P_{fe}
G	Gain of radar
$h(x,\eta)$	SAR system point response
i	DEM range index
$\bar{I}(x,\eta)$	Expected value of SAR power image, the magnitude of the complex interferogram
j	Complex number $\sqrt{-1}$
k	Integer number of phase cycles
m	Terrain slope as a ratio

M_n	Coefficients of standard deviation backscatter equation
$n(x,\eta)$	Uncorrelated system noise
P_{far}	Power returned from target at far swath
N	Number of scatterers per pixel
$P(y,z)$	Solved point on terrain
P_{fe}	Solved point's flat earth location
P_n	Coefficients of mean backscatter equation
P_{near}	Power returned from target at near swath
P_r	Received power
P_t	Transmitted power
$\mathbf{r}(x,y,z)$	Cartesian coordinate vector
R	Slant range
s	Standard deviation
s^2	Variance
$v(x,\eta)$	Amplitude of SAR image $= \lvert\mathbf{v}(x,\eta)\rvert$
$\mathbf{v}(x,\eta)$	Complex SAR image
$\mathbf{v}'(x,\eta)$	Simulated noisy SAR image
V	Volume
$W(\cdot)$	Wrapping operator
x	Azimuth
y	Ground range
y_{swath}	Ground range extent of swath
z	Height
$\mathbf{z}(\cdot)$	Complex interferogram

α	Look angle of radar
β	Local slope angle
γ	Complex coherence
γ_{geom}	Geometrical or baseline coherence
γ_{time}	Temporal coherence
γ_{SNR}	Coherence due to finite signal to noise ratio
$\delta(\cdot)$	Dirac impulse
ΔAnt	Antenna horizontal baseline
Δf	Slope induced range spectral shift

ΔR	Path difference $R_1 - R_2$
$\Delta\phi$	Interferogram phase $= \phi_1 - \phi_2 = \arg(\mathrm{z}(\cdot))$
$\Delta\phi_{fe}$	Flattened interferogram phase
ζ	In zero Doppler plane, the coordinate parallel to the approximated plane wave
η	In zero Doppler plane, coordinate perpendicular to ζ
$N()$	Normal distribution
θ	Incident angle
λ	Carrier wavelength
μ	Mean
π	Pi, 3.14159...
σ^0	Backscatter coefficient
$\sigma^0_{mean}(\theta)$	Empirically derived mean backscatter coefficient
σ	Radar cross section
σ_v	Radar cross section per unit volume
ϕ	Wrapped phase
φ	Absolute phase

Nomenclature

Across Track Repeat Pass Interferometry—Method based on two image acquisitions of the same scene from slightly displaced orbits of a satellite or aircraft.

Azimuth—Distance in a horizontal plane, parallel to the ground track.

Backscatter Coefficient (σ^0)—The expected value of the backscattered power normalised with respect to area.

Coherence—Statistical correlation between any two points or images.

Endian—Refers to the order in which computers store bytes of information.

Ground Range—The perpendicular distance from the ground track to a given object on Earth's surface.

Ground Track—Path of radar projected to the horizontal plane.

Interferometer—Device such as an imaging radar that uses two different paths for imaging, and deduces information from the coherent interference between the two signals.

Interferometric Synthetic Aperture Radar (InSAR)—A technique involving phase measurements from successive aircraft or satellite SAR images to infer differential range and range changes for the purpose of detecting very subtle changes on or of the earths surface with unprecedented scale, accuracy and reliability.

Layover—Effect of side looking radar whereby multiple target reflections are superimposed due to their equal distance to the radar.

Phase—The angle of a complex number.

Radar Cross Section (RCS) (σ)—The expected value of the backscattered power from terrain to sensor.

Radar Phase—A property of a periodic phenomenon, for example a wave, referring to its starting point or fractional advancement relative to an arbitrary origin.

Slant Range—The distance measured along a line between the radar antenna and the target.

Shadow—Effect of side looking radar image whereby regions of terrain are hidden from the radar due to the terrain and radar geometry.

Synthetic Aperture Radar (SAR)—A signal-processing technique for improving the azimuth resolution beyond the beamwidth of the physical antenna actually used in the radar system. This is done by synthesizing the equivalent of a very long side-looking array antenna.

Swath—The area on earth covered by the radar signal.

Zero Doppler—Angle of radar transmission which results in no relative motion between the imaged point and the radar. When observing stationary targets, the angle is perpendicular to the radar velocity vector.

Chapter 1

Introduction

In the past ten years, the remote sensing community has benefitted greatly from the launch of no less than seven synthetic aperture radar (SAR) imaging satellites [15], inciting much research in the academic, public and private sectors. This branch of radar is currently the essential imaging process used for radar remote sensing.[18]

SAR is an imaging process capable of producing high resolution images of planetary terrain. The frequencies of operation cover three decades of range from low VHF band (100 MHz) on airborne platforms to X band (10 GHz) and Ka band (35 GHz) on satellite sensors. Many aspects of the environment can be monitored including paths of creeping glaciers, sudden land subsidence, oceanographic trends, patterns of deforestation, reforestation and urbanisation viewed remotely from airborne or satellite platforms [15]. SAR is an all-weather all-day instrument as it is largely unaffected by clouds or precipitation and provides its own illumination. The high resolution capability makes SAR a valuable imaging technique, offering resolution on the order of tens of metres [6].

Interpreting SAR images presents a unique problem. Radar images are formed by virtue of their own illumination and use the range from sensor to target to form an image. Radar leads to distorted features especially in non-flat terrain regions. For example mountain ranges appear heavily distorted on both slopes; showing brightly illuminated areas foreshortened in length and leaning sharply to one side and dark shadowed extended areas on slopes away from the radar. In addition to image interpretation, it is helpful to know in advance the ramifications of the satellite imaging parameters to ensure imaging of the desired ground area and the

minimisation of radar shadows and regions of extreme foreshortening or layover. Costly errors can be prevented by selecting an appropriate imaging setup. These two requirements; image interpretation and system parameter selection, are aided through the use of a radar simulation program.

1.1 SAR Simulators in the Literature, 1974 - 1998

In preparation for and as a result of the many imaging SAR systems both in design and operation many institutions have developed their own in-house SAR simulators.

SAR image simulation tools have aided engineers and scientists in many ways including:

- selecting an optimum acquisition mode from a suite of sensor and viewing options prior to purchasing a costly scene [14]
- understanding the effect of illumination angle and terrain relief on SAR images [12]
- testing and optimising interferometric SAR (InSAR) processing algorithms [31]
- modelling the forward problem[1] which lends insight to the more common inverse problem[2] [10][11]

A complete simulator would model the complete SAR process, including the radar transmitter and receiver, the operation of a signal processor and the production of a radar image. However, most currently existing simulators address only a particular aspect of the whole process, according to the needs of a specific application. It is not surprising that such a wide variety of applications should spawn an equal extent of implementations. These implementation types will be described with emphasis on function, input parameters and output results.

[1] Forward problem: given a radar and some terrain to be imaged, what received signals are expected.

[2] Inverse problem: given the received signals, reconstruct the terrain observed.

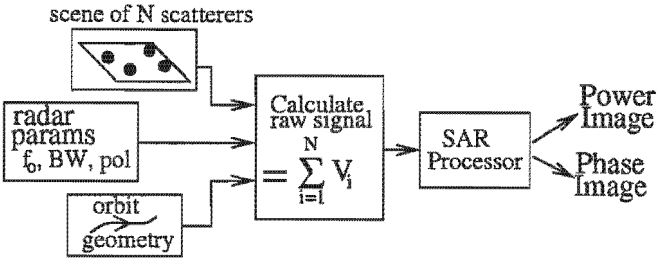

Figure 1.1: System Simulator / Coherent System Simulator Block Diagram

1.1.1 Simulator Types

The current classification scheme for simulator types was introduced by Marconi [19]. Leberl also uses this classification structure but uses different nomenclature [18]. The types will be given as *Marconi's notation/Leberl's notation* followed by a description, a simple system block diagram and some specific cases of successful implementation.

Type 1: System Simulator / Coherent System Simulator

This is a complete end to end mathematically rigorous model of the entire radar imaging process which takes an arrangement of point targets, computes the raw SAR signal and processes the final signal through an internal SAR processor as described by Figure 1.1. This model focuses on an accurate representation of the scene's reflectivity function. This can include terrain electromagnetic properties, frequency and polarisation parameters and small- or large-scale statistics.

This is a useful type for testing scattering models, experimenting with fine details of the backscatter model and gaining a thorough understanding of the Herculean task of processing SAR signals. Examples of system simulators are Franceschetti et al's SARAS raw signal simulator [11], and their later version for modelling the ocean surface [10].

Type 2: Product Simulator / Incoherent System Simulator

The principle difference between the system simulator of Figure 1.1 and the product simulator of Figure 1.2 is the replacement of the raw signal generator and

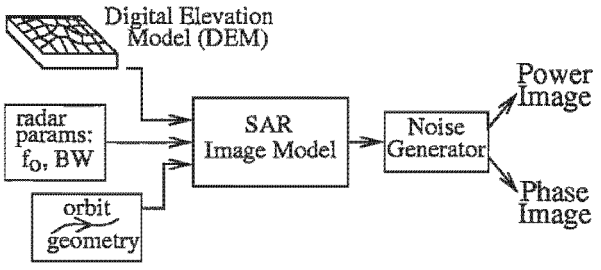

Figure 1.2: Product Simulator / Incoherent System Simulator Block Diagram

SAR processor sections with a SAR image model for computing image statistics and terrain geometry. There is a trade-off between simplicity of the product simulator and the accuracy of the system simulator. Product simulators include Gelautz's image simulator [12] with a special regard to layover areas, and Guindon's SARPLAN simulator [14] which produces an image as seen by the ERS, JERS and Radarsat sensors to aid in selection of the most suitable parameters. The Kansas simulator by Holtzman et al [16], is of this type, with attention paid to the development of an exacting backscatter model for more realistic power images.

Type 3: SAR Image-Based Simulator

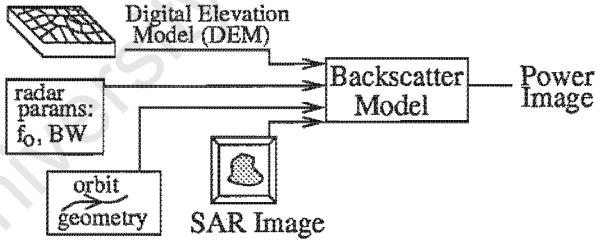

Figure 1.3: Image - Based Simulator Block Diagram

SAR image-based simulators[3] are sometimes noted as a subset of Type 2, the product simulator. Using statistics from an actual SAR image, simulated images of an alternate viewing configuration is created. Some successful implementations of this type include:

[3] Marconi and Leberl use the same notation here.

- Domik's generation of a power image from a descending orbit using an image from the ascending orbit and a DEM of the covered terrain [7].
- Xu and Cumming's method of producing a slave complex image from a master image with special attention paid to the application of receiver noise and speckle to the interferograms and the ability to independently control the contribution of each noise source [31].

1.1.2 Selected Simulator Type

Considering the available ingredients for a simulation to be a DEM, radar parameters, orbit geometry, and the anticipated products to be power images, interferograms, coherence products, and no capability to incorporate a SAR processor, the product simulator was chosen for this application. This method allows interferometric images to be formed with minimum complexity yet reasonable accuracy.

1.2 Project Goals

It is desired to create an interferometric SAR simulator to incorporate a DEM, flight trajectory information, and radar parameters and output realistic interferometric slant range SAR images including:

- power images: showing variations in the radar cross section
- interferogram due to changing terrain: showing the difference between the individual phases as viewed from each antenna
- coherence map: showing normalised cross correlation of the antenna's two views of the terrain
- shadow map: a binary map highlighting pixels hidden from the sensor
- layover map: indicating the number of superimposed regions of terrain that are mapped into each slant range pixel
- two complex SAR images: the correlation properties are determined partly by the geometrical properties of the scene and by the time correlation and

receiver signal to noise ratio parameters. These images can serve as inputs to an InSAR processor.

1.2.1 Some Notes on the Program Structure

The software program is robust, easy to use, adaptable if needed while offering a range of input parameters. The input and output files conform with the guidelines set in Appendix C in order to interact with other interferometric software modules under construction.

The SAR simulator uses the IDL language for use on the UNIX platform. However it would be simple enough to adapt the code for a Windows-compliant version, making some simple changes to platform-specific commands dealing with directory manipulation.

The simulator is a command line program that uses an unformatted floating point digital elevation model (DEM), a few ASCII user parameter files, and output unformatted data image files. Separate header files to easily interpret the image files are also produced, these conform with the standard header file format adopted by the RRSG (Radar Remote Sensing Group) of the Department of Electrical Engineering. An text log file is also produced containing all input parameters and calculated image statistics which can be seen in Appendix D. Performance can be judged by speed, processor memory usage, and/or accuracy. All were taken into account, and efficient programming methods were introduced to reduce time and memory spent.

1.2.2 Interfacing with Other Software

A library of interferometric software modules is planned for use within the RRSG including a phase unwrapping module and a DEM creation module. As the simulator forms an integral part of this library, it will conform to standard inputs and outputs set by the group.

1.3 Test Data

To simulate real-looking images, one must posses the necessary input DEMs and either real images for comparison or prior knowledge of expected real image characteristics. Luckily all are available for the chosen two test sites.

1.3.1 Site 1 - Cape Region, South Africa

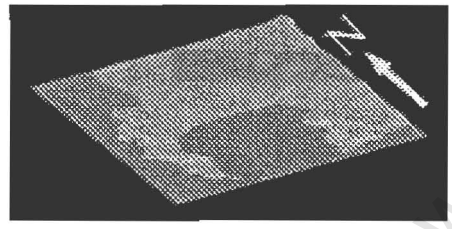

Figure 1.4: 3D view of the Cape region DEM, the ocean areas are coloured dark grey.

This DEM covers a portion of South Africa; 18°10′E, 34°30′S to 19°10′E, 33°30′S. The Cape Peninsula juts out west and south from the mainland, and the Cedarberg Mountains appear to the northeast of the DEM as seen in Figure 1.4. The peninsula has a rocky, hilly coastline with the urban sprawl of Cape Town joining it to the mainland. This DEM, provided by INSERT BENEFACTOR HERE, is 77 km x 72 km with a ground range resolution of 100 m x 100 m. This DEM covers the gamut of ecological surfaces: urban, meadowlands, rocky cliffs, sea, mountains, beaches. Satellite images taken by the European Space Agency's ERS-2 (European Remote Sensing) satellite are available for comparison with simulated images.

1.3.2 Site 1 - Katse Reservoir, Lesotho

This reservoir is located at 28°29′E, 29°20′S in the Tolkienesque alpine country of Lesotho on the southern African continent and is a region of active research within the RRSG [8]. This is due to an ongoing study of the deformation of the earth's crust resulting from the recent filling of a reservoir. The available DEM provided by the South African Air Force covers 12 km by 12 km with a

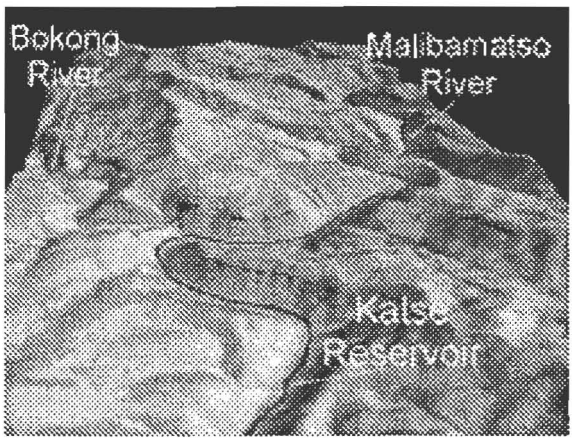

Figure 1.5: 3D view of Katse reservoir, derived from a digital elevation model. North is up in this figure. Image courtesy G. Doyle.

resolution of 25 m x 25 m. A three dimensional model formed from the DEM is shown in Figure 1.5 where the confluence of the Bokong river from the northwest and the Malibamatso river from the northeast can be seen. The terrain in this region consists of rivers, vegetated mountain slopes and sparsely vegetated rocky mountain peaks. ERS-1/2 satellite images have been acquired and are suitable for comparison to simualted data.

It is important to note that the DEMs both for the Cape Peninsula and the Katse Reservoir represent the height of the soil or rock on Earth's surface *excluding* vegetation and man made objects.

1.4 Outline of Thesis

The remainder of this thesis is organised in such a manner:

Chapter 2 mathematically models the geometrical transformation from a terrain of point sources to a complex signal representative of the output of the radar. Terrain is described in terms of distributions of point targets. The geometric conversion model from ground to slant range is discussed, with attention to the particular quirks of slant range imaging. Models for both SAR and InSAR are developed with a brief diversion into flight trajectory models.

Chapter 3 deals with radar image statistics; why the image looks the way it does

and how to characterise and simulate a statistically correct image. The product of the model described in Chapter 2, the complex interferogram, can be used to form amplitude, intensity and phase images. An empirical radar backscatter model is adopted for the accurate portrayal of greytones. Generation of speckle is described. Geometrical aspects of phase calculations and the removal of the component due to Earth are reviewed. Finally, the ground range to slant range conversion algorithm is explained.

Chapter 4 demonstrates how the software model adheres to the theoretical SAR model given in Chapter 2 and shows which subprogram accomplishes which mathematical task. The program is then introduced in a black box fashion and both the input and output files and formats are dilineated. The final part of the chapter can be used as an operations manual.

Simulation results are presented and compared with actual SAR images in Chapter 5. Visual simularity and image statistics are used to evaluate the success of the simulation.

Chapter 6 covers conclusions and recommendations for future work and possible upgrades to the simulator.

Appendix A contains a gallery of images simulated with the parameters outlined in Chapter 5. This section is replete with DEMs, power images, interferograms with and without the earth component, coherence and layover maps.

Examples of the two user input parameter files are included in Appendix B, with alterable fields marked in bold face type.

A sample log file is shown in Appendix C. This is the text output of the simulation process describing all input parameters, intermediate program constants, timing information and image statistics.

Appendix D contains a listing of the source code files that make up the heart of the simulator.

A CD is included which contains the simulator source code, sample DEMs and input files, and a manual on the use of the simulator.

Chapter 2

Radar Simulation Theory

A model for the SAR imaging process is developed then extended to an interferometric model. Figure 2.1 depicts the SAR imaging process as combination of passing the scattering object's reflected signal through the filter $h(x, \eta)$ representing the SAR system's point response, adding the receiver and image noise and producing a slant range SLC (single look complex) radar image.

This model for the scene, radar and SAR image is based on Balmer and Hartl's work [3] and the references therein.

2.1 SAR Imaging Model

The radar system is described by first modeling the scene as a superposition of point target returns from the a DEM's discrete grid points. This superposition is known as a distributed target. The scene then undergoes a transformation of coordinates from ground range to slant range, that is, a Cartesian system to a

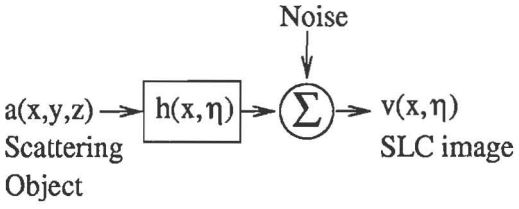

Figure 2.1: SAR imaging model.

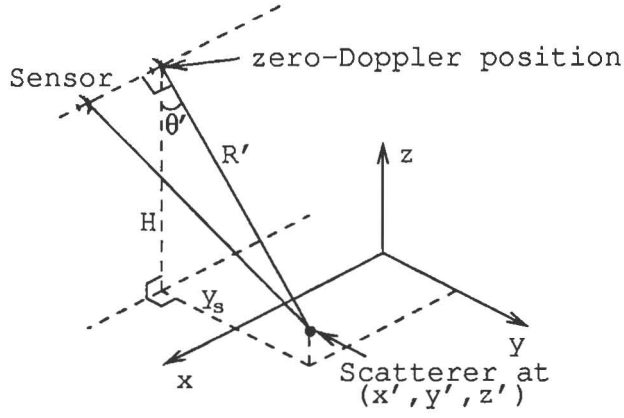

Figure 2.2: Sensor and point scatterer locations.

radar-centered cylindrical system. The returned complex signal has a magnitude that is a function of the radar cross section and a phase due to the line of sight distance between sensor and target. Some quirks inherent to side looking radar (SLR) are discussed. The imaging model is extended to include the operation of two radars operating in an interferometric mode. The products of this tandem imaging including geometric coherence and the complex interferogram are introduced.

2.1.1 Scene Model

The scene is modelled as a collection of circularly Gaussian independent random scatterers.

Point Target

Consider a point scatterer located in three dimensional space at $(x, y, z) = (x', y', z')$ as seen in Figure 2.2.

$$\delta(x - x', y - y', z - z') \tag{2.1}$$

where $\delta(\cdot)$ represents the Dirac delta distribution. It can be shown that the response of the SAR system at cylindrical coordinates $(R, \theta, z) = (R', \theta', z')$ to this point response is:

$$h(x - x', R - R') \cdot \exp(-j2kR') \tag{2.2}$$

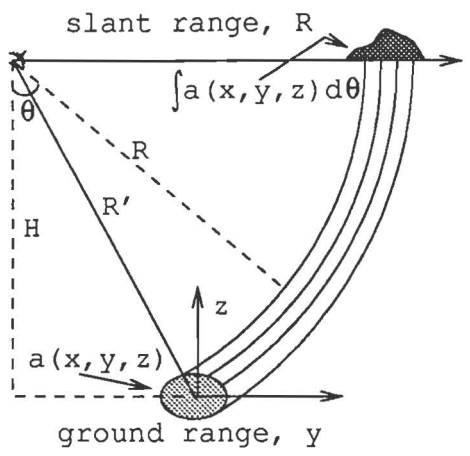

Figure 2.3: Ground range to slant range geometrical conversion.

where $h(\cdot)$ denotes the linear system response and $\exp(-j2kR')$ represents the phase due to the traversal of the distance R' from sensor to scene. The wavenumber is represented by $k = 2\pi/\lambda$, $\lambda = c/f_0$ is the wavelength of the transmitted pulse, c is the light velocity and f_0 is the centre frequency of the transmitted pulse.

Distributed Target - Collection of Point Targets

The scene to be imaged can be modelled as a collection of Gaussian independent randomly positioned point scatterers, also called a *distributed target*. From these point scatterers the scattered fields and thus their responses in the SAR image superpose linearly, excluding attenuation and multipath effects. If a high number of random scatterers are within a resolution cell of the SAR image, that is, no single scatterer remarkably dominates the others, then the SAR image pixel values will be complex circular Gaussian random variables. For remote sensing SARs the Gaussian assumption is true for most natural scatterers such as forests, farmlands or mountainous areas. In regions where only a few dominant scatterers exist such as in urban areas with artificial objects, the distributed target assumption does not apply.

2.1.2 Conversion from Ground Range to Slant Range

Let the distributed target be represented as $a(x, y, z)$ and let $\mathbf{r} = (x, y, z)^T$, the coordinate system vector, and $\mathbf{r}' = (x', y', z')^T$, the vector denoting the position of the distributed target centre. The linear operator characterising the SAR imaging process is a geometric projection of $a(x, y, z)$ from three-dimensional space into the two-dimensional cylindrical zero-Doppler coordinates (x, R) followed by a two-dimensional convolution with the point response found in Equation 2.2:

$$\mathbf{v}(x, R) = \int a(\mathbf{r}') \exp\{-j2kR'\}\, h(x - x', R - R')\, \mathrm{d}V' \tag{2.3a}$$

$$= \left[\int a(\mathbf{r})\, R\, \mathrm{d}\theta \cdot \exp\{-j2kR\}\right] \circledast h(x, R) \tag{2.3b}$$

where $\circledast$ represents convolution, $\mathrm{d}V' = dx'\, dy'\, dz'$ and $y = y_s + R\sin\theta$, $z = H - R\cos\theta$. The coordinate y represents ground range while R represents slant range. The SAR image $\mathbf{v}(x, R)$ is described in Equation 2.3a and Figure 2.3.

The SAR imaging process is defined as a convolution of the phase shifted and projected scattering object with the receiver's impulse response function. The distributed target $a(\mathbf{r})$ is projected from ground range to slant range along the θ direction; in circles of constant R. The phase component $\exp\{-j2kR\}$ due to the scatterer's distance from the sensor is applied, and the product is convolved with the receiver system response. A change from Cartesian to cylindrical coordinates is implied.

SAR Imaging Model

This model implies detection of distributed scenes, which are adequately described by their backscatter coefficient, σ^0, a measure of the expected value of backscattered power normalised by the slant range area. We now assume a plane wave approximation with reference to the SAR projection circles as seen in Figure 2.4. The ζ-coordinate is parallel to the plane wave and the η-coordinate is described by the vector from the sensor to the distributed target centre. The SAR image $\mathbf{v}(x, R)$ is now expressed as $\mathbf{v}(x, \eta)$.

The expected value of the magnitude squared SAR image is termed the pixel intensity $\bar{I}(x, \eta)$, or equivalently the received power, P_r.

$$\bar{I}(x, \eta) = P_r = \mathrm{E}\left\{|\mathbf{v}(x, \eta)|^2\right\} \tag{2.4a}$$

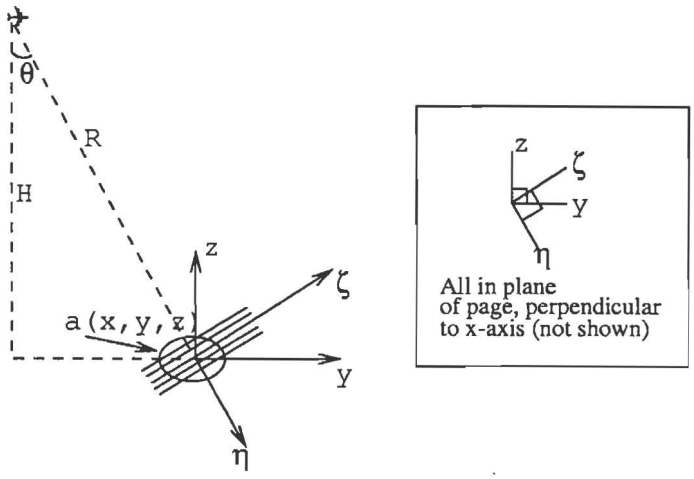

Figure 2.4: Plane wave approximation and associated approximate coordinate system for SAR image model.

$$= \left(\int \sigma_v(\mathbf{r})\, \mathrm{d}\zeta \right) \circledast |h(x,\eta)|^2 \tag{2.4b}$$

$$= \sigma(x,\eta) \circledast |h(x,\eta)|^2 \tag{2.4c}$$

where σ_v is the radar cross section (RCS) per unit volume, $h(x,\eta)$ is the transfer function of the receiver, and σ is the RCS.

Under the assumption of circular Gaussian image statistics, several conclusions can be drawn [3] [20]:

- real and imaginary parts of $\mathbf{v}$ are mutually uncorrelated
- phase and magnitude of $\mathbf{v}$ are uncorrelated

Radiometry

The returned power P_r as seen in Equation 2.4a can be viewed as a combination of system parameters, the range to the target R and the radar cross section σ: [24]

$$P_r = \left(\frac{P_t G^2 \lambda^2}{(4\pi)^3} \right) \frac{\sigma}{R^4} \tag{2.5}$$

where G^2 is the two-way gain of the antenna, and λ is the wavelength of the transmitted pulse. This equation assumes firstly that the area must be populated with

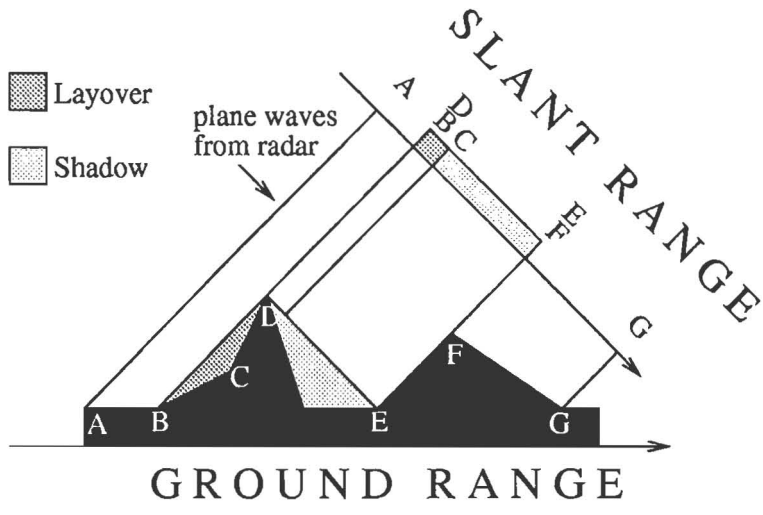

Figure 2.5: Slant range effects caused by side looking projection geometry.

distributed targets; a homogeneous region of a large number of individual scatterers in the resolution cell positioned randomly, and secondly, that all parameters of the radar equation are constant across the resolution cell.

2.1.3 Side Looking Radar Imaging Geometry and Quirks

A one-to-one mapping from ground to slant range is not always possible due to the geometry of the imaging process as illustrated in Figure 2.5.

Shadow Due to the viewing angle of the radar, parts of the terrain may be hidden from the radar's line of sight. These sections of the scene are termed *shadow* areas exemplified by the slant range region from D to E in Figure 2.5.

Layover During the process of ground range to slant range conversion, it is possible that more than one point of the scene will be at the same slant range distance from the sensor. These points will be indistinguishable from each other as they are mapped into the same SAR image pixel. These points are said to be in *layover*. For example, the point pair B, D in Figure 2.5 are at equal slant ranges as are the pair E, F. The resultant is a weighted sum of the returned power and phase contributions of each distributed target.

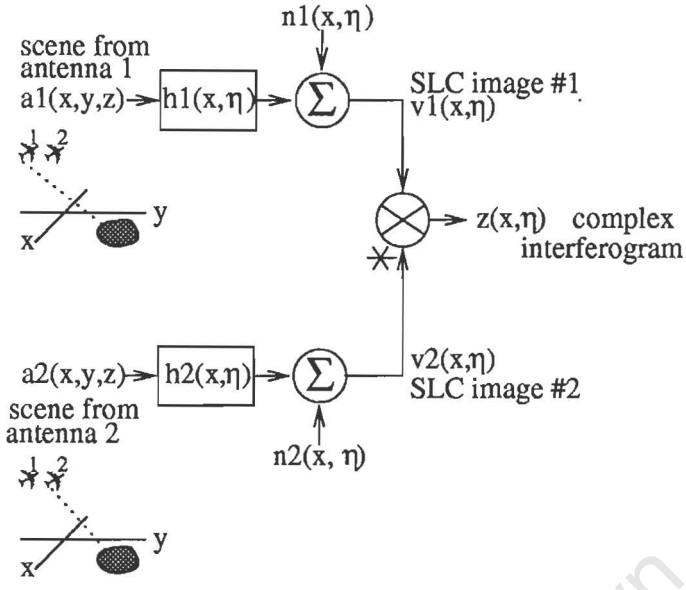

Figure 2.6: InSAR imaging model.

2.1.4 InSAR Imaging Model

Interferometry is the process of deriving more information about the scene than a single image can produce by exploiting the coherent phase interference. Within these two or more images, the varied parameters could include flight path, acquisition time or wavelength which then determines the type of interferometer. For our application of simulating two successive flybys, the flight path is varied. This is accomplished by *repeat-pass* interferometry whereby two slightly different sensor geometries produce two images of a common area.

The two images attained are:

$$\mathbf{v}_1(x,R) = |\mathbf{v}_1(x,R)| \exp\{j\phi_1(x,R)\} \tag{2.6a}$$

$$\mathbf{v}_2(x,R) = |\mathbf{v}_2(x,R)| \exp\{j\phi_2(x,R)\} \tag{2.6b}$$

the complex conjugate of these two images forms the complex interferogram, $\mathbf{z}(\cdot)$.

$$\mathbf{z}(\cdot) = \mathbf{v}_1(\cdot)\mathbf{v}_2^*(\cdot) \tag{2.7a}$$

$$= |\mathbf{v}_1(\cdot)||\mathbf{v}_2(\cdot)| \exp\{j\Delta\phi)\} \tag{2.7b}$$

The phase of $\mathbf{z}(\cdot)$, $\Delta\phi$, is the SAR image response of a point scatterer, propor-

tional to the range from the sensor.

$$\arg\left[\mathbf{z}(\cdot)\right] = \Delta\phi = \phi_1 - \phi_2 = 2k\Delta R = \frac{4\pi}{\lambda}\Delta R \tag{2.8}$$

A model for the interferometric imaging process for Gaussian scatterers is shown in Figure 2.6. Two different views of the same scattering object $a(x, y, z)$ owing to different flight paths produce the two scenes $a_1(x, y, z)$ and $a_2(x, y, z)$. The SAR systems are modeled as filters with point responses $h_1(x, \eta)$ and $h_2(x, \eta)$, and uncorrelated system noise $n_1(x, \eta)$ and $n_2(x, \eta)$ is added. The final image, $\mathbf{z}(x, \eta)$, represents the slant range complex interferogram. The expected value of the complex interferogram can be shown as:

$$\mathrm{E}\left\{\mathbf{z}(x,\eta)\right\} = \mathrm{E}\left\{\mathbf{v}_1(x,\eta)\mathbf{v}_2^*(x,\eta)\right\} \tag{2.9}$$

Image Statistics

The complex quantity, γ, can be defined as a normalised measure of the correlation between two registered SAR images.

$$\gamma = \frac{\mathrm{E}\left\{\mathbf{v}_1^*\mathbf{v}_2\right\}}{\sqrt{\mathrm{E}\left\{|\mathbf{v}_1|^2\right\}\mathrm{E}\left\{|\mathbf{v}_2|^2\right\}}} \tag{2.10}$$

$$= \gamma_{geom}\,\gamma_{time}\,\gamma_{SNR}\,\exp(j\Delta\phi) \tag{2.11}$$

This is also called the correlation coefficient and its magnitude may be computed from the product $|\gamma| = \gamma_{geom}\,\gamma_{time}\,\gamma_{SNR}$, a function of the local terrain slope, radar parameters, antenna locations and an estimate of the time decorrelation. The phase contribution is the interferometric phase due to the terrain. Individual contributions to the correlation coefficient magnitude ,$|\gamma|$, are described further.

Geometric Coherence The geometric coherence, γ_{geom}, due to the slightly different views of the two antennas and is calculated as [30]

$$\gamma_{geom} = \frac{BW - \Delta f}{BW} \tag{2.12}$$

where BW is the bandwidth of the transmitted pulse, and Δf is the slope-induced range spectral shift given by

$$\Delta f = f_0\left(1 - \frac{\sin\theta_1}{\sin\theta_2}\right) \tag{2.13}$$

where θ_1, θ_2 are the incident angles for antennas 1 and 2 respectively and f_0 is the transmitted pulse frequency.

Coherence Due to Receiver Noise The coherence due to a finite signal to noise ratio (SNR), γ_{SNR}, is

$$\gamma_{SNR} = \frac{1}{\sqrt{1+\frac{1}{SNR_1}}}\frac{1}{\sqrt{1+\frac{1}{SNR_2}}} \tag{2.14a}$$

$$\approx \frac{1}{1+\frac{1}{SNR}} \tag{2.14b}$$

where SNR_1 and SNR_2 are the signal to noise ratios in each SAR image. γ_{SNR} can be approximated as in Equation 2.14b by assuming that $SNR_1 \approx SNR_2$.

Temporal Coherence The temporal coherence, γ_{time}, represents the expected decorrelation between the two SAR images expected during the time between acquisitions. As with all coherence values, this quantity is expressed as a normalised value; between 0 and 1, with 0 representing no coherence retained between images and 1 representing complete preserved coherence. Contributions to the decorrelation of the scene involve changes in the microstructure of the scene from trees moving, waves rippling, lawns being mowed, houses falling down and so on. Temporal coherence is valid in the following region:

$$0 < \gamma_{time} \leq 1 \tag{2.15}$$

2.2 Interferometer Configuration and DEM Orientation

Interferometry involves the extraction of useful information from the coherent addition of phases from multiple target reflections. Different interferometer configurations exist according to particular applications. In the case of this simulator, modelling the reflected signal from a certain surface topology from two slightly different flight paths with an allowance for possible time decorrelation factor between each antenna pass is desired. This can be accomplished by the repeat pass across track interferometer, whereby two slightly different images are taken at different times of the same scene.

DEM Placement and Orientation

In the case of a rectilinear horizontal flight path, the geometry can be simulated using a model of the range mapping effect. Figure 2.7 shows the master antenna (antenna #1) at $(azimuth, range, height) = (x, y, z) = (0, 0, z_{A1})$ imaging a constant swath width while observing along the range direction. The sensor path is parallel with the azimuth axis. For dual antenna operation the slave antenna (antenna #2) is placed at $(0, y_{HB}, z_{A2})$ where y_{HB} is the horizontal baseline between antennas and z_{A1}, z_{A2} are the heights of the master and slave antennas respectively above the spheroidal model of the Earth. The current antenna geometry assumes both sensors are a constant azimuth distance apart.

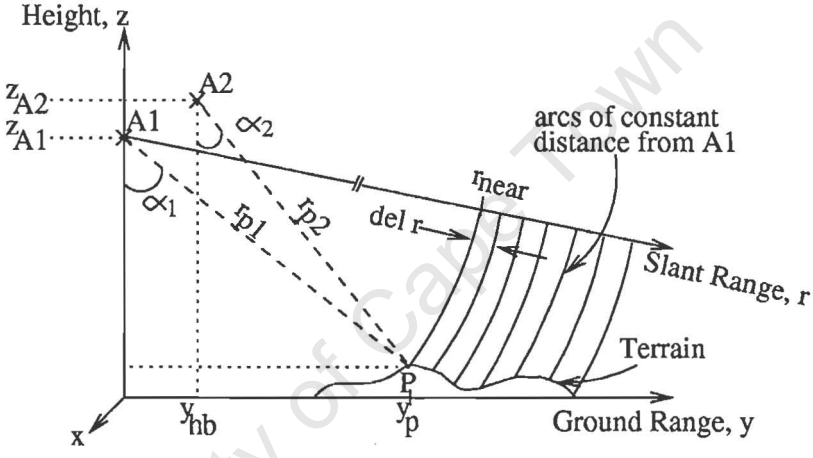

Figure 2.7: Cross section of idealised flight path perpendicular to the velocity vector.

Although images are typically simulated using an idealised straight flight path parallel to the DEM, the need may arise to model an arbitrary flight path. This is visually described in Figure 2.8. In such cases the illumination vector intersecting the DEM is determined from the sensor position and velocity vectors.

2.3 Possible Flight Trajectory Models

The two applications of the current flight trajectory model are presented with an upgrade to a more flexible future model.

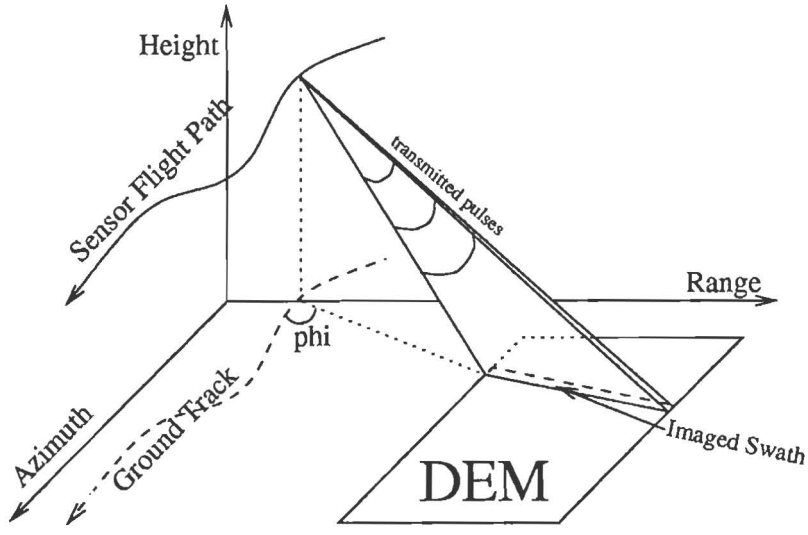

Figure 2.8: Arbitrary flight path and DEM geometry.

2.3.1 Current Model - Two Dimensional Zero Doppler Imaging

As DEMs exist in rectangular two dimensional matrices, and the imaging direction of a SAR can be approximated as in planes of constant azimuth, a logical first step is to assume a flight path of constant height and constant range from the DEM, depicted in Figure 2.9. This simplifies the analysis greatly and minimises computation.

2.3.2 Current Model with Variation - Two Dimensional Zero Doppler Imaging with Rotated DEM

A flight direction angled to the azimuth axis can be approximated by rotating the DEM instead, and reverting to the setup algorithms for the zero Doppler imaging geometry. As mentioned, this is an approximation due to the discrete nature of the DEM, for when rotated produces finite errors and distortions of previously straight rows. This effect is remarkable on a small scale as in Figure 2.10 but decreases in significance as the pixel size becomes much smaller than the overall rotated image size.

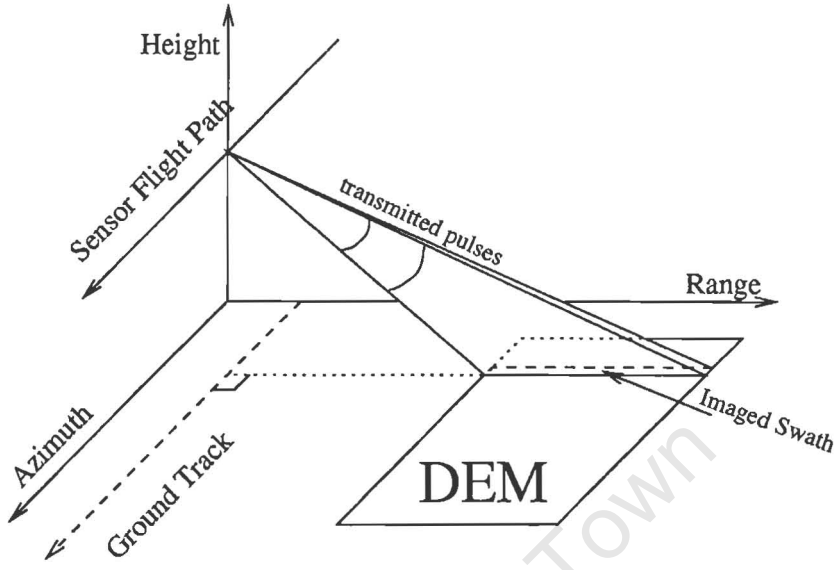

Figure 2.9: Idealized straight line flight path and DEM geometry.

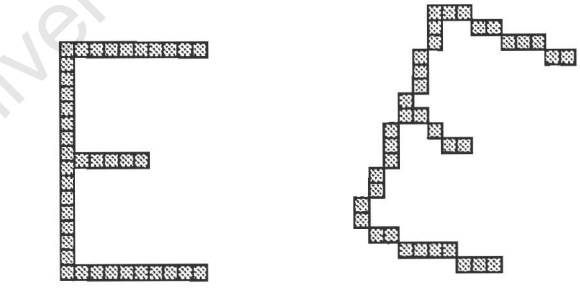

Original Discrete Object

Discrete Object Rotated by 20°

Figure 2.10: Distortion effects on a rotated discrete image.

2.3.3 Future Model - Three Dimensional Imaging Model

A more correct method of simulation a variable-range flight path would be one which projects a arbitrarily angled perpendicular swath across the terrain model and interpolates between terrain samples for each piecewise portion of the flight path as can be seen in Figure 2.8.

This model places no restrictions on the path of the sensor, that is, variations in latitude, longitude and height are allowed. This is the most correct model for flight path designation and would accept a number of discrete sensor positions. Discrete times and velocities (of which distance information can be derived) are commonly used to depict flight paths of current satellite imaging radars such as ERS-1/2. Interpolation between sensor positions using linear, cubic or spline methods could be used.

Chapter 3

Fundamental Properties of SAR Images

The primary geophysical quantity determining SAR data is the complex radar reflectivity of the scene and the SAR provides a measurement of this complex value $\mathbf{v}(x,\eta)$. The slant range image's azimuth and range coordinates are x and η respectively. Refer to Figure 2.6 for a reminder of the notation. Qualitatively, this concept expresses the fact that when an electromagnetic wave scatters from the slant range position (x,η), the physical properties of the terrain cause changes in both the phase $\phi(x,\eta)$ and amplitude $v(x,\eta)$ of the wave. The SAR measures the in-phase and quadrature (I and Q) channels of the receiver, weighted by the SAR's point spread function. This estimate of the local reflectivity at each pixel can also be represented by the complex number $ve^{j\phi}$. In this form, the SAR data are known as the complex image (SLC)[20].

$$\mathbf{v} = v_I + jv_Q = v\cos\phi + jv\sin\phi \tag{3.1a}$$

$$= ve^{j\phi} \tag{3.1b}$$

From the single SLC image, the ampliftude image, v, the phase, ϕ, and the power image, v^2, can be derived. For interferometric applications, two or more SLC images are used to form the complex interferogram, $\mathbf{z}(x,\eta)$. For simplicity, only two SLC images, $\mathbf{v}_1$ and $\mathbf{v}_2$, modelling the images seen from two radar locations will be used.

$$\mathbf{z} = \mathbf{v}_1\mathbf{v}_2^* \tag{3.2a}$$

$$= \mathbf{v}_1\mathbf{v}_2 e^{j(\phi_1-\phi_2)} \tag{3.2b}$$

From the complex interferogram $\mathbf{z}$, the following images can be obtained: the magnitude of the complex interferogram, $|\mathbf{v}_1\mathbf{v}_2^*|$ and the interferogram phase $(\phi_1 - \phi_2)$.

3.1 Simulation of SAR Amplitude Images

This section deals with the process of creating the magnitude of the complex interferogram, $|\mathbf{z}|$. Simulation of $|\mathbf{z}|$, is a two step process; calculate the radar cross section values, $E\{|v_n|^2\}$, then apply a speckle application model to obtain $|\mathbf{z}|$.

$E\{|v_n|^2\}$ or Radar Cross Section (RCS) Image Determine the RCS values for each image pixel (x, η) and form an 8-bit greyscale image. The greytones will reveal the terrain contours.

Magnitude of the Complex Interferogram, $|\mathbf{z}|$ To the existing RCS image $E\{|v_n|^2\}$, apply a receiver noise model to obtain $|\mathbf{z}|$. See Figure 4.2 for details.

The magnitude of the complex interferogram $|\mathbf{z}|$ is formed by incorporating the radar cross section values to determine the correct mean and variance for each I and Q channel of the two SLC images. The calculated mean and variance are then used to generate "noisy" I and Q data and thus a SLC image with the correct noise-like appearance and distribution is formed as seen in the centre of Figure 3.1. Compare this with the actual power image on the right and the clean "first approximation" RCS image on the left.

3.1.1 Radar Backscatter Image

As mentioned in the *SAR Imaging Model* section in Chapter 2, Equations 2.4a to 2.4c relate the radar cross section σ to the intensity or power image. The radar cross section is directly proportional to $E\{|v_n|^2\}$ which is seen mathematically in Equation 3.3a and visually in Figure 3.1.

$$\bar{I}(x,\eta) = \mathrm{E}\left\{|\mathbf{v}(x,\eta)|^2\right\} \propto \sigma(x,\eta) \tag{3.3a}$$

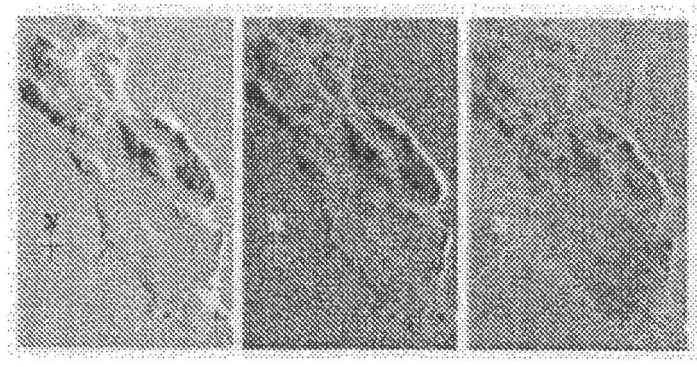

Figure 3.1: SAR amplitude images of the southern Cape Peninsula. L to R: simulated radar cross section, simulated magnitude of complex interferogram, actual ERS single SLC power image. Simulation parameters: C-band, VV-polarisation, 23 degree mid-swath incident angle, antenna height 785 km.

Digression on the Development of a Radar Backscatter Model for Simulation of ERS Images

For the radar backscatter model, initially a basic scattering model was implemented dependent solely on the local slope; the slope of the terrain on a scale comparable to the DEM spacing. This model was upgraded to one which takes into account local slope, transmitted pulse frequency, polarisation mode and the area of the slant range resolution cell. The new model was evaluated by virtue of its versatility and ability to adequately mimic actual SAR images.

Radar Equation The power returned to a radar is given by the following equation:

$$P_r = \frac{P_t G^2 \lambda^2}{(4\pi)^3 R^4} \sigma \tag{3.4a}$$

$$= K\sigma \tag{3.4b}$$

as echoed in Equation 2.5. This equation assumes firstly that the area must be populated with distributed targets, that is, a homogeneous region of a large number of randomly positioned individual scatterers in the resolution cell. It is with the radar cross section σ that we are concerned and can lump the rest of the parameters in Equation 3.4a into a constant K over the imaged swath.

The RCS may be further subdivided into sigma nought (σ^0), the unit-less backscatter coefficient, and A_{GR}, the ground range resolution cell area in units of m^2. A_{GR} can be seen in Figure 3.2

$$\sigma = \sigma^0 A_{GR} \tag{3.5}$$

The multiplication of σ^0 and A_{GR} result in σ, the average power returned from a resolution cell.

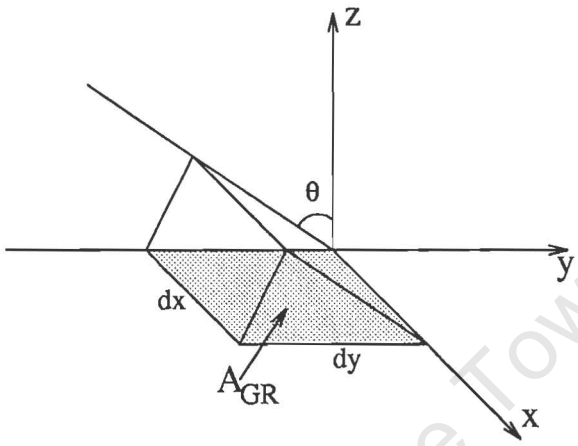

Figure 3.2: Representation of ground range resolution cell area A_{GR}.

Theoretical Scattering Models for Sigma Nought Theoretical models provide a value for sigma nought based on a mathematical description of both the scattering surfaces and the incident radar pulse, and calculate the expected backscattered power using these models. To date, theoretical models are very restrictive in their applicability to generalised surfaces and are computer- and patience-intensive [27], and were not tested for these reasons.

Empirical Scattering Model for Sigma Nought A compilation of empirical scattering models can be found in [27], containing an extensive database relating the backscatter coefficient to terrain type, frequency, polarisation and local incident angle. For each terrain type, frequency, and polarisation, the backscatter coefficient is given in terms of local incident angle, θ. This is the angle between the surface normal vector and the direction to the radar, hence the angle varies with terrain slope. Equations were fitted to the database on an

Table 3.1: Available terrain types for power image backscatter model.

Type A	Soil and Rock
Type B	Grasses
Type C	Shrubs
Type D	Short Vegetation
Type E	Dry Snow
Type F	Wet Snow

exponential and cosine relationship of the form:

$$\sigma^0_{mean}(\theta) = P_1 + P_2 \exp(-P_3\theta) + P_4 \cos(P_5\theta + P_6) \tag{3.6}$$

where θ is in radians and σ^0_{mean} is unit-less, although measured logarithmically, hence the units of dB. Equation 3.6 represents the mean backscatter, the standard deviation of the data was also computed and modelled as:

$$s(\theta) = M_1 + M_2 \exp(-M_3\theta) \tag{3.7}$$

where $s(\theta)$ is the standard deviation of σ^0_{mean} in dB and θ again in radians.

The coefficients P_1 to P_6 are available for a certain choice of frequency, polarisation and terrain cover type. Since the majority of the simulations in this thesis are of images from the European Space Agency's ERS instruments which work at 5.3 GHz (C-band) and VV polarisation, those parameters were chosen.

The terrain cover types are categorised as: soil and rock, trees, grasses, shrubs, short vegetation, road surfaces, urban areas, dry snow and wet snow. The categories trees, road surfaces and urban areas are not supplied for C-band frequencies and VV polarisation so they were not studied. The resulting types are listed in Table 3.1.

Sigma nought varies with incidence angle, surface roughness and soil moisture levels. The angular dependence is treated in the mean backscatter calculation in Equation 3.6. Each type has a characteristic average particle size, average moisture value and average vegetation content all of which influence the reflected power.

The plotted backscatter coefficient σ^0 as a function of θ plotted in Figure 3.3 is valid for $0° \leq \theta \leq 80°$. There is a high correlation between the non-snow terrain curves. The three classes of vegetation, namely types B, C and D; grasses, shrubs

Table 3.2: Recommended empirical backscatter model coefficients for C-band VV-polarisation radar.

Coefficient	Value
P1	-88.593
P2	99.000
P3	0.326
P4	9.574
P5	1.969
P6	-3.142
M1	2.287
M2	3.330
M3	2.674

and short vegetation, have almost identical backscatter characteristics which is not surprising given their similar composition. For angles up to 40° the soil and rock category behaves like the vegetation types. This could be due to similar roughness scales or moisture levels. The snow reflects very little energy towards the sensor at high incident angles, it seems to behave like a specular surface, which makes sense as snow is generally very smooth even at short wavelengths.

Since the backscatter curves for the vegetated areas are quite similar, any one of Types A through D would suffice, so Type D was chosen for implementation. The coefficients for Equation 3.6 for Type D are given in Table 3.2.

Implementation and Analysis of Ulaby's Vegetation Model The simulator was run with the chosen backscatter model to create a realistic SAR image which when compared with actual ERS images showed correlation in that they agree where the low-correlation areas are, yet disagree on the absolute value of the correlation values. This can be seen from the results in Chapter 5.

Recommendation for Simulator's Backscatter Model Ulaby's model for short vegetation can be used over most land cover with good results. It is not useful for imaging ocean nor urban areas as the ocean has a constantly varying small scale structure, and the urban areas are too complex to be accurately modeled with a coarse DEM.

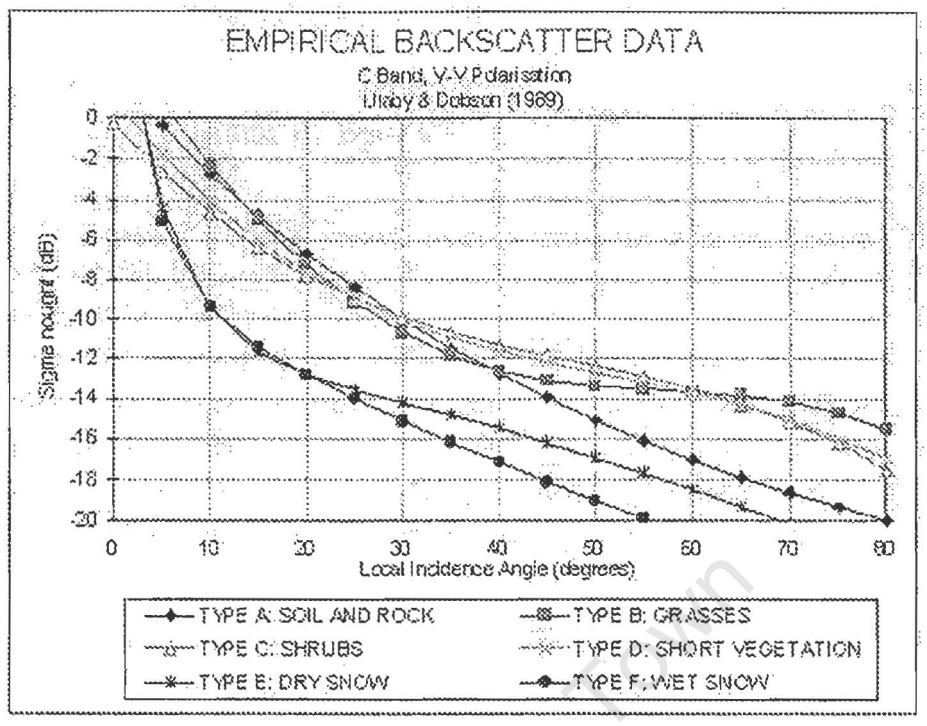

Figure 3.3: Angular dependence of sigma nought (backscatter coefficient) for various terrain types using the Ulaby and Dobson empirical models.

3.1.2 Application of Speckle

The noise-like quality characteristic of all coherence imaging systems is known as speckle. Speckle is an interference phenomenon in which the principle source of the noise-like data is the distribution of the phase terms ϕ_k. Since each simulated pixel is many wavelengths across, scatterers at different parts of the pixel will contribute very different phases to the return even if their scattering behaviour is identical. Each slant range pixel of the SLC is the superposition of many scatterers as seen in Equation 3.8. The sum $ve^{j\phi}$ is described as [20] a random walk in the complex plane, where each step of length v_k is in a completely random direction.

$$ve^{j\phi} = \sum_{k=1}^{N} v_k e^{j\phi_k} \tag{3.8}$$

Initial Assumptions

Table 3.3: Radar simulation parameters for testing the backscatter model.

Parameter	**Value**
Operating Frequency	5.3 GHz
System Bandwidth	15 MHz
SAR Incident Angle	23° at mid-swath
Slant Range Resolution	8m x 24m (range x azimuth)
DEM Resolution	100m

- the number of scatterers, N, per pixel is very large
- the scatterers within each pixel are statistically identical, that is, no one scatterer dominates.

The following procedure for generation of complex speckle images is attributed to the work by A.Wilkinson [28], A. Amit [2] and Goldstein et al [13]. The noisy SLCs $\mathbf{v}_1$ and $\mathbf{v}_2$ can be modelled as complex Gaussian random variables [20]. Thus they can be modelled as a sum of complex independent Gaussian random variables; a, b, c.

$$\mathbf{v}_1 = a(x,\eta) + c(x,\eta) \tag{3.9a}$$
$$\mathbf{v}_2 = b(x,\eta) + c(x,\eta) \tag{3.9b}$$

$$a = a_I + ja_Q \tag{3.10a}$$
$$b = b_I + jb_Q \tag{3.10b}$$
$$c = c_I + jc_Q \tag{3.10c}$$

The means, μ, and standard deviations, s, of the random variables a, b, c are as follows.

$$\mu_{AI} = \mu_{AQ} = \mu_{BI} = \mu_{BQ} = \mu_{CI} = \mu_{CQ} = 0 \tag{3.11}$$

$$s_{AI} = s_{AQ} = s_{BI} = s_{BQ} \tag{3.12a}$$
$$s_{CI} = s_{CQ} \tag{3.12b}$$

The random variables a and b are independent and correlated, whereas a and c are independent and uncorrelated. The degree of correlation will be related to

$|\gamma|$ the magnitude of the coherence.

$$E\{\mathbf{v}_1\mathbf{v}_2^*\} = E\{(a+c)(b+c)^*\} = E\{|c|^2\} \tag{3.13}$$

$$\begin{aligned} E\{|\mathbf{v}_1|\} &= E\{|a|^2\} + E\{|c|^2\} && (3.14a)\\ &= E\{a_I^2 + a_Q^2\} + E\{c_I^2 + c_Q^2\} && (3.14b)\\ &= s_{AI}^2 + s_{AQ}^2 + s_{CI}^2 + s_{CQ}^2 && (3.14c)\\ &= 2s_{AI}^2 + 2s_{CI}^2 && (3.14d)\\ &= 2s_{BI}^2 + 2s_{CI}^2 = E\{|\mathbf{v}_2|\} && (3.14e) \end{aligned}$$

Relating these variables to the common definition for correlation, $|\gamma|$

$$\begin{aligned} |\gamma| &= \frac{E\{\mathbf{v}_1\mathbf{v}_2^*\}}{\sqrt{E\{|\mathbf{v}_1|^2\}E\{|\mathbf{v}_2|^2\}}} && (3.15a)\\ &= \frac{E\{|c|^2\}}{E\{|a|^2\} + E\{|c|^2\}} && (3.15b) \end{aligned}$$

It can be shown that the expected value of $|c|^2$ is equal to $2s_{CI}^2$.

$$E\{|c|^2\} = E\{c_I^2 + c_Q^2\} = s_{CI}^2 + s_{CQ}^2 = 2s_{CI}^2 \tag{3.16}$$

Similarly the expected value of $|a|^2 = 2s_{AI}^2$. Combining Equations 3.14d, 3.15b and 3.16 leads to:

$$\begin{aligned} |\gamma| &= \frac{s_{CI}^2}{s_{CI}^2 + s_{CQ}^2} && (3.17a)\\ E\{|\mathbf{v}_i|\} &= 2s_{AI}^2 + 2s_{CI}^2 && (3.17b) \end{aligned}$$

Thus given the magnitude of the complex coherence, $|\gamma|$, and the radar cross section, $E\{|\mathbf{v}_i|^2\}$, the variances s_{AI}^2 and s_{CI}^2 can be solved using Equations 3.17a and 3.17b.

$$\begin{aligned} s_{CI}^2 &= \frac{|\gamma|\ E\{|\mathbf{v}_i|^2\}}{2} && (3.18a)\\ s_{AI}^2 &= \frac{E\{|\mathbf{v}_i|^2\}}{2} - s_{CI}^2 && (3.18b) \end{aligned}$$

Six Gaussian distributed random images, $a_I, a_Q, b_I, b_Q, c_I, c_Q$ are generated by multiplying a two dimensional array of Gaussian distributed random variables with zero mean and standard deviation of one by the square root of the calculated variance.

$$a_I(x,\eta) = N(\mu = 0, s = 1)\sqrt{s_{AI}^2(x,\eta)} \tag{3.19}$$

The SLC images with the interferometric phase are formed as follows:

$$\mathbf{v}_1' = [(a_I + c_I) + j(a_Q + c_Q)]\,[\cos(\phi_1 - \phi_2) + j\sin(\phi_1 - \phi_2)] \quad (3.20a)$$

$$\mathbf{v}_2' = [(b_I + c_I) + j(b_Q + c_Q)] \quad (3.20b)$$

$$\mathbf{z} = (\mathbf{v}_1')(\mathbf{v}_2')^* \quad (3.21)$$

The noisy power image $|\mathbf{z}|$ and the noisy interferogram phase $\arg(\mathbf{z})$ are thus formed. A third noisy SLC $\mathbf{v}_3'$ was also formed with the phase equal to the flattened interferogram phase.

3.2 Simulation of SAR Phase Images

The argument of the complex interferogram is known as the phase ϕ. The phase is proportional to slant range distance between the radar and imaged terrain scatterer and is expressed as a value in the region of $(-\pi, \pi]$. The phase may be expressed with or without the high frequency fringe pattern due to the phase contribution of the geoid. The former is known as the phase, and the latter as the "flattened phase".

3.2.1 Geometry Behind Phase Calculations

The interferogram phase is a function of the difference of the two slant range distances R_1 and R_2 from the two radar positions A_1 and A_2 as defined in Figure ??.

$$\Delta\phi = \phi_1 - \phi_2 = \frac{4\pi}{\lambda}(R_1 - R_2) \quad (3.22)$$

The flattened interferogram phase has the "flat earth" component removed, that is, for the solved point P, the distance from the radar positions to the point P_{fe}.

$$\Delta\phi_{fe} = \frac{4\pi}{\lambda}(R_1 - R_2 - (fe_1 - fe_2)) \quad (3.23)$$

From ordinary trigonometry, fe_2 can be shown to be:

$$fe_2 = \sqrt{z_2^2 + (\sqrt{fe_1^2 - z_1^2} - \Delta Ant)^2} \quad (3.24)$$

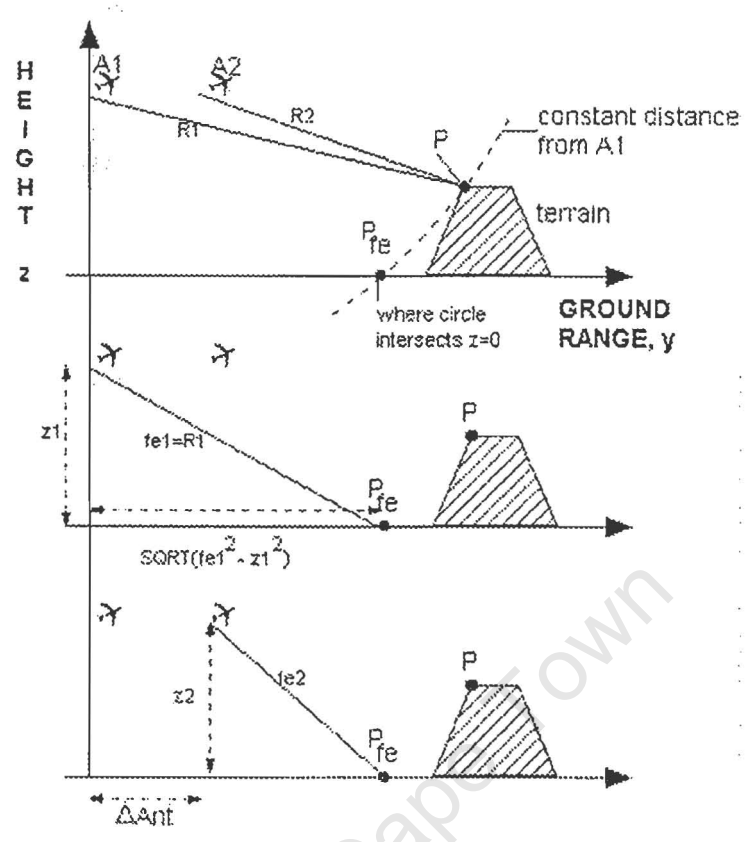

Figure 3.4: Height-ground range analysis of flat earth phase calculations.

3.3 The Geometric Solver Subprogram

The radar cross section and the phase images are produced along with the coherence and flat earth calculations in the subprogram known as the geometric solver. There are two main purposes of the solver subprogram, solver.pro. The primary function is to transform the scene described by the digital elevation model from ground range coordinates (azimuth, ground range, height) $= (x, y, z)$ into slant range coordinates (azimuth, slant range, height) $= (x, R, z)$ as displayed in Figure 3.5. The secondary function is to use the transformed slant range points to build up radiometric and geometric images such as interferometric phase, coherence, reflected power and other interpretive maps.

See Figures 3.9 and 3.10 for the flowchart of the geometrical solver subprogram.

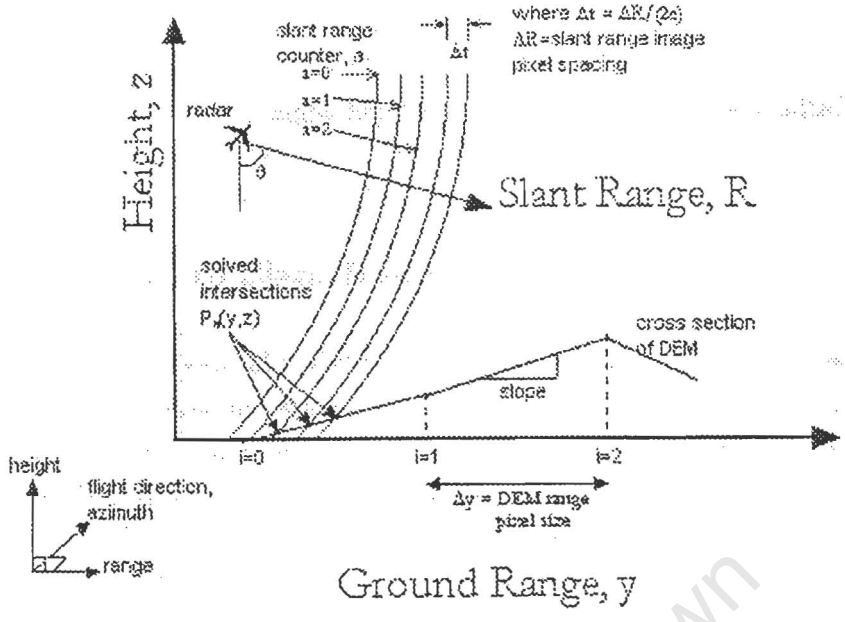

Figure 3.5: Figure showing setup for geometrical solver module.

3.3.1 Coordinate Definitions

The four coordinates used in the ground and slant range coordinate systems are further defined here, and reference Figure 3.5.

Ground Range, y

This axis is perpendicular to both height and azimuth. Under approximations described later in the section *Simplifications Made,* the radar observes the scene at the incident angle θ to the nadir in the yz plane.

Slant Range, R

This coordinate is measured radially from radar in yz plane.

Height, z

Perpendicular to both azimuth and ground range, this axis indicates vertical distance from the geoid.

Azimuth, x

Parallel to the idealised straight line flight path, this axis is also called "along track".

3.3.2 Ground to Slant Range Conversion

This conversion is essentially a change in coordinates, from the Cartesian xyz system to the xRz system. A few simplifications are made to ease the computational load but which sacrifice the modeled radar's and scene's generality. The coordinate change involves solving a system of equations, one representing the expanding sphere of the radar pulse and another representing the yz cross section of terrain, seen in Figure 3.5.

System of Equations

As will be justified in the next section, the analysis can be performed in the yz plane, that is, eliminating the x-axis. The transmitted pulses are modeled as concentric circles around the radar equally distanced by the desired slant range pixel size. The scene is modeled by linearly interpolated DEM points forming a surface of linear facets. A system of equations solving for the intersection of the circle and the DEM segment generating two solutions, only one of which is valid. The valid point is determined and the conversion to slant range coordinates is complete for the one ground range point.

Simplifications Made

The ground to slant range conversion process is a complicated arbitrary three dimensional problem. It is made easier through eliminating the azimuth coordinate by assuming that the radar's motion is a straight line parallel to the azimuth axis, restricting the radar to observation along planes of constant azimuth. Considering that the path of an airborne or satellite platform is theoretically a straight one with relatively minor deviations, the straight line trajectory assumption is valid for amplitude related images; the radar cross section image $E\{|v|^2\}$ and the magnitude of the complex interferogram $|\mathbf{z}|$. The second assumption regarding

observing at constant azimuth swaths, that is, at right angles to its trajectory, is justified considering that the squint angle, defined as the angle on the ground plane between the line of sight and the perpendicular to the azimuth axis, is generally small [15]. Hence the azimuth axis may be ignored and the problem turns into a calculation of the intersections $P_n(y, z)$ of slant range arcs and the segments of the DEM as shown in Figure 3.5. The arcs represent the transmitted radar pulses spaced in distance as the slant range pixel size.

Details on Creating the Slant Range Image

So in effect we can imagine the sensor flying relatively slowly alongside the DEM and radiating bursts at light speed off to its side and receiving the echoes a few milliseconds later. This fast imaging allows for no relative motion between the sensor and the imaging of one "row" of constant azimuth. Thus the analysis can be thought of as a series of two dimensional projections as in Figure 3.5.

Designating antenna 1 as the reference, or *master* antenna, arcs of equal distance from the master antenna are drawn at increments of ΔR , the desired slant range pixel size of the output SAR image. Where these "range circles" intersect the terrain, the locations $p_1(R_{p1}, \theta_{p1})$, $p_2(R_{p2}, \theta_{p2})$ are calculated.

$$R_{p1} = R_{near} + a\Delta R \tag{3.25}$$

where R_{near} is the slant range distance to the near swath, a is the index of the range circle, and ΔR is the slant range spacing. The slant range distance from antenna 2, R_{p2}, to the solved point p is:

$$R_{p2} = \sqrt{(z_{A2} - z_{p1})^2 + (y_{p1} - y_{HB})^2} \tag{3.26}$$

Before the calculation of θ_{p1} and θ_{p2}, the terrain slope must be known, it is a numerical derivative formed from the ratio of the change in height of the two neighbouring DEM samples, p_{DEM1}, p_{DEM2}, see Figure 3.6.

$$m = \frac{p_{DEM2,z} - p_{DEM1,z}}{p_{DEM2,y} - p_{DEM1,y}} \tag{3.27}$$

The ratio m is converted to an angle β, the terrain slope angle, and the incident angle can be calculated as the difference between the look angle to the sensor and the terrain slope.

$$\beta = \arctan(m) \tag{3.28}$$

$$\theta = \alpha + \beta \tag{3.29}$$

It can be seen from Figure 3.6 that $\theta_{p1} = \alpha_1 + \beta$ and $\theta_{p2} = \alpha_2 + \beta$.

Thus we have solved for $R_{p1}, R_{p2}, \theta_{p1}$ and θ_{p2} at point p_1 which will be used to calculate expected power value:

$$E\left\{|\mathbf{v}_{p1}|^2\right\} \propto \theta_{p1} \approx \theta_{p2} \propto E\left\{|\mathbf{v}_{p2}|^2\right\} \tag{3.30}$$

The phase at antenna 1, φ_1, antenna 2, φ_2, and the phase difference, $\varphi_1 - \varphi_2$, can be calculated as

$$\begin{aligned}
\varphi_1 &= \phi_1 + 2\pi k_1 = \frac{4\pi}{\lambda} R_1 + 2\pi k_1 && (3.31)\\
\varphi_2 &= \phi_2 + 2\pi k_2 = \frac{4\pi}{\lambda} R_2 + 2\pi k_2 && (3.32)\\
\varphi_1 - \varphi_2 &= \phi_1 + 2\pi k_1 - \phi_2 - 2\pi k_2 && (3.33)\\
&= \phi_1 - \phi_2 + 2\pi(k_1 - k_2) && (3.34)\\
W(\varphi_1 - \varphi_2) &= W\left[\phi_1 - \phi_2 + 2\pi(k_1 - k_2)\right] && (3.35)\\
&= W(\phi_1 - \phi_2) && (3.36)
\end{aligned}$$

where k_1, k_2 are integers and $W(\cdot)$ is the wrapping operator.

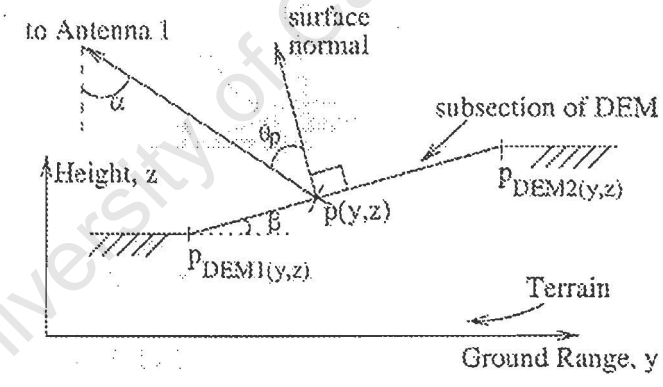

Figure 3.6: Local terrain slope of terrain cross-section.

Solving for the Remainder of the Range Line An entire range line (one row of constant azimuth value from the DEM) is analysed in which slant range vectors of distance R_1, R_2, and local terrain slopes θ_1 and θ_2 are stored for later calculations and display.

Handling Layover Areas As seen in Figure 3.7 when the pulse wavefront intersects multiple points on the terrain, these points are in layover. The returned power will be a sum of the individual powers from each of the N points in layover:

$$E\left\{|\mathbf{v}|^2\right\} = \sum_{n=1}^{N} E\left\{|\mathbf{v}_n|^2\right\} \tag{3.37}$$

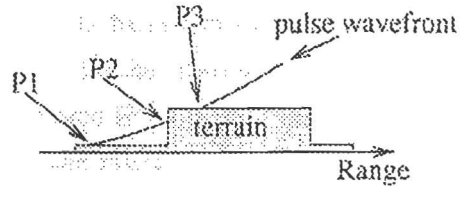

Figure 3.7: Layover condition in terrain cross section.

Handling Shadowed Areas If a slant range pixel is hidden geometrically from the radar and it is not in layover, then the expected power and the phase for that pixel is set to zero before the application of the radar noise model.

3.3.3 Radiometric and Geometric Product Calculations

Once an intersection $P_n(y, z)$ has been found, many parameters dependent on the geometry of radar and scene can then be calculated.

Radar Cross Section

As per Equation 2.5, the magnitude of the reflected power P_r is a function of the RCS σ, which is responsible for the degree of grey shading of the power image which reflects large scale geological structures. It has been shown in Equation 3.6 that σ is a function of the local incident angle θ of the pixel, and hence the position of the solved point.

$$P_r \propto \sigma(\theta) \tag{3.38}$$

Phase

The phase of the complex interferogram as shown in Equation 2.7b is dependent on the position of the solved point, as the phase is determined by calculating the slant range distances R_1, R_2 from the solved point to the two simulated radar positions. In Equation 3.39 the absolute phase is shown by φ, the wrapped phase modulo 2π by ϕ where $W(\cdot)$ represents the wrapping operator, and λ the operating wavelength of the radar.

$$\phi = W(\varphi) = \frac{4\pi}{\lambda}(R_1 - R_2) \tag{3.39}$$

Geometric coherence

From the two simulated radar positions at each solved point, the expected signal correlation due to geometry alone can be calculated as in Equation 2.12 repeated here in Equation 3.40 which is a function of the incident angles θ_1, θ_2 in the plane of the sidelooking beam from the two simulated radar positions. The radar receiver bandwidth is indicated by BW, the operating frequency by f_0, and geometrically induced spectral shift by Δf.

$$\gamma_{geom} = \frac{BW - |\Delta f|}{BW} \tag{3.40}$$

$$\Delta f = f_0 \left(1 - \frac{\sin\theta_1}{\sin\theta_2}\right) \tag{3.41}$$

Coherence Due to Finite Signal to Noise Ratio

From the radar equation as in Equation 2.5 the power received at distance R from a target of radar cross section $\sigma = A_{SR} \cdot \sigma^0$ is shown.

$$P_r = \left(\frac{P_t G^2 \lambda^2}{(4\pi)^3}\right) \frac{\sigma}{R^4} \tag{3.42}$$

$$P_r \propto \frac{\sigma}{R^4} \tag{3.43}$$

The signal to noise ratio, SNR, is proportional to $\frac{P_r}{kTB}$ where k is Boltzman's constant, T is the physical temperature of the object, and B is the bandwidth over which the power is being measured. For a SAR system, the SNR improves by a factor N, the number of independent samples in the synthetic aperture, D.

$$SNR\_sar = N * SNR$$

$$N = \frac{R\theta}{(\frac{D}{2})}$$

The product $R\theta$ is the synthetic aperture, and $\frac{D}{2}$ is the azimuth sample spacing [15]. Thus there is a link between SNR_sar and σ:

$$\begin{aligned} SNR\_sar &= \frac{R\theta}{(\frac{D}{2})} * a\frac{P_r}{kTB} \\ &\propto R * \frac{\sigma^0}{R^4} \\ &\propto \frac{\sigma^0}{R^3} \end{aligned}$$

Shadow map

By keeping track of the largest angle subtended between nadir and line of sight in the yz plane, it can be determined whether or not the solved point is in shadow from the radar's illumination. The binary map demonstrates whether the solved point is in shadow (the map contains a 1) or not (the map contains a 0). If there exists more than one solved point in a slant range cell, the pixel will be marked as in shadow only if all of the solved points are in shadow.

Layover map

If more than one solved point occurs on the same slant range arc, that slant range cell is said to be in layover. The layover map holds the integer number of solved points per arc.

A two page flowchart is shown in Figures 3.9 and 3.10 which traces out the logic behind the solver.pro subprogram.

3.4 Timing Tests

Figure 3.8 shows the average time requirements for running the full simulation process, including production of all possible output files, in terms of the number of slant range pixels in the final image. The processing time is limited by the finite amount of memory available on the server which ran the program.

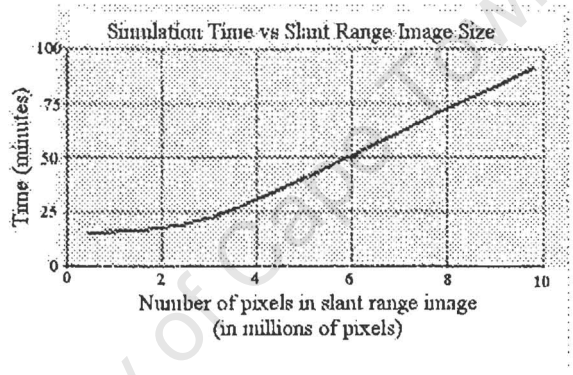

Figure 3.8: Expected time of simulation versus slant range image size.

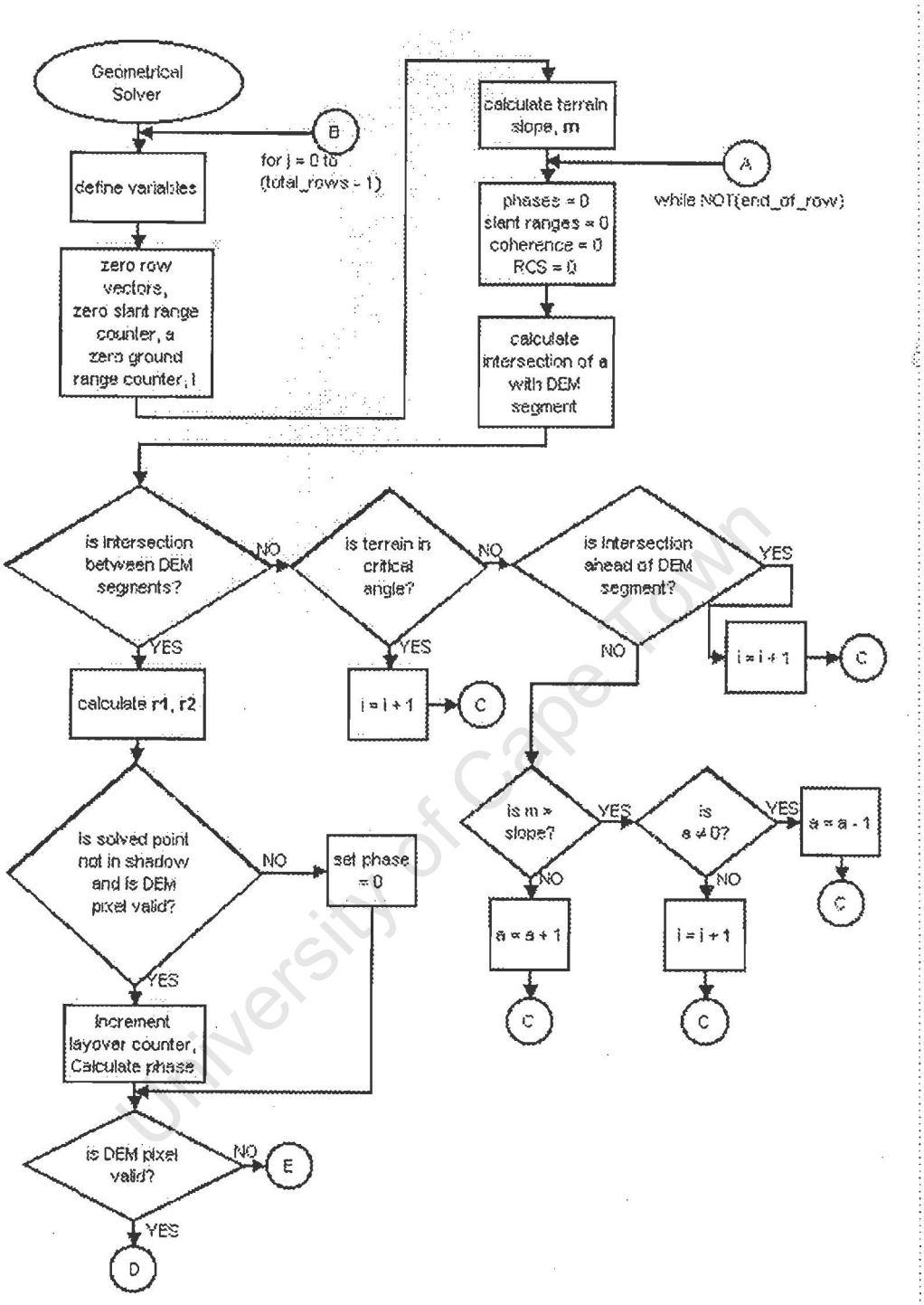

Figure 3.9: Geometrical solver module flowchart - part 1 of 2, showing conversion of ground to slant range coordinates and calculations of phase, coherence and backscattered power.

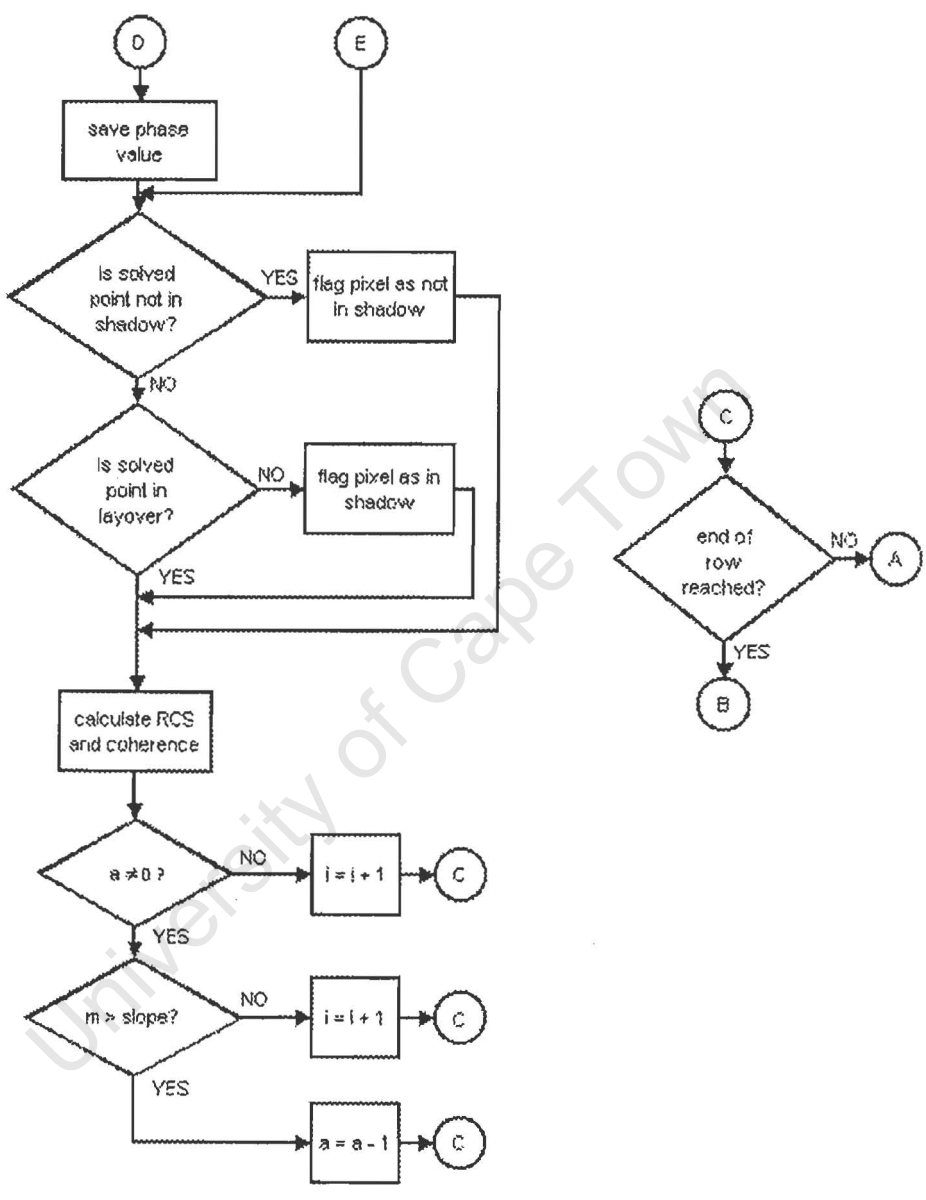

Figure 3.10: Geometrical solver flowchart, part 2 of 2.

Chapter 4

Interferometric Simulator Software Architecture and Operation

How is a practical implementation of the theoretical simulation model realised? What is needed to run the simulator? How is the simulator used? What images can it produce? The answers are the focus of this chapter, introducing the reader to a practical understanding of its workings.

4.1 Program Architecture

Starting with a so-called black box approach, the functionality of the simulator will be introduced via its primary input files and output images. Figure 4.1 lists the filenames of all the input files including the DEM, its two masks, the two descriptive ASCII text files indicating pixel sizes, endian information, backscatter models and time correlation information and the radar and antenna information file. These files are necessary and sufficient for the operation of the simulator.

The output images listed are all the possible images that may be written, each at the request of the user. In addition to the images, a log file is also produced. This is an ASCII text file containing all pertinent information, completely describing the simulation inputs, processes and outputs. Each of the input and output files named in Figure 4.1 will be reviewed in this chapter.

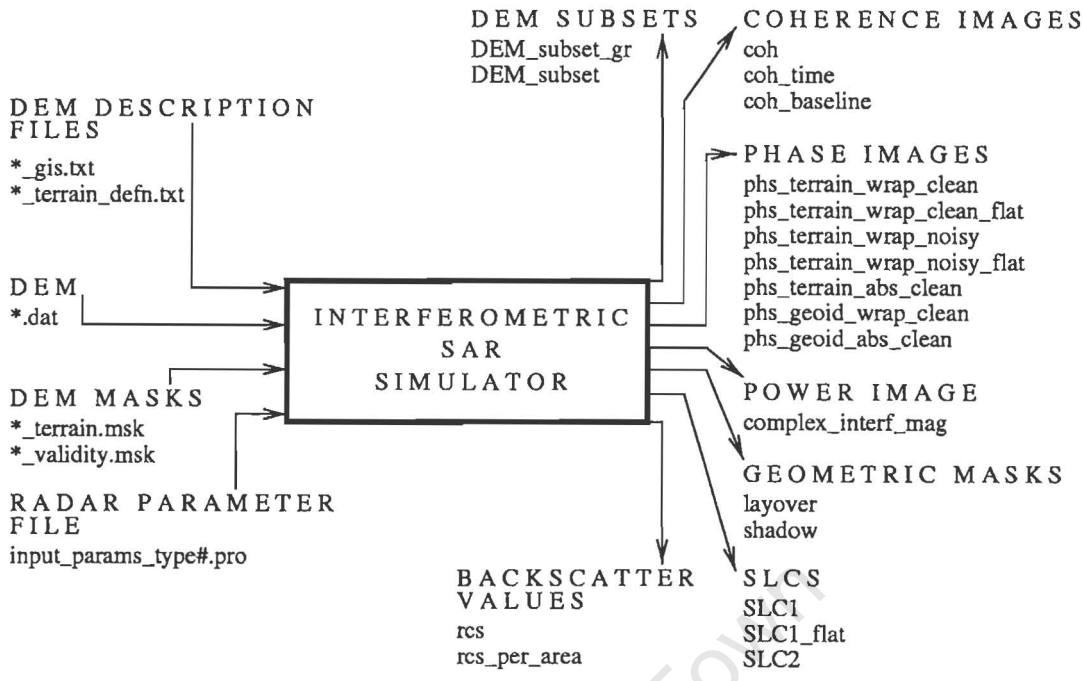

Figure 4.1: Block diagram of simulator showing all input files and output images.

4.1.1 Simulation Model

This model was introduced in the Chapter 2, in Figure 2.6 as an approach to explaining systematically how the distributed target $a(x, y, z)$ is imaged by the two slightly different angles to produce single look complex images and a complex interferogram. See Figure 4.2 for the following relation of the simulation model functions and the code routines involved.

The solver.pro routine converts the scene from ground range to slant range coordinates and applies a filter modelling the receiver. Currently the bandlimiting effect of the receiver is not implemented so the filter can be viewed as all-pass; equal to one. The ground to slant range conversion technique was described in Chapter 3.

Next, the slant range images need to be rebinned to match the pixel sizes specified by the user. This is accomplished in the processing.pro routine. Where needed, interpolation between pixels has been applied for attaining a more realistic image.

The add_speckle.pro subprogram simulates circularly Gaussian random noise using a probability density function with a mean of zero and a standard deviation

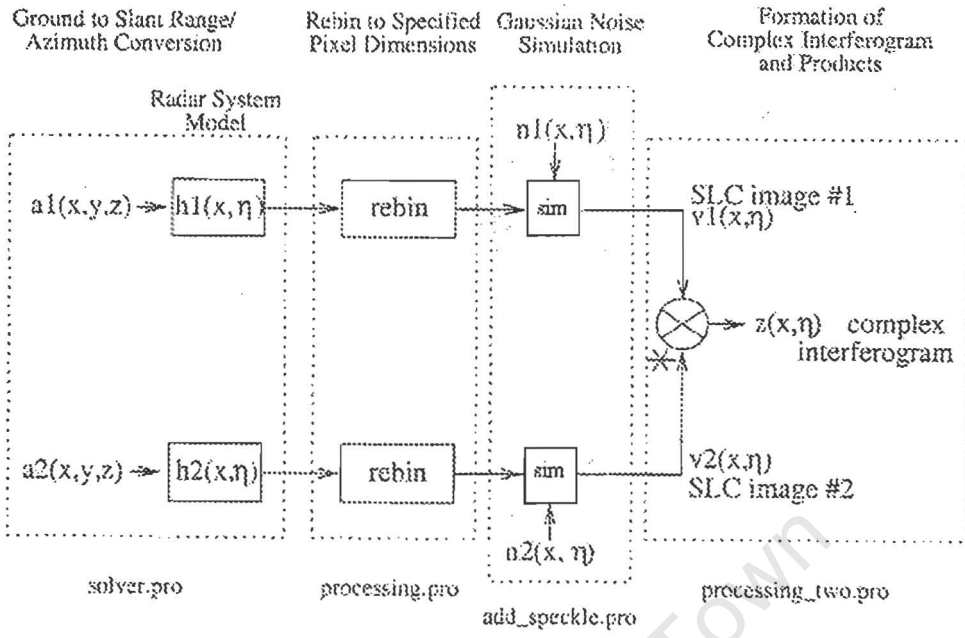

Figure 4.2: Symbolic interferometric simulation model. Primary functions of each stage is noted on top of each dotted module with the associated code filename at the bottom.

that is based on the magnitude of the complex coherence and the backscattered power. Noise is applied to form the SLC images. The noise generation process was explained in Chapter 3.

Final processing steps on the noisy data is done in processing_two.pro. The complex interferogram $\mathbf{z}(x,\eta)$ is formed by taking the complex conjugate of image 2 and multiplying it by image 1. The complex interferogram is indeed a complex image which can be separated into the magnitude of the complex interferogram:

$$|\mathbf{z}(x,\eta)| = |\mathbf{v}_1(x,\eta)\,\mathbf{v}_2^*(x,\eta)| \tag{4.1}$$

and the phase of the complex interferogram.

$$\arg\left[\mathbf{z}(x,\eta)\right] = \arg\left[\mathbf{v}_1(x,\eta)\,\mathbf{v}_2^*(x,\eta)\right] \tag{4.2}$$

4.1.2 Simulation Architecture

The simulation stages at which the output files are generated are shown in Figure 4.3. The clean SAR products i.e. the products before the noise model is applied, are formed after the rebinning stage, only one simulated antenna is needed for these images. The clean InSAR products use views from both antennas to form coherence images and interferograms. Passing the two wrapped terrain interferograms through the noise application process and taking the complex conjugate of the two SLCs results in noisy InSAR products: the three SLCs, the magnitude of the complex interferogram and the two wrapped terrain interferograms.

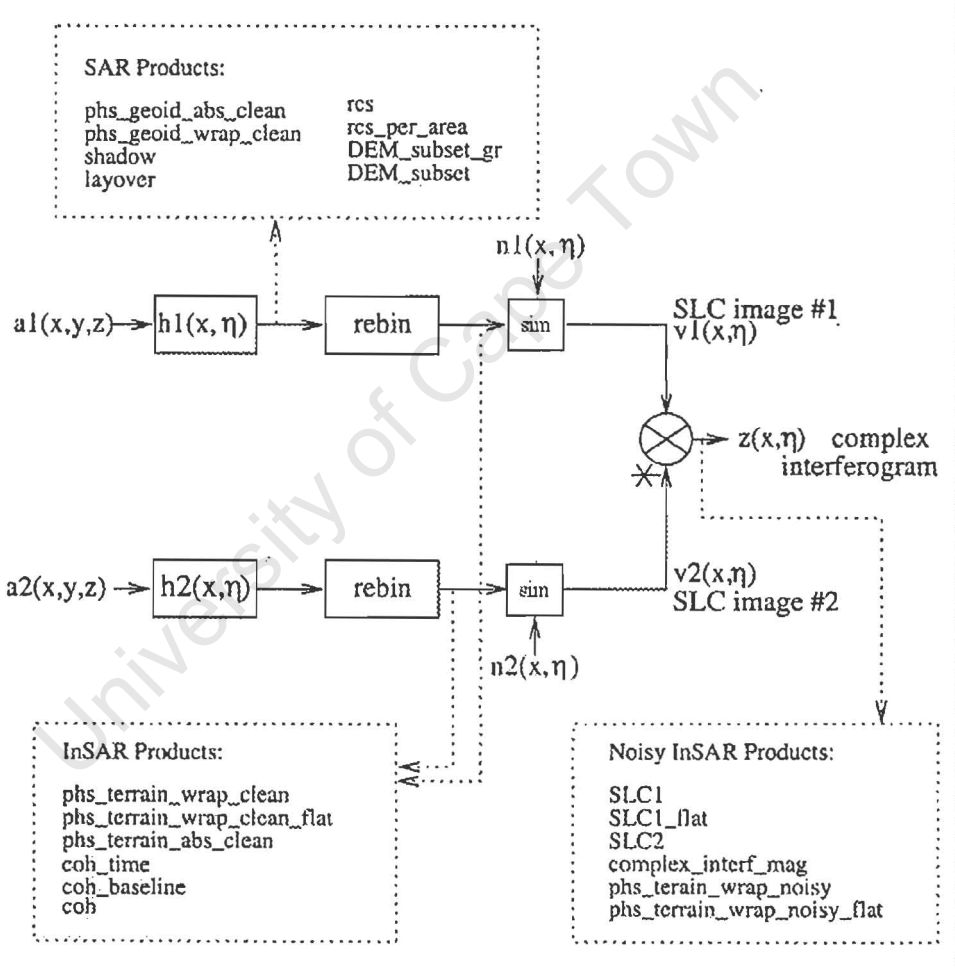

Figure 4.3: Symbolic interferometric simulation model with locations of output files noted.

Table 4.1: Simulator input files.

Description	Name of File	Data Type
Input Parameter File	input_params_type#.pro	ASCII text
DEM	*.dat	Float
DEM GIS File	*_gis.txt	ASCII text
DEM Terrain Mask	*_terrain.msk	Byte
DEM Terrain Definition File	*_terrain_defn.txt	ASCII text
DEM Validity Mask	*_validity.msk	Byte

4.2 Program Input Files

The simulator needs in addition to the source code files used for its core operation, six extra files: three text files, two image masks and one DEM.

4.2.1 Naming Conventions and Locations of Input Files

There are six input files that are needed for a complete run of the simulator. The descriptions and filenames are shown in Table 4.1. All six files must be placed in the same directory. Upon running the simulator a window will query the user for the location of the input_params_type#.pro file and hence the directory of all input files. See sub-section 4.2.2 *Input Parameter Files* to determine which of the two files is relevant to the desired simulation.

Note that the convention for filenames must be strictly followed, with * denoting the same continuous word or phrase in each of the files. For example a valid set of filenames would be:

cape.dat

cape_gis.txt[1]

cape_terrain.msk

cape_terrain_defn.txt

cape_validity.msk

[1]GIS stands for Geographic Information Systems

4.2.2 Input Parameter Files

The user options and input radar parameters are defined in one of two IDL files depending on which setup parameters the user has ready. The two files are provided for the user's benefit to reduce calculations and either one may be used. During the operation of the simulator, the user is prompted which of the two files is to be read in: input_params_type1.pro or input_params_type2.pro. Figures 4.4 and 4.5 show the defining starting parameters for each of these files.

Common to both files are the following parameters:

- final slant range image pixel spacings in both range and azimuth.
- row subset (azimuth subset) of DEM.
- row number for plotting diagnostic graphs.
- master antenna (antenna 1)'s height above spheroid.
- slave antenna (antenna 2)'s height above spheroid.
- desired rotation angle of DEM and terrain masks, in xy plane, measured in degrees clockwise.
- antenna horizontal baseline; the spacing in range between master and slave antennas, assumed constant throughout simulation.
- bandwidth of transmitted RF waveform.
- wavelength of transmitted signal.
- signal to noise ratio of the receiver.
- path and name of simulation log file.
- path and directory where all other user input files reside such as the DEM, the DEM validity mask, the terrain type mask, the terrain type definition file and the GIS file.
- desired output image files to write to disk

In addition to the above, input_params_type1.pro also includes the following, depicted in Figure 4.4:

- slant range distance to near swath, R_{near}.
- number of slant range bins or samples.

Using the input_params_type1.pro file is useful when the number of slant range samples, which corresponds to the number of bins in a standard analogue to digital (A/D) converter, is known or limited as would occur if a real SAR is simulated. The limiting parameters; sensor altitude, finite A/D storage size and the slant range distance to the near swath entirely characterises the geometrical setup of the SAR. All the remaining calculations are performed by the simulator and output to the screen. The user may accept these calculated parameters or change the input values and try again.

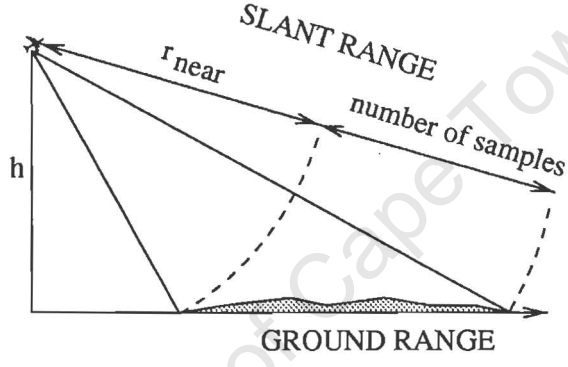

Figure 4.4: Distinguishing geometrical parameters used for first input parameter file are the slant range distance to the near swath and the number of slant range samples.

The file input_params_type2.pro has the common parameters plus the following items, shown in Figure 4.5.

- incident angle to ground range midswath, θ_{mid}.
- ground range extent of swath, y_{swath}.

Using this file is useful when a particular area of the ground is to be covered in full for the simulation and there is no restriction on the number of slant range bins as with input_params_type1.pro.

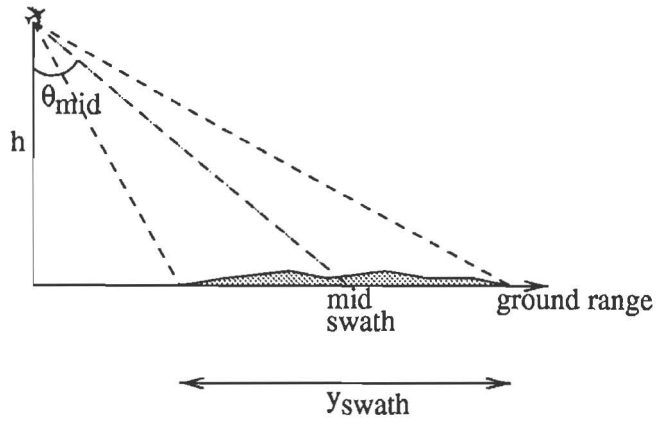

Figure 4.5: Distinguishing geometrical parameters used for second input parameter file are the incident angle at mid-swath and the ground range distance to mid-swath.

Example An example of the two input parameter files are included in Appendix B. The fields that can be altered are marked in bold typeface.

File Setup Details The input parameter files are IDL routines, therefore any extraneous lines such as comment fields have to prefixed with a semicolon.

4.2.3 Digital Elevation Model (DEM)

A DEM is a two dimensional array of terrain elevation values upon an evenly sampled grid. Either a faceted (as seen in Figure 4.6) or smooth surface can be realised by using either linear or cubic interpolation respectively between elevation samples. The DEM does not exhibit any surface detail such as foliage, buildings or people; it simply represents the so-called bald earth.

File Format The DEM must be of floating point type for use with the simulator with numerical values denoting height in metres above the chosen geoid. Either endian type is acceptable and must be noted in the DEM GIS file as seen in the following section.

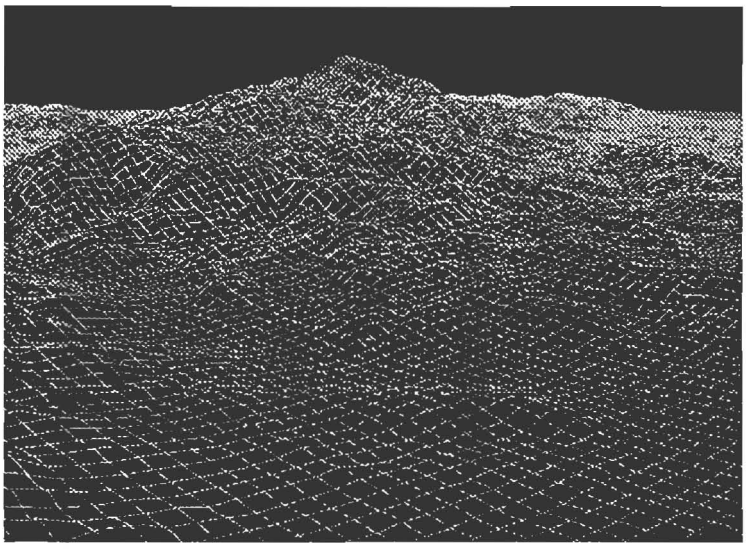

Figure 4.6: Faceted surface formed from interpolating a DEM. Provided by PCI Enterprises Inc.

4.2.4 DEM GIS File

The DEM GIS file is an ASCII text file which contains information about the number of rows and columns of the DEM, the ground range spacing in both range and azimuth between each sample, the endians of the DEM, the validity mask and the terrain mask. The variable names, data types, units and sample usage can be found in Table 4.2. In this table, a *long* refers to a 32 bit signed integer, a *float* to a 32 bit floating point number, and a *byte* to an 8 bit unsigned integer.

Example

A sample of the DEM GIS file is as follows:

DEM_rows = 500
DEM_cols = 180
DEM_pix_x = 100.
DEM_pix_y = 100.
DEM_endian = 0
validity_mask_endian = 0

Table 4.2: DEM GIS file contents.

Variable	Data Type	Units	Example
DEM_rows	long	rows	DEM_rows = 500
DEM_cols	long	columns	DEM_cols = 180
DEM_pix_x	float	metres	DEM_pix_x = 100.
DEM_pix_y	float	metres	DEM_pix_y = 100.
DEM_endian	byte	0 = little, 1 = big	DEM_endian = 0
validity_mask_endian	byte	0 = little, 1 = big	validity_mask_endian = 0
terrain_mask_endian	byte	0 = little, 1 = big	terrain_mask_endian = 0

terrain_mask_endian = 0
<blank line>
comments may go here, as long as they follow at least one blank line

File Setup Details There must be no blank lines at the beginning of the text file nor in between the seven assignment statements. The lines may not be interchanged with each other and only one assignment statement must exist per physical line. After the seventh statement there must be at least one blank line after which may exist as many lines of comments as desired as they will not be read into the simulation process.

Note on Endian The endian refers to the way the computer stores the bytes of a multiple byte integer number. Some machines store, for example, a two-byte integer with the least significant byte first followed by the most significant byte. These machines are called little endian machines. Other machines store a two-byte integer with its most significant byte first followed by it least significant byte. These machines are called big endian machines. Most SUN machines are big endian whereas most PCs are little endian machines. As seen in Table 4.2, "0" represents little endian and "1" represents big endian.

4.2.5 DEM Validity Mask

A mask is a two dimensional byte array with the same dimensions as the DEM. Each value carries specific information on the classification of that DEM pixel. The DEM validity mask marks DEM pixels which contain values pertaining to a true height measurement as opposed to a nonsense value. Consider the situation where a DEM contains height values of zero. This could represent an area of land at zero height or it could be an artifact due to a cropped or rotated DEM inside a larger array. This mask clears the confusion, containing a "1" for valid height values and "0" for invalid height values.

File Format Byte array of ones for valid height values and zeros for nonsense height values. The size of the array is identical to the DEM.

4.2.6 DEM Terrain Type Mask

The DEM terrain type mask and the DEM terrain type definition file exist to assign both a temporal correlation factor and a model for the backscattered power. As with the DEM validity mask, the terrain type mask is also a ground range array of identical dimensions as the DEM, and contains byte values according to user prescribed classes of terrain cover as seen in the next section. Integer values from 0 to 255 inclusive may be used to denote separate classes of terrain, and for each class the integer used, the time correlation factor and the backscatter parameters need to be included in the terrain type definition file.

File Format Byte array of values pertaining to those listed under "terrain type" as discussed in the next section.

4.2.7 DEM Terrain Type Definition File

For each terrain type that exists in the terrain type mask, this file includes both a time correlation factor γ_{time} and backscatter model parameters.

Time Correlation Factor

This factor γ_{time} is valid from $0 \leq \gamma_{time} \leq 1$, as noted by Equation 2.15, and denotes the degree of correlation expected between the two simulated passes of the sensor. A value near 1 denotes a high temporal correlation between passes and values near 0 denote low correlation. For example, a region exhibiting high time correlation would be rocky plains with little or no vegetation, and the sea surface would be a region with low correlation due to the fast-changing wave patterns. Care should be taken not to set γ_{time} to exactly zero.

Backscatter Model

The radar cross section σ is a measure of the scattered power from a discrete reflecting object, having units of m^2. It is a product of the unit-less parameter σ^0, so-called *sigma nought*; the mean reflectivity per unit surface area of the material, and A_{GR}, the ground range pixel area.

$$E\left\{|V|^2\right\} = P_r \propto \sigma = \sigma^0 A_{GR} \tag{4.3}$$

The normalised value σ^0, is an inherent characteristic of the material and has be modeled empirically as a function of the local incidence angle, θ, the frequency and polarisation [27] as a result of many scatterometer experiments. More details on the justification for using this backscatter model can be found in Chapter 3, section 3.2.1. To sum up, the backscatter from rocky or vegetated terrain can be modelled as:

$$\sigma^0_{mean}(\theta) = P_1 + P_2 \exp(-P_3\theta) + P_4 \cos(P_5\theta + P_6) \tag{4.4}$$

where θ is in radians and σ^0_{mean} is in dB. Values for the coefficients P_1 to P_6 depend on the terrain type, frequency of operation, polarisation, soil moisture content. Typical values for the operation of a C-band, VV polarisation SAR imaging rocky and vegetated terrain of average moisture content are:

$$\begin{bmatrix} P_1 \\ P_2 \\ P_3 \\ P_4 \\ P_5 \\ P_6 \end{bmatrix} = \begin{bmatrix} -88.593 \\ 99.000 \\ 0.326 \\ 9.574 \\ 1.969 \\ -3.142 \end{bmatrix} \tag{4.5}$$

File Setup Details

This is a text file that can include from one to thirty terrain type definitions. Each definition occupies one line of text. No blank lines should occur in the document, and within each line, each parameter must be separated by one or more spaces. The <description of terrain type X> is unused by the simulator and is included only as a reference for the user. It can be a word or combination of words, as long as there are no spaces within the text. The format of the document should be:

<description of terrain type A> <integer denoting type A> <γ_{time} value A> <P_{1A}> <P_{2A}> <P_{3A}> <P_{4A}> <P_{5A}> <P_{6A}>

<description of terrain type B> <integer denoting type B> <γ_{time} value B> <P_{1B}> <P_{2B}> <P_{3B}> <P_{4B}> <P_{5B}> <P_{6B}>

...

After the last terrain type, at least one blank line must be included before any comments are included. These comments may be plain text and need not be prefaced with any special character. Also, there may be as many comment lines as desired.

Example

A terrain type file that incorporates two classes of terrain; Land and Water, with integer numbers 1 and 0 respectively, γ_{time} equalling 0.9 and 0.1 respectively, and a backscatter model coefficients as described in Equation 4.5 is as follows:

Land 1 0.9 -88.593 99.000 0.326 9.574 1.969 -3.142

Water 0 0.1 -88.593 99.000 0.326 9.574 1.969 -3.142

This assumes that within the terrain type mask the integer 1 is contained in each pixel which pertains to "land" and the integer 0 for "water".

4.3 Program Output Files

All image files produced by the simulator have associated text headers designed for viewing with the VIEWIMG.PRO software, an in-house program for easy image display. For example if the image is named *, then the header will be named *.txt. The headers are included in the same directory as the images. This is the directory specified by the user in the input_params_type_#.pro file in the line:

```
startup_params.output_dir = '/usr/idl/InSIM/output/'
```

4.3.1 Note on SAR Projections

Ground Range The standard latitude/longitude projection that the DEM and inputs masks exist in.

Slant Range Most of the output images are produced in slant range-azimuth projection as seen by the radar. There has been no elevation corrections made to the data. Terrain correction has not been applied, so the foreshortening and layover effects still exist.

4.3.2 Naming Conventions and Locations of Output Files

As mentioned all output files in Table 4.3 are located in the directory specified by the above assignment statement beginning with startup_params.output_dir.... All the following are explained further in subsequent sections. All image files are in slant range projection except DEM_subset_gr.

4.3.3 Log File

Filename: log.txt

An ASCII text log file is generated which contains all pertinent information to the simulation, including all user setup variables, time of start and end of simulation, DEM information, DEM mask information, antenna positions, calculated ground

Table 4.3: Simulator output files.

Description	Name of File
log file	log.txt
DEM subset of area used	DEM_subset
DEM subset, ground range	DEM_subset_gr
RCS values	rcs
RCS values without area effect	rcs_per_area
shadow map	shadow
layover map	layover
complex coherence, magnitude	coh
coherence factor due to temporal stability	coh_time
coherence factor due to baseline	coh_baseline
coherence factor due to SNR	coh_snr
geoid absolute phase	phs_geoid_abs_clean
geoid wrapped phase	phs_geoid_wrap_clean
complex coherence, phase with earth component	phs_terrain_wrap_clean
complex coherence, without earth component	phs_terrain_wrap_clean_flat
terrain wrapped phase, noisy	phs_terrain_wrap_noisy
terrain_wrapped phase, without earth component, noisy	phs_terrain_wrap_noisy_flat
terrain absolute phase	phs_terrain_abs_clean
SLC (single look complex) image from antenna 1, noisy	slc1
SLC image from antenna 1, flattened, noisy	slc1_flat
SLC image from antenna 2, noisy	slc2
complex interferogram, magnitude, noisy	complex_interf_mag

and slant range distances to imaged swath, incident angles and output files with statistics. A sample of this file can be found in Appendix C.

4.3.4 DEM Subset, Ground Range

Filename: DEM_subset_gr

Header: DEM_subset_gr.txt

Projection: ground range

Depending on the rows selected and the effective simulated ground range swath, the entire DEM need not be simulated. This image shows the subsection of the DEM that was used for simulation.

4.3.5 DEM Subset, Slant Range

Filename: DEM_subset

Header: DEM_subset.txt

Projection: slant range

This image is the ground range DEM subset converted to slant range projection. As image distortions such as layover and shadowing may occur which could be confusing when analysing the phase or coherence images, this slant range DEM was included for easier interpretation. Some discrepancies between ground and slant range images may also occur due to improper input parameter selection. For example, for a set near slant range distance, R_{near}, some close range structures could be missed and will not appear on the slant range image.

4.3.6 Radar Cross Section

Filename: rcs

Header: rcs.txt

Projection: slant range

Using the user-defined backscatter model, the radar cross section is computed as a function of the computed sigma nought value and the ground range area of each pixel.

$$\sigma = \sigma^0 A_{GR} \tag{4.6}$$

This adds the so called slope effect whereby patches of terrain that are angled near perpendicular to the radar line of sight return more power to the radar and thus appear brighter than other cells oriented at a different angle.

4.3.7 Normalised Radar Cross Section

Filename: rcs_per_area

Header: rcs_per_area.txt

Projection: slant range

This is the normalised terrain reflectivity σ^0 from Equation 4.6 as determined by the simulator based on the model supplied by the terrain type definition file and the calculated local values of the incident angle at each slant range pixel. This slant range mask contains floating point values corresponding to the reflectivity divided by the area of the two dimensional slant range pixel.

4.3.8 Shadow Map

Filename: shadow

Header: shadow.txt

Projection: slant range

Any pixel that is hidden from the radar's line of sight by the topography of the terrain is said to be in shadow. This map is a binary map, with 0 denoting "not in shadow" and 1 denoting "in shadow". Pixels that are in shadow will be blackened out on the following images: complex coherence magnitude, both coherence factor images, terrain absolute phase, all SLC images, complex interferogram magnitude, both noisy terrain phases, both RCS images, and DEM slant range subset.

4.3.9 Layover Map

Filename: layover

Header: layover.txt

Projection: slant range

Layover occurs when one or more locations on the ground have the same slant range to the radar. These pixels are marked in this map, with the value of the pixel denoting the number of pixels that map to the same slant range cell. The image is of integer type, with contents of 0 for no layover and 1,2,3,... for the number of overlaid pixels.

4.3.10 Complex Coherence, Magnitude

Filename: coh

Header: coh.txt

Projection: slant range

The complex coherence magnitude is denoted $|\gamma|$, and is the correlation coefficient between any two imaged points and is a product of the individual coherence factors as shown in Equation 2.10, reproduced below.

$$\gamma = \gamma_{geom}\,\gamma_{time}\,\gamma_{SNR}\,\exp(j\Delta\phi) \tag{4.7a}$$

$$|\gamma| = \gamma_{geom}\,\gamma_{time}\,\gamma_{SNR} \tag{4.7b}$$

γ_{geom} is the geometric coherence, sometimes called the baseline coherence. Both γ_{geom} and γ_{time} are output images described below, while γ_{SNR} is a constant value as computed in Equation 2.14b. As with all other coherence masks/images, this matrix is of floating point type and ranges from 0 to 1.

The greyscale image is scaled so that black represents a coherence value of 0 and white represents 1. An optional scale bar may be added to the bottom left hand corner of the image for easy determination of absolute coherence values.

4.3.11 Coherence Time Factor, Slant Range

Filename: coh_time

Header: coh_time.txt

Projection: slant range

As seen in Equation 4.7b $|\gamma|$ is a function of γ_{time}. This image is the γ_{time} factor which denotes the degree of temporal correlation between the two antenna looks. The values for γ_{time} are derived from the DEM Terrain Definition File.

As with the principle coherence image, the time factor image also ranges from 0 to 1 represented by black to white. Again, the scale bar is optional.

4.3.12 Coherence Geometric Factor, Slant Range

Filename: coh_baseline

Header: coh_baseline.txt

Projection: slant range

This coherence factor γ_{geom} is calculated by the simulator, and is dependent on the range bandwidth and the slope-induced range spectral shift [30].

This mask contains floating point values between 0 and 1 represented by black to white greytones with an optional scale bar.

4.3.13 Coherence SNR Factor, Slant Range

Filename: coh_SNR

Header: coh_SNR.txt

Projection: slant range

This coherence factor γ_{SNR} is calculated by the simulator, as a function that is proportional to the radar cross section and inversely proportional to R^3 where R is the slant range distance from the radar to the observed terrain point.

The SNR has been scaled to values between 0 and 1 represented by black to white greytones with an optional scale bar.

4.3.14 Geoid Absolute Phase

Filename: phs_geoid_abs_clean

Header: phs_geoid_abs_clean.txt

Projection: slant range

The phase component due to the presence of the geoid is represented here. This is a slowly varying greyscale image from near range to far range, with similar values along lines of constant range. There are no ambiguities in the data, as it is not wrapped. The image is of floating point type.

4.3.15 Geoid Wrapped Phase

Filename: phs_geoid_wrap_clean

Header: phs_geoid_wrap_clean.txt

Projection: slant range

A wrapped version of the geoid absolute phase. The image is of floating point data and the phase is wrapped in the region $-\pi$ to $+\pi$.

4.3.16 Terrain Absolute Phase

Filename: phs_terrain_abs_clean

Header: phs_terrain_abs_clean.txt

Projection: slant range

The phase component due to the changing terrain, but not in its wrapped form. Ambiguities may exist due to the presence of layover areas. The image is of floating point type.

4.3.17 Terrain Phase, Wrapped, Clean

Filename: phs_terrain_wrap_clean

Header: phs_terrain_wrap_clean.txt

Projection: slant range

The phase component $\Delta\phi$ of Equation 4.7a is the clean phase component due to the difference in signal path lengths at the two antenna positions. The geoid phase component has not been removed. This image is of floating point type and the phase values exist modulus 2π, in the region from $-\pi$ to $+\pi$.

4.3.18 Terrain Phase, Wrapped, Clean, Flattened

Filename: phs_terrain_wrap_clean_flat

Header: phs_terrain_wrap_clean_flat.txt

Projection: slant range

The phase component due to the earth, the geoid phase, has now been removed. The image produced resembles a contour map with the fringes denoting areas of constant distance away from the radar. This image is of floating point type and contains phase values modulus 2π, in the region from $-\pi$ to $+\pi$.

4.3.19 Terrain Phase, Wrapped, with Noise

Filename: phs_terrain_wrap_noisy

Header: phs_terrain_wrap_noisy.txt

Projection: slant range

The phase interaction of the reflected signals due to terrain results in this terrain interferogram. The component due to the earth spheroid has not been removed, hence for regions at zero height above the spheroid there will exist a vertical fringe pattern.

4.3.20 Terrain Phase, Wrapped, with Noise, Flattened

Filename: phs_terrain_wrap_noisy_flat

Header: phs_terrain_wrap_noisy_flat.txt

Projection: slant range

This is the terrain phase image with the earth's phase component, the geoid absolute phase, removed. The resultant resembles a contour map, indeed the fringes can be used to discern the height variations.

4.3.21 SLC Image from Antenna 1

Filename: slc1

Header: slc1.txt

Projection: slant range

This is the master complex image seen from antenna 1. Its formation can be derived from Figure 4.2. This image is used to generate noisy phase images, phs_terrain_wrap_noisy and phs_terrain_wrap_noisy_flat.

4.3.22 SLC Image from Antenna 1, Flattened

Filename: slc1_flat

Header: slc1_flat.txt

Projection: slant range

The phase of this SLC has the earth component removed and is used to make the noisy flat phase image phs_terrain_wrap_noisy_flat.

4.3.23 SLC Image from Antenna 2

Filename: slc2

Header: slc2.txt

Projection: slant range

The slave complex image as seen from antenna 2. The formation is the same as SLC1.

4.3.24 Magnitude of Complex Interferogram

Filename: complex_interf_mag

Header: complex_interf_mag.txt

Projection: slant range

This is the magnitude of the complex interferogram and mostly closely resembles an optical image.

4.4 Program Operation

Once the input files have been collect and the desired output images chosen, the simulator can be run using the following instructions.

4.4.1 Input File Preparation

Gather these six input files into one directory:

DEM: Denote the dimensions m x n, containing floating point height values.

Validity Mask: Dimensions also m x n, containing byte values 0 or 1 only.

Terrain Type Definition File: ASCII text containing the terrain type byte values, backscatter parameters and temporal coherence values: $0 < \gamma_{time} \leq 1$. Note the coherence can not be set to exactly zero.

DEM GIS File: ASCII text containing DEM parameters and endian information.

Input Parameter File: one of the two types, with all relevant radar and antenna information. Ensure the existence of the output directory and the correctness of the code directory specified prior to simulation. Note that the directory pathnames are case-sensitive.

4.4.2 Running InSIM

Change directories to the program code directory. Run the IDL application with the following command:

IDL

When the IDL> prompt appears, start the simulator by typing:

.r insim

The simulator will first prompt for the location of the INPUT_PARAMS_TYPE#.PRO file. Based on the information within the file chosen, the simulator will calculate the remaining geometrical parameters regarding swath widths, slant range distances from sensor, incident angles and more. The calculated numbers will be displayed and a command line query presented. If necessary, change any parameters in the input parameter file, save the file and type "0" at the command line. This will force the simulator to re-compile the input parameter file and recalculate. Once the calculated parameters are satisfactory to the user, type "1" to accept.

Next a query box will ask for the location of the DEM, looking in the same directory as the input parameter file and displaying any files with the suffix .DAT.

There are no further queries for the user. When the simulator finishes, a banner showing the elapsed time will appear. All desired output images, their headers and the log file will be written to the output directory. View these images using the VIEWIMG.PRO routine or by manually translating the text headers into another image reading program.

Chapter 5

Results of Simulation and Comparison to Actual SAR Images

Evaluation of the resulting simulated images was accomplished by qualitative comparison to actual images. Three simulations: the Cape Peninsula, the Cedarberg Mountains and the Katse region, were performed, and the power, phase and coherence images are compared to actual SAR images.

To make this image analysis readable, all images have been reduced in size for presentation and analysis. However, all statistical tests were performed on the original simulated images.

5.1 Cape Peninsula Simulation

The Cape DEM was used in two simulations, this first simulation concentrates only on the peninsula region.

5.1.1 Notes on Simulation Parameter Selection

A medium resolution DEM was obtained for the Cape region, and a simulation was run with parameters as listed under *Peninsula* in Table 5.1. This is

Table 5.1: Parameters for Cape Peninsula simulation.

Simulation Parameter	Peninsula	Cedarberg	Katse
DEM dimensions (row x col)	550 x 220	800 x 500	510 x 544
DEM pixel size (range x azim.)	100 m x 100 m	100 m x 100 m	25 m x 25 m
DEM rotation angle (CW)	168°	168°	5°
DEM rotation point	centre of DEM	centre of DEM	centre of DEM
DEM validity mask used?	yes	yes	yes
DEM terrain mask categories	0: water, 1: land	1: land	0: water, 1: land
DEM temporal coherence values	water: 0.1, land: 0.9	land: 0.9	water: 0.1, land: 0.9
Backscatter Model	Ulaby	Ulaby	Ulaby
Antenna heights (#1, #2)	796 km, 796 km	796 km, 796 km	796 km, 796 km
Horizontal baseline	100 m	100 m	100 m
Vertical baseline	0 m	0 m	0 m
Incident angle at mid-swath	23°	23°	23°
Receiver bandwidth	15 MHz	15 MHz	15 MHz
Observing wavelength	0.0566 m	0.0566 m	0.0566 m
Simulated range spacing	7.905 m	7.905 m	7.905 m
Simulated azimuth spacing	20.240 m	20.240 m	20.240 m
Signal to noise ratio	1000	1000	1000

only a partial list containing the more important parameters; a complete set of simulation parameters can be seen in Appendix B.

With the current imaging geometrical setup, the simulator will fashion a radar viewing the DEM from left (near range) to right (far range) along the range axis. If an alternate imaging direction is desired, the DEM must be rotated. In this example, to simulate a radar looking from right to left at -12 degrees to the horizontal, rotate the DEM +168 degrees or 168 degrees clockwise (CW).

A terrain mask with two designations, land and water, was used to more accurately simulate the incoherent random appearance of the water regions. The amount of incoherence is specified in the temporal correlation mask, where, for each designation in the terrain mask, a value for coherence is assigned.

Ulaby and Dobson's backscatter model as described in Chapter 4 was used for each of the simulations.

The positions of the antennas mimic the ERS-1/2 parameters; antenna heights of 796 km, incident angle of 23°, receiver bandwidth of 15 MHz, and operating wavelength of 0.0566 m. To obtain square slant range pixels, a pixel size of 7.905 m by 20.240 m in range and azimuth respectively were chosen.

5.1.2 Description of Images in Thumbnail Collections

The resulting images from the simulation process are shown as collections, as seen in Figure 5.1. Each collection is arranged in a three-row, four column matrix, with sub-images lettered A to L. The following lists the filename and description of each sub-image:

A. DEM_subset_gr: DEM in ground range coordinates representing increasing height with lighter greyscale pixel values.

B. DEM_subset: DEM in slant range coordinates, again with increasing height denoted with lighter greyscale pixel values.

C. rcs: radar cross section with area effect.

D. complex_interf_mag: magnitde of the complex interferogram.

E. coh_baseline: coherence due to geometrical baseline, scaled from 0 (black) to 1 (white).

F. coh_time: coherence due to temporal decorrelation, scaled from 0 (black) to 1 (white).

G. coh: total coherence, scaled from 0 (black) to 1 (white).

H. layover: layover map, defined as black: 0 solved points, grey: 1 solved point, white: 2 or more solved points.

I. phs_terrain_wrap_clean: clean phase with earth component.

J. phs_terrain_wrap_clean_flat: clean phase without earth component.

K. phs_terrain_wrap_noisy: noisy phase with earth component.

L. phs_terrain_wrap_noisy_flat: noisy phase without earth component.

The north half of the Cape Peninsula is simulated, and the resulting images can be seen in Figure 5.1. Larger versions of these images can be seen in the Gallery in Appendix A.

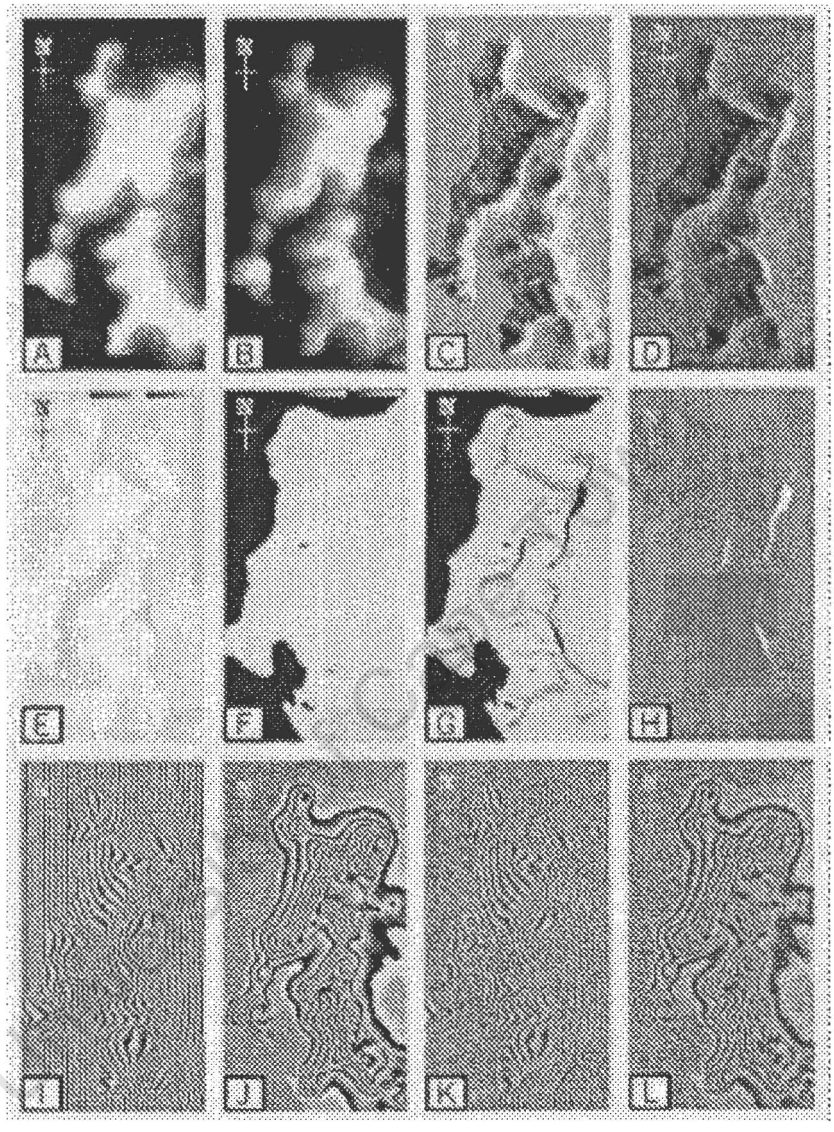

Figure 5.1: Simulated images of northern Cape peninsula. Each image is 308 x 582 pixels representing 12.4 x 23.5 km ground range.

The south half of the Cape Peninsula can be seen in Figure 5.2.

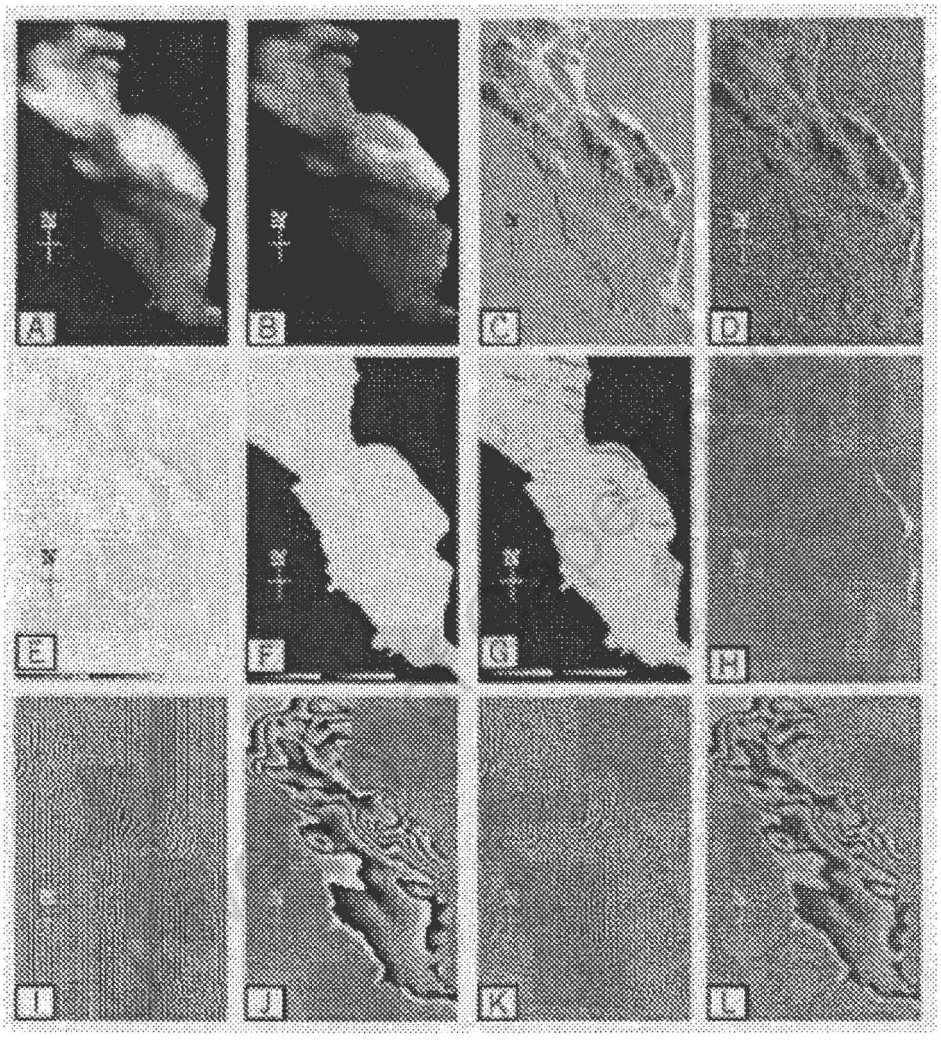

Figure 5.2: Simulated images of southern Cape peninsula. Each image is 358 x 540 pixels representing 14.6 x 22.1 km ground range.

5.2 Cedarberg Mountains Simulation

A DEM of the Cedarberg Mountains, north-east of Cape Town, offers 100 m resolution and an opportunity to test the simulator on alpine terrain. The simulation parameters are listed in column *Cedarberg* of Table 5.1.

The resulting images from the simulation are shown in Figure 5.3, in the thumbnail format as described previously.

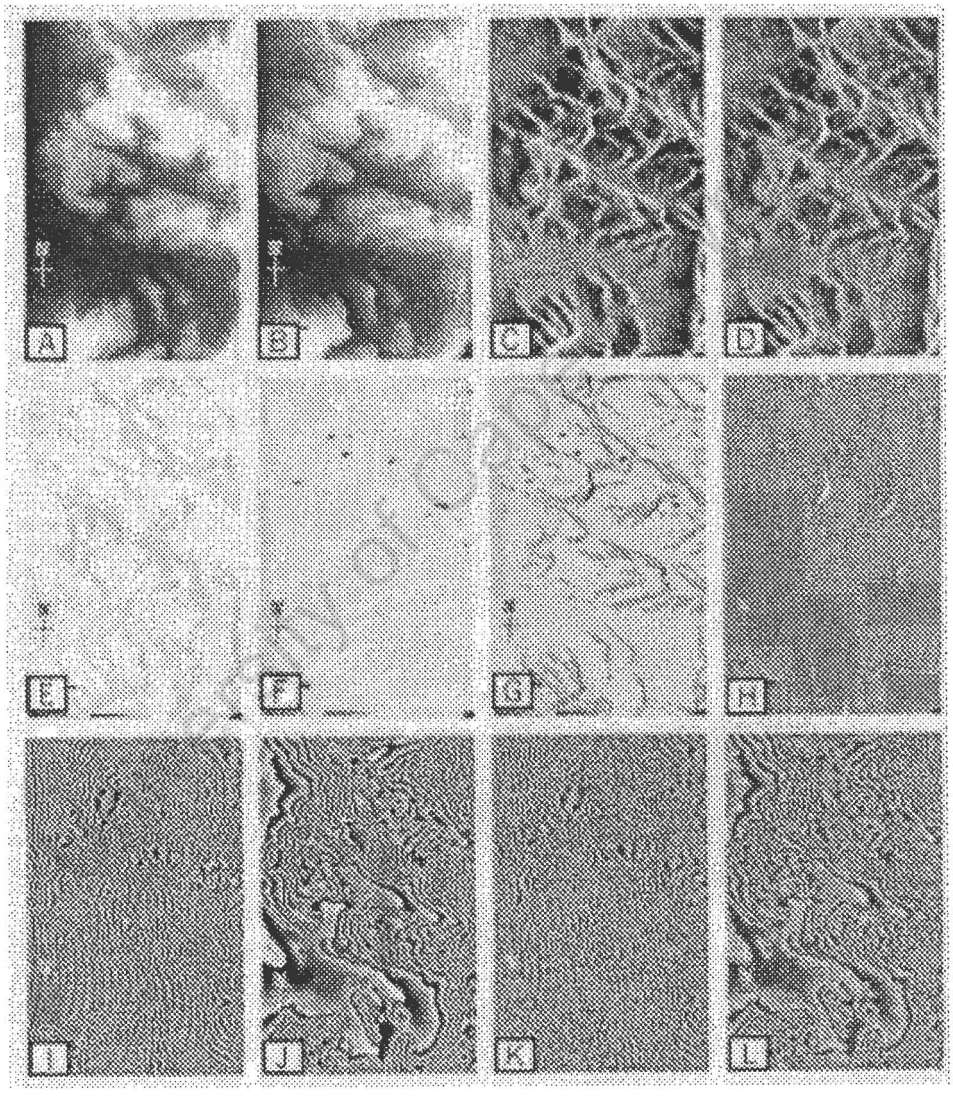

Figure 5.3: Simulated images of Cedarberg Mountains near Cape Town, South Africa. Each image is 360 x 562 pixels representing 17.4 x 27.3 km ground range.

5.3 Katse Simulation

The sparsely-populated Katse region incorporates two major rivers and some mountains. The DEM is of a finer resolution than the previous DEMs, although a smaller region is covered, so no significant improvement in visual resolution is obtained.

The last column of Table 5.1 holds the simulation parameters for the Katse images, which can be seen in Figure 5.4.

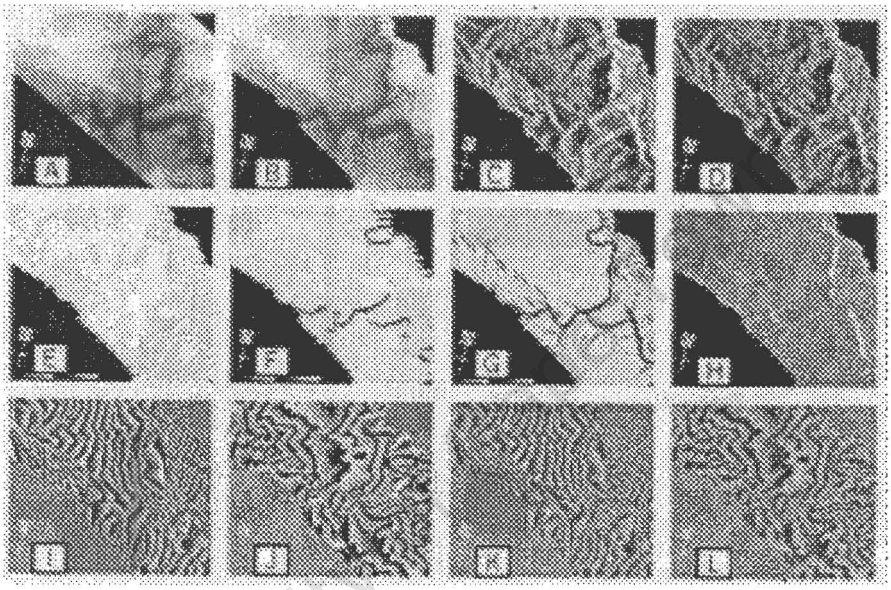

Figure 5.4: Simulated images of Katse dam region in Lesotho. Each image is 394 x 337 pixels representing 13.5 x 9.9 km ground range.

5.4 Comparison of Simulated Images to Actual ERS Images

To evaluate the functionality and operation of the simulation model, comparison to actual images is necessary. The northern Cape Peninsula images were chosen to demonstrate the strengths and weaknesses of the simulator.

The available ERS images include power, coherence, and interferometric phase images with the earth component included. The images were obtained from flight

numbers 05715 and 25388. The following simulated and actual ERS images are all imaged from 12 degrees north of east, the range axis, and image the terrain from east to west. The azimuth axis indicates the direction of motion and is perpendicular to the range axis which indicates the direction the radar is imaging.

5.4.1 Power Image Comparison

Comparison of the simulated power to the actual power images is shown in Figure 5.5. The simulated power image on the top left and the actual ERS power image is on the top right.

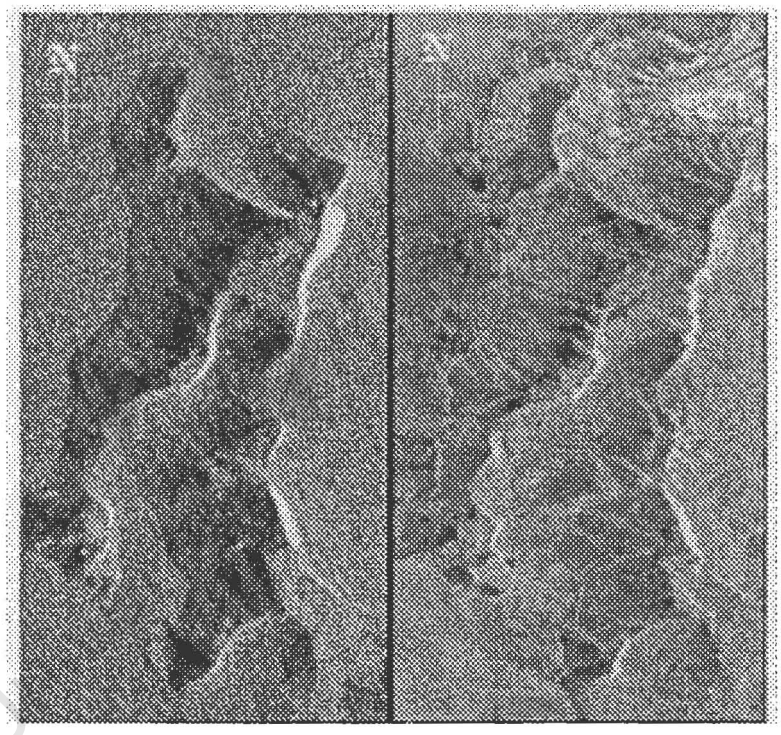

Figure 5.5: Comparison of simulated (left) magnitude squared image from the SLC: $|v_1|^2$ and actual ERS (right) power image $|v_1|^2$.

General Greytones

The mountain slopes and tops can be readily identified, the regions of layover appear equally bright on both images. The greytones of the mountain slopes are correct in proportion to the average intensity.

Urban Detail

The finer resolution of the ERS power image shows more detail on the mountain slopes, large-scale water patterns, and features of the urban and harbourfront areas of Cape Town to the north. The simulator has no information that an urban area is present, thus it produces backscatter information similar to that of a flat plain at the height designated. Urban areas appear very bright on radar images due to the strong reflections from the dihedral and trihedral corners made by buildings and pavement. Settled areas can be deduced from the different brightness values of the simulated and actual images, populated areas are found on the eastern side of the easternmost mountain ridge to two-thirds down the image.

Ocean Detail

Again, the simulator knows no information about the wave patterns. From the terrain mask, it can determine that the region is composed of water and has a certain correlation value.

5.4.2 Coherence Image Comparison

Figure 5.6 compares the simulated and actual total coherence images. This simulated coherence takes all of geometrical, temporal and noise due to finite SNR into account.

The calculated coherence is accurate in determining the very low coherence of the ocean and a moderate value for the land areas. It does well in showing that in areas of low power returned, for example the shadowed areas of the mountains, there is a significant drop in coherence also. This shows that the model for receiver noise is an appropriate one. The urban areas appear comparatively bright in the ERS image, due to the invariability of the major structures between the imaging times. The very dark areas on the mountain ridges of the simulated image correspond to the very bright areas on the simulated power image. This is evidence of layover, when two or more pixels correspond to the same slant range position. The very low coherence value results from the addition of the complex coherence values of each slant range pixel, which have uniformly distributed

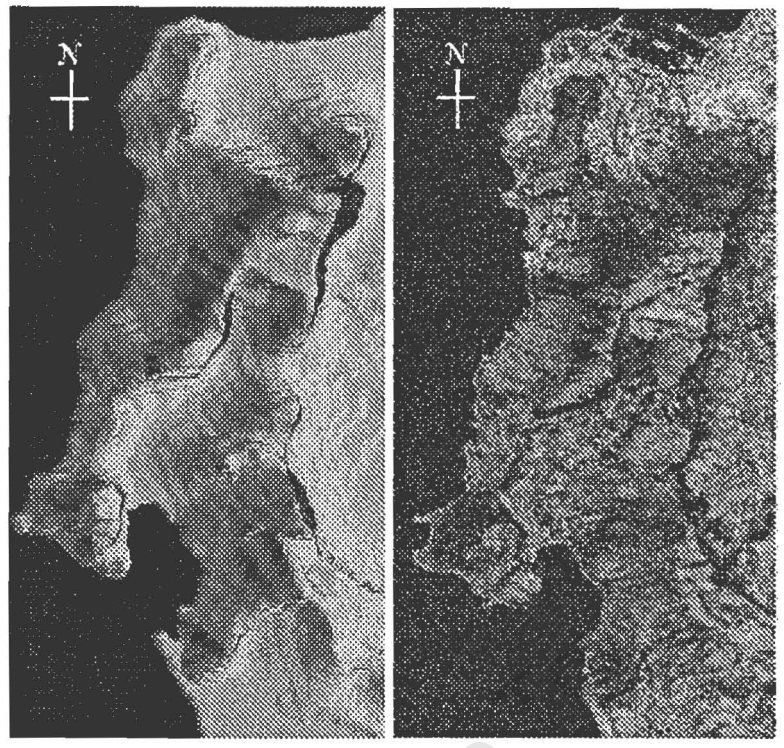

Figure 5.6: Comparison of simulated (left) and actual ERS (right) coherence images.

phases. Expected low-coherence regions due to layover can also be seen in the ERS image.

5.4.3 Interferogram Image Comparison

Figure 5.7 shows the unflattened wrapped interferograms of the imaged terrain. The simulated image uses a greyscale pattern and the actual ERS image uses a coloured pattern. There is complete decorrelation in the ocean areas of both images, as predicted by the coherence values. The regular vertical fringe component due to the flat earth component has not yet been removed. The horizontal baseline chosen during simulation directly affects the spacing of the fringes.

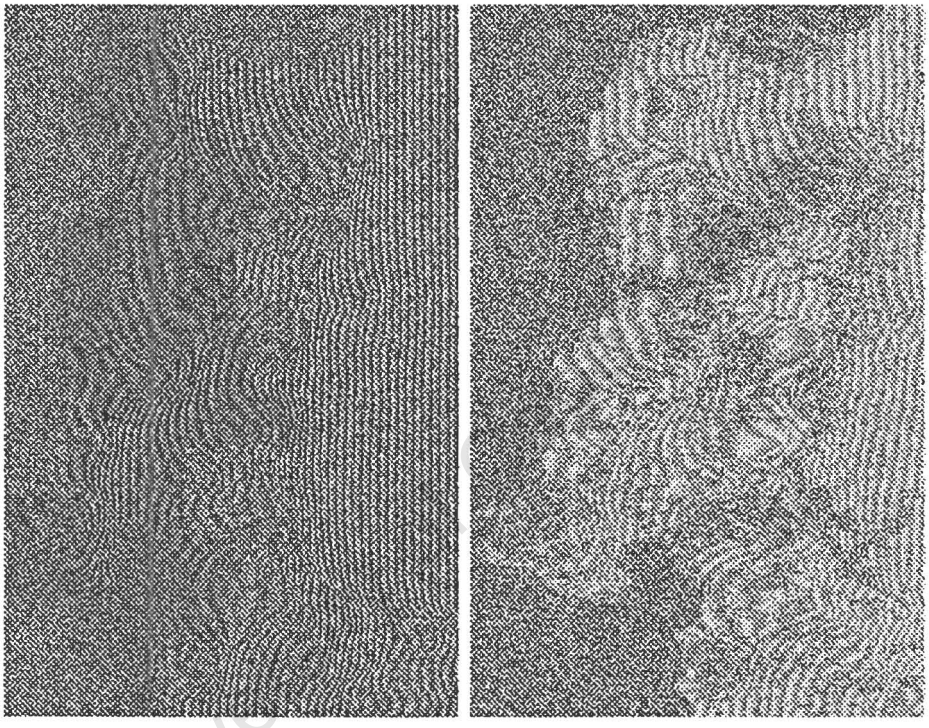

Figure 5.7: Comparison of simulated (left) and actual ERS (right) interferometric phase images.

Chapter 6

Conclusions and Future Work

A synthetic aperture radar software program was created for the purpose of mission planning, image interpretation and interferometric demonstration and algorithm development.

A product simulator model was chosen to fulfill the purposes listed above with minimum amount of complexity in development. The DEM, the flight path, correlation and radar parameter information were inputs.

The SAR and InSAR imaging models were based on a model for the scene and the slant range conversion process. The scene can be described as a distributed target; a collection of point scatterers. The responses from the targets superpose linearly to form complex circularly Gaussian random variable images. The conversion from ground range to slant range is a purely geometric one, involving the solution of the transmitted wave and the terrain facets. Quirks arising from the imaging geometry include layover and shadowing which further characterise the SAR image.

SAR image characteristics including their statistics and dominant factors have been comprehensively studied. This aids in qualifying the success of the simulation when compared to actual images. The backscatter values greatly influence the tonality of the simulated power images, thus the correct computation of its components, the backscatter coefficient and the slant range area, are critical to the success of the simulated image. The process of calculating the backscatter values were reviewed, along with a generic empirical backscatter model for use with ERS radar parameters. A model for generating speckle is reviewed and

applied successfully. The procedure for calculation of phase and phase without the earth component is also shown.

The architecture of the simulator was constructed to match the theoretical model as described in Chapter 4. Successful operation of the program requires an understanding of the input files and file formats, and the desired output images, thus a manual is provided.

The overall simulation process is evaluated by comparing the simulated to actual images including the expected statistics. It was confirmed that even a geometry-only approach can produce very accurate power and phase images, though further enhanced by specific radiometric terrain information in the form of a terrain-type specific backscatter model for vegetated areas. The statistics of the images are used to evaluate the speckle application routine. The simulated phase images exhibit the uniform distribution as expected. The complex interferogram magnitude images show an almost exponential distribution, which was deemed suitable for the purposes of modelling the amount of disarray that can be expected when speckle is applied to the clean radar cross section images. The coherence images routinely over-estimate the values seen in the actual images. This is most likely due to a wrong assumption of the user-estimated terrain type correlation levels or the inapplication of the decaying signal to noise ratio over the swath of the image. The ramifications of the over-estimated coherence level results in phase images with the fringes being less eroded than actually would occur, although the power images do not suffer as much.

The simulator excels at providing a simple yet powerful tool for:

- Predicting realistic backscatter, power, phase and coherence images
- Investigating the effects of interferometric configurations.
- Accurately predicting the imaged area's content, layover and shadow regions, given a specific antenna geometry.
- Demonstrating the process of phase production from absolute terrain phase to wrapped terrain phase to wrapped terrain phase without the earth component.
- Demonstrating the relationship between coherence value and overall noisiness of image.

Areas for improvement for the simulator and estimated dificulty levels include:

- Extension of the flight path model to one in which a few points are defined in (*latitude*, *longitude*, *height*) coordinates which the simulator interpolates a to smooth curve. Although not a difficult change, this would involve a major revision in the subroutine which is now the bulk of the program.

- Application of a radar transfer function that takes into account the limited bandwidth of the receiver. This would be a relatively simple process, taking the Fourier transform of the data, multiplying by a function modelling the limited bandwidth, and inverse Fourier transforming the data.

- Improving the interpolation procedure needed when the DEM spacing does not equal that of the desired slant range spacing. The spatial domain interpolation procedures offered by the IDL software have been less than perfect, frequency domain methods may prove more acceptable.

- Coding a graphical user interface to make the operation more user-friendly and allow for the user to view the images during the simulation process.

Appendix A

Gallery of Simulated Images

For each of the simulated regions; Cape Peninsula - North, Cape Peninsula - South, Cedarberg Mountains, Katse Region, the following full resolution simulated images will be included in pairs, as follows. The simulation parameters are identical to the ones outlined in Chapter 5.

- Image Pair #1
  - **Ground range DEM**: DEM in ground range coordinates representing increasing height with lighter greyscale pixel values, filename: DEM_subset_gr.
  - **Slant range DEM**: DEM in slant range coordinates, again with increasing height denoted with lighter greyscale pixel values, filename: DEM_subset.
- Image Pair #2
  - **RCS**: radar cross section with area effect, filename: rcs.
  - **Power**: power image, filename: complex_interg_mag.
- Image Pair #3
  - **Baseline coherence**: coherence due to geometrical baseline, scaled from 0 (black) to 1 (white), filename: coh_baseline.
  - **Temporal coherence**: coherence due to temporal decorrelation, filename: coh_time.

- Image Pair #4
  - **Coherence:** total coherence, filename: coh.
  - **Layover:** layover map, defined as black: 0 solved points, grey: 1 solved point, white: 2 or more solved points, filename: layover.
- Image Pair #5
  - **Clean phase:** clean phase with earth component, filename: phs_ terrain_ wrap_clean.
  - **Clean flattened phase:** clean phase without earth component, filename: phs_terrain_wrap_clean_flat.
- Image Pair #6
  - **Noisy phase:** noisy phase with earth component, filename: phs_ terrain_ wrap_noisy.
  - **Noisy flattened phase:** noisy phase without earth component, filename: phs_terrain_wrap_noisy_flat.

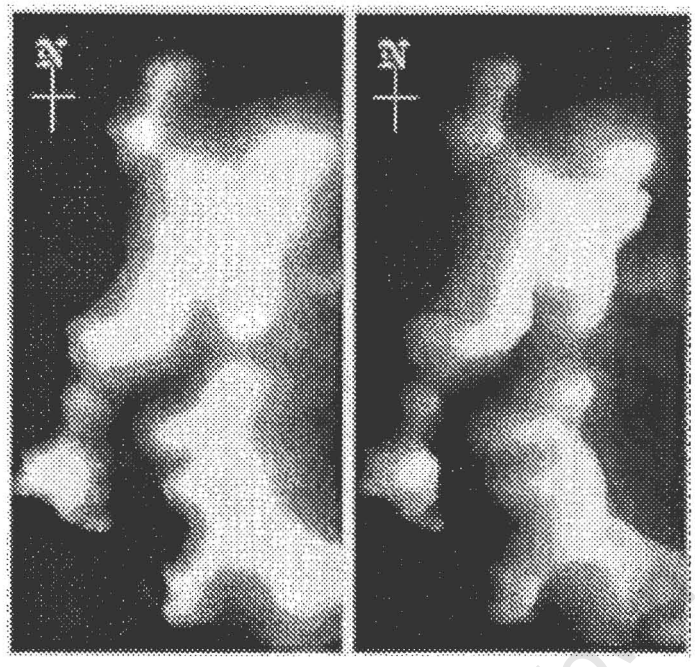

Ground range DEM (left), slant range DEM (right) images of northern Cape Peninsula simulation.

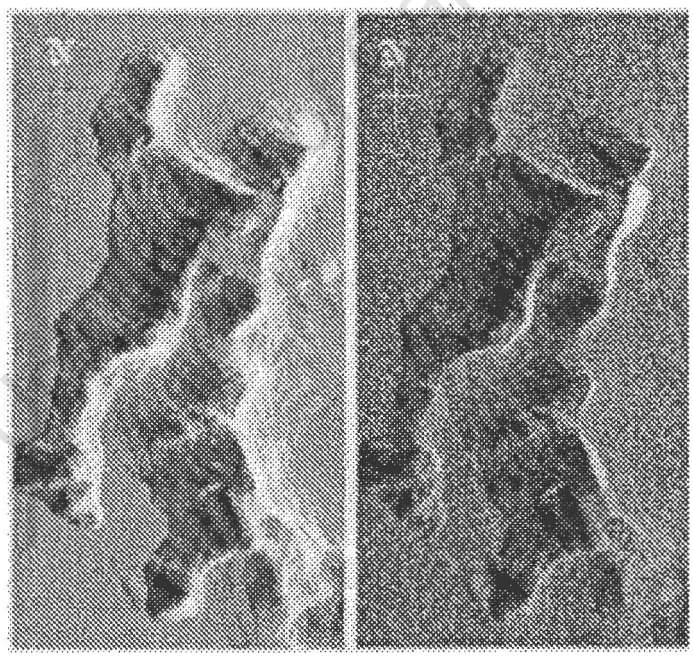

Radar cross section (left), power (right) images of northern Cape Peninsula simulation.

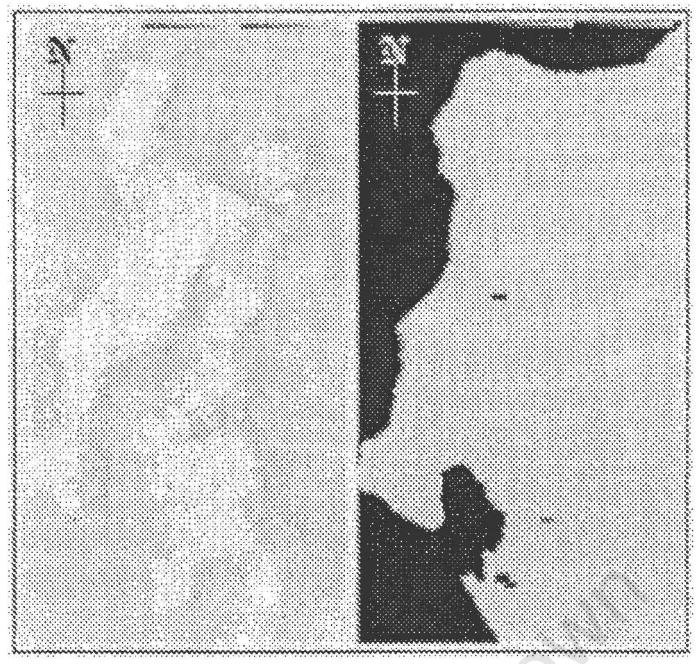

Baseline coherence (left), temporal coherence (right), images of northern Cape Peninsula simulation.

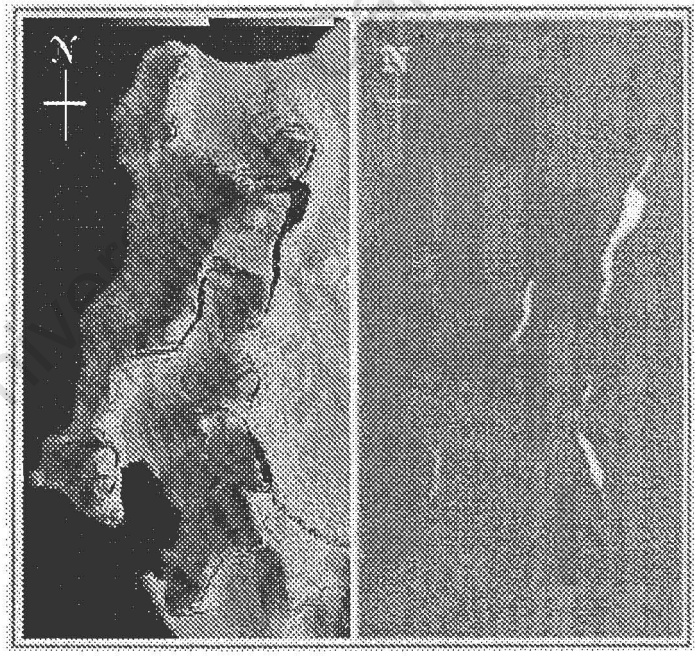

Coherence with SNR model applied (left), layover (right) images of northern Cape Peninsula simulation.

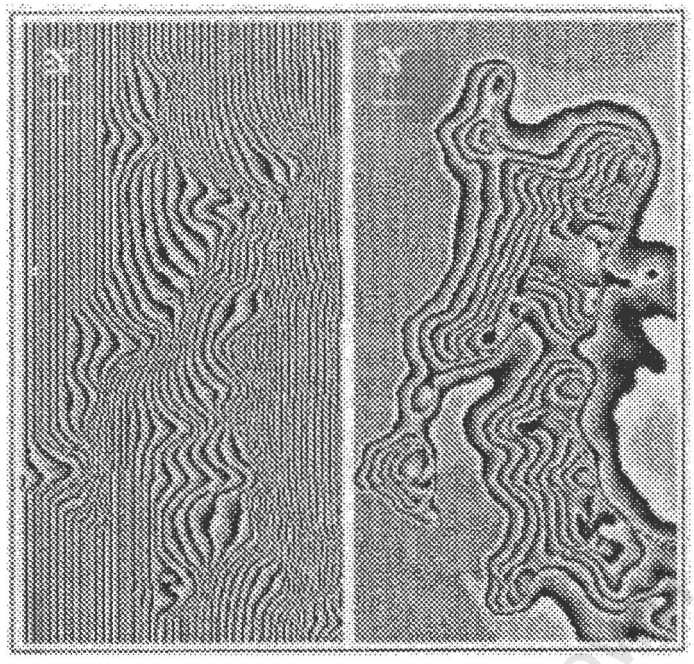

Clean phase (left), clean flattened phase (right) images of northern Cape Peninsula simulation.

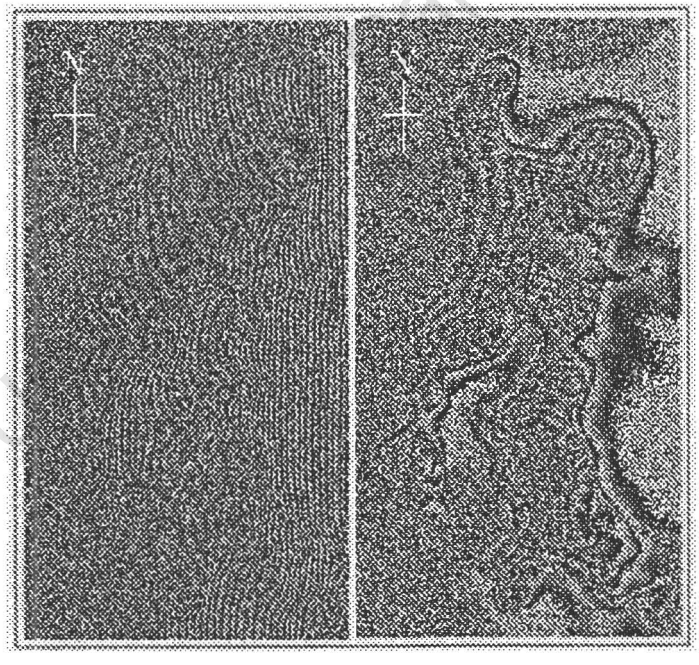

Noisy phase with SNR noise model (left), noisy flattened phase (right) images of northern Cape Peninsula simulation.

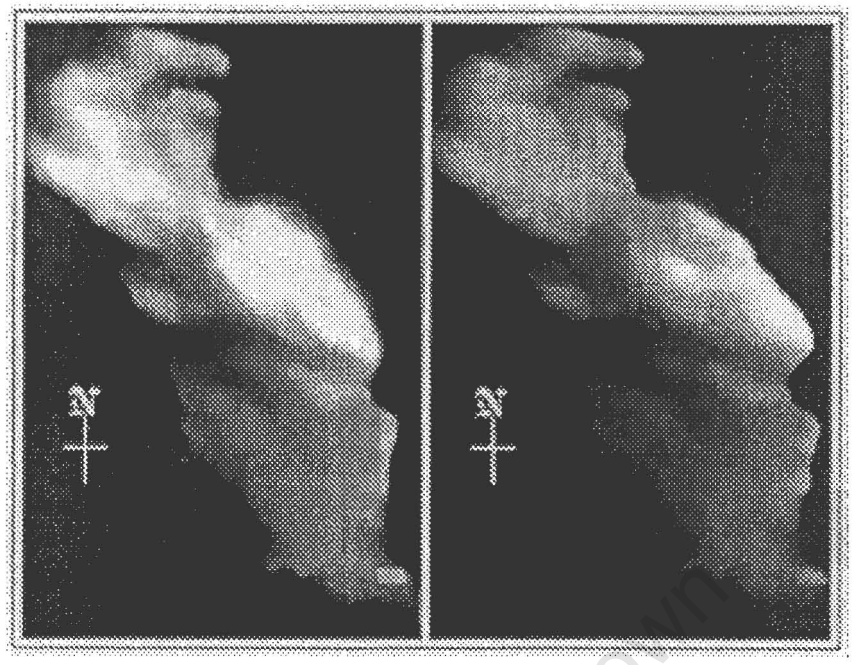

Ground range DEM (left), slant range DEM (right) images of southern Cape Peninsula simulation.

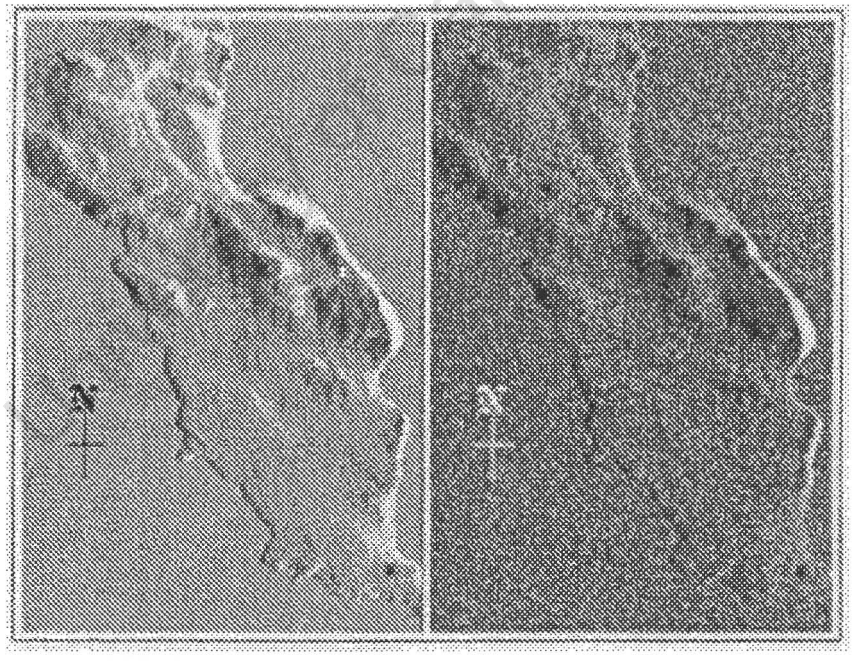

Radar cross section (left), power (right) images of southern Cape Peninsula simulation.

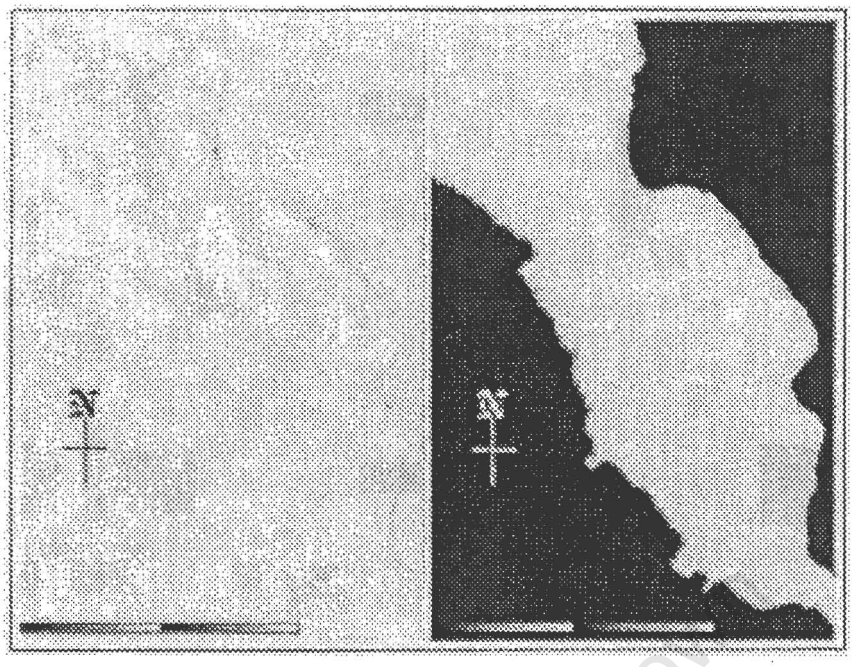

Baseline coherence (left), temporal coherence (right) images of southern Cape Peninsula simulation.

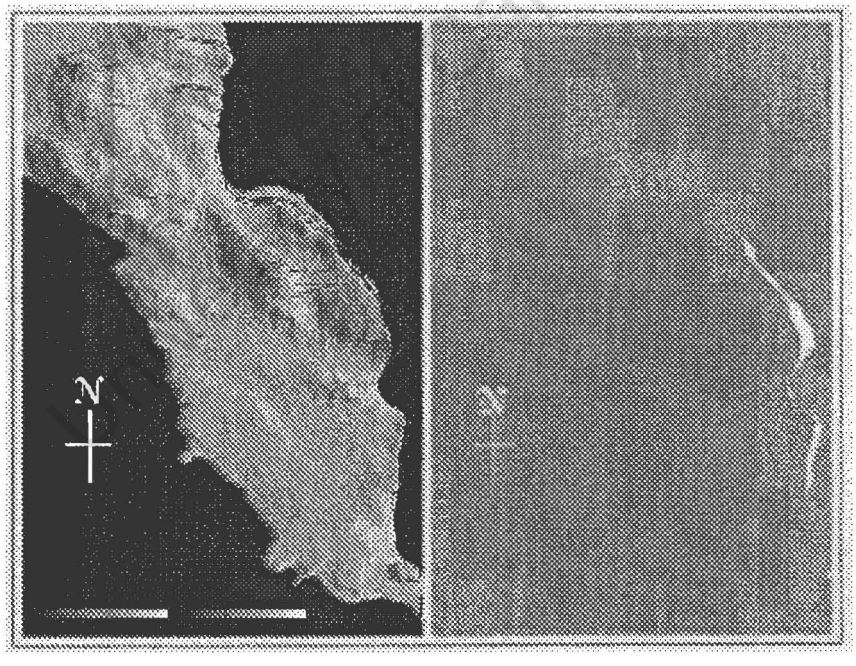

Coherence with SNR noise model (left), layover (right) images of southern Cape Peninsula simulation.

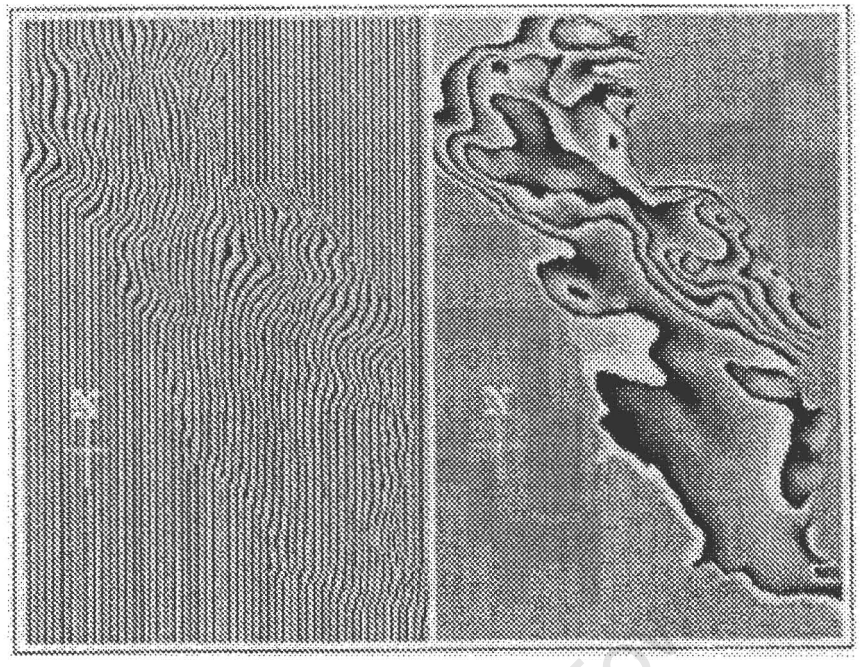

Clean phase (left), clean flattened phase (right) images of southern Cape Peninsula simulation.

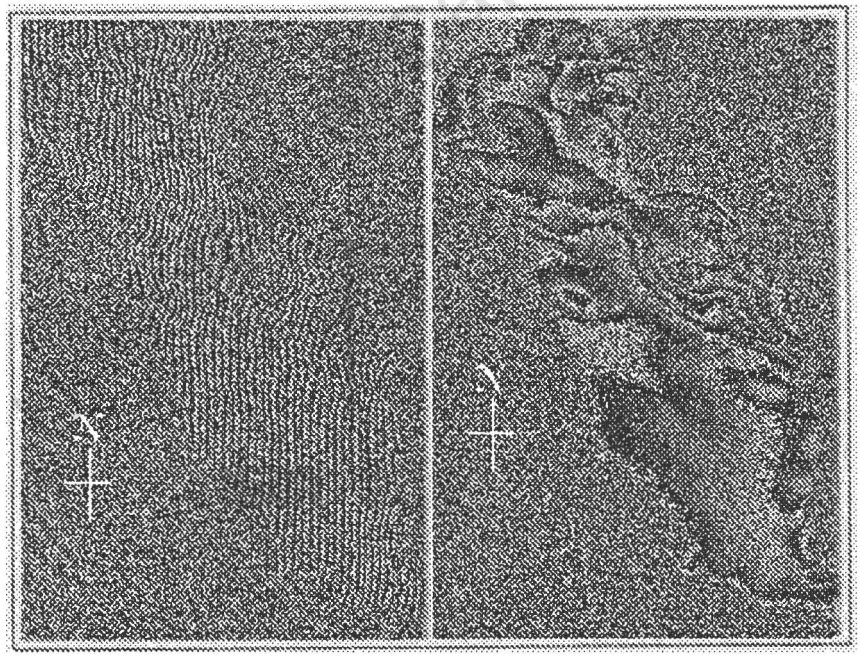

Noisy phase with SNR noise model (left), noisy flattened phase (right) images of southern Cape Peninsula simulation.

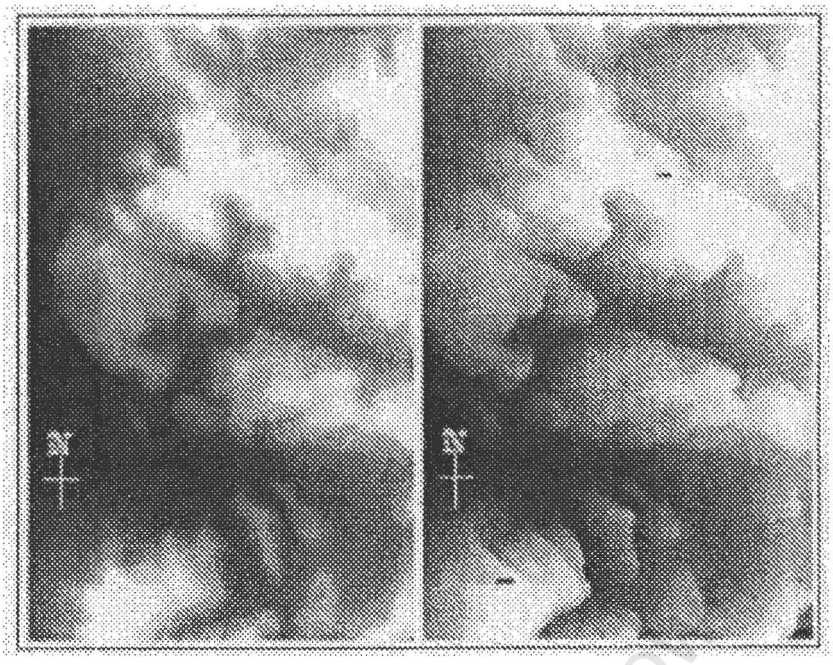

Ground range DEM (left), slant range DEM (right) images of Cedarberg Mountains simulation.

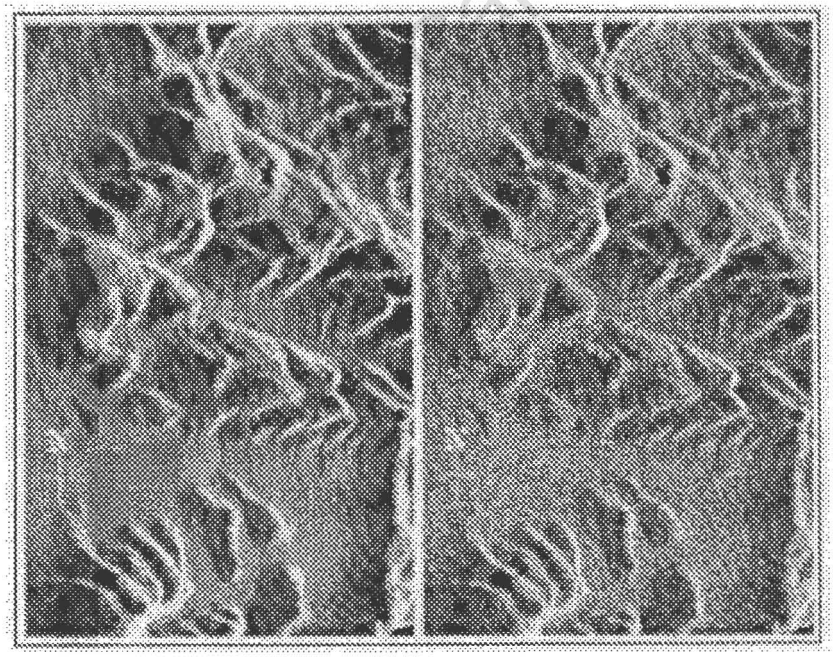

Radar cross section (left), magnitude of the complex interferogram (right) images of Cedarburg Mountains simulation.

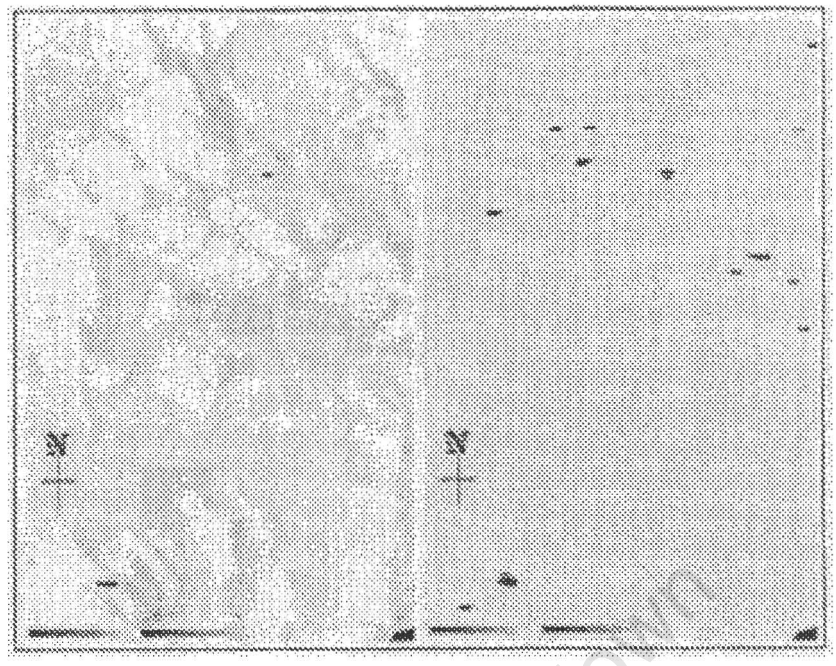

Baseline coherence (left), temporal coherence (right) images of Cedarburg Mountains simulation.

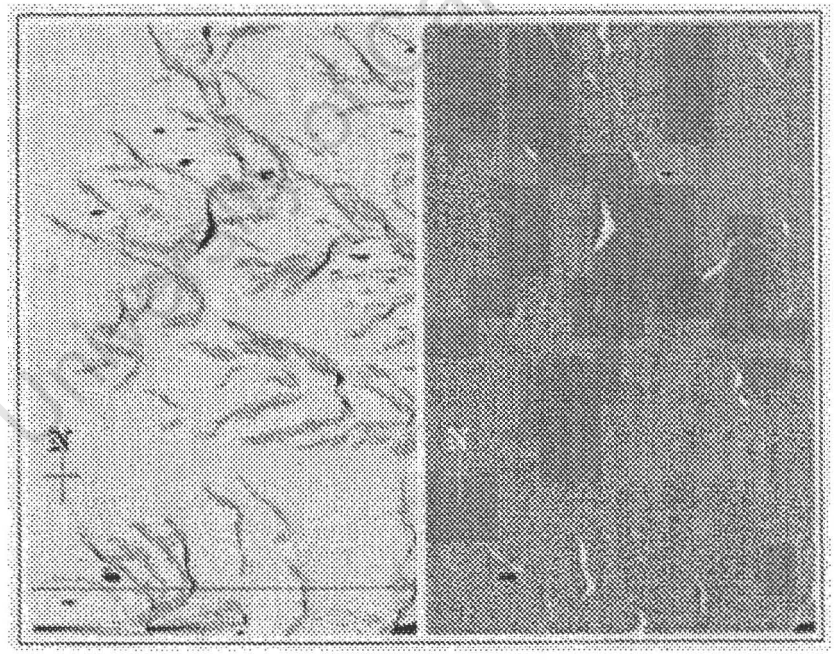

Coherence without SNR noise model (left), layover (right) images of Cedarburg Mountains simulation.

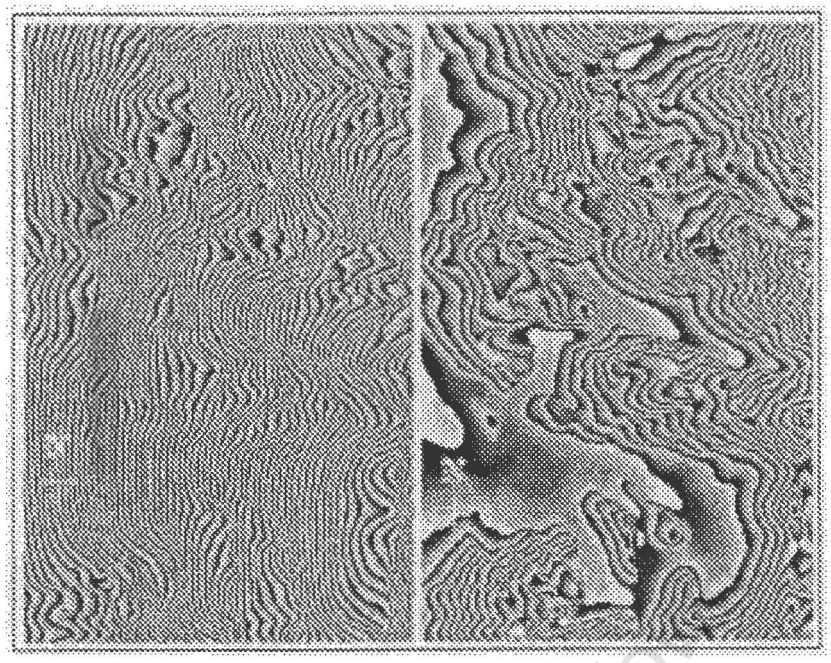

Clean phase (left), clean flattened phase (right) images of Cedarberg Mountains simulation.

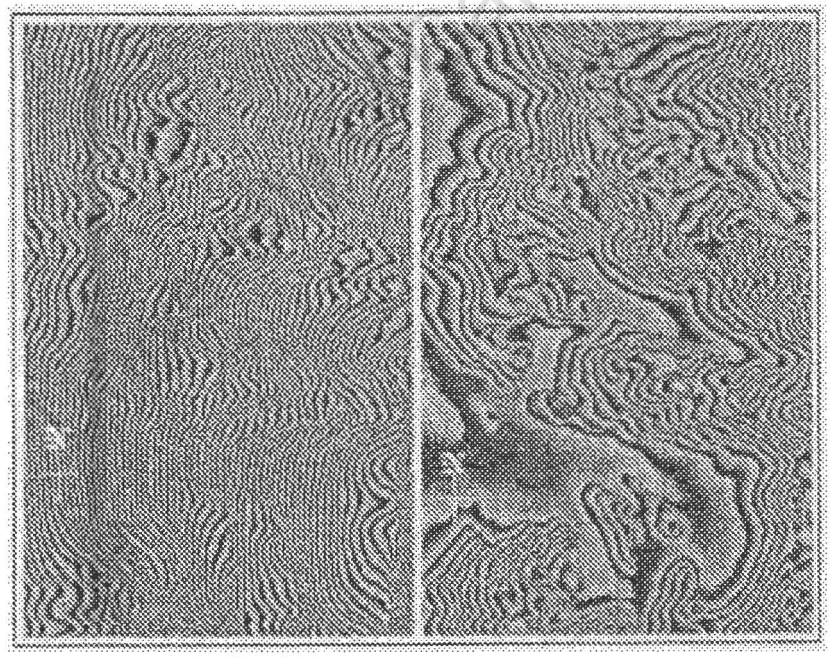

Noisy phase without SNR noise model (left), noisy flattened phase (right) images of Cedarberg Mountains simulation.

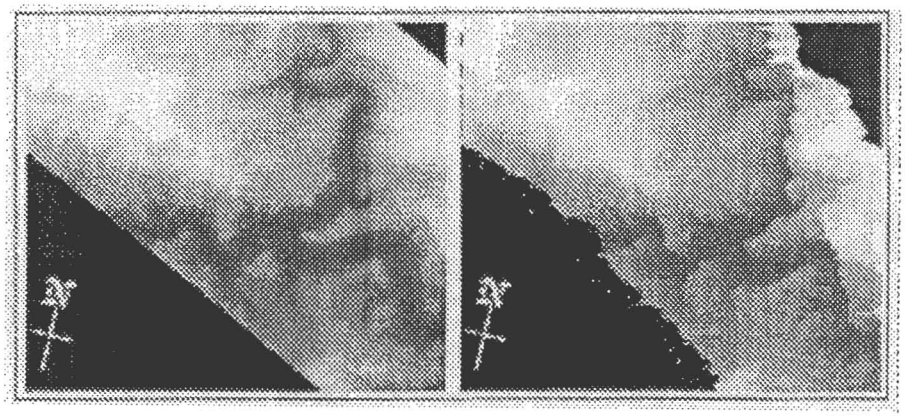

Ground range DEM (left), slant range DEM (right) images of Katse simulation.

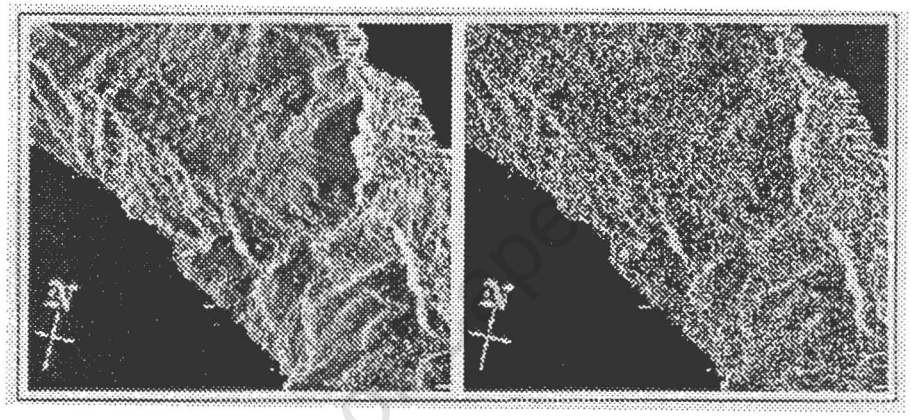

Radar cross section (left), power (right) images of Katse simulation.

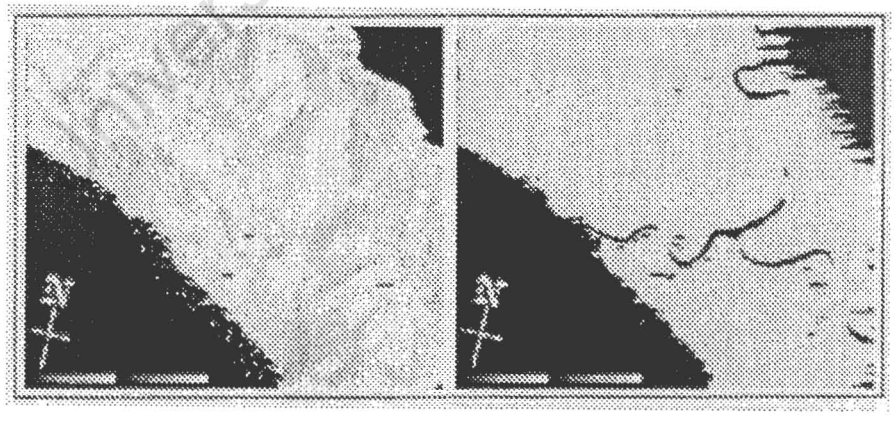

Baseline coherence (left), temporal coherence (right) images of Katse simulation.

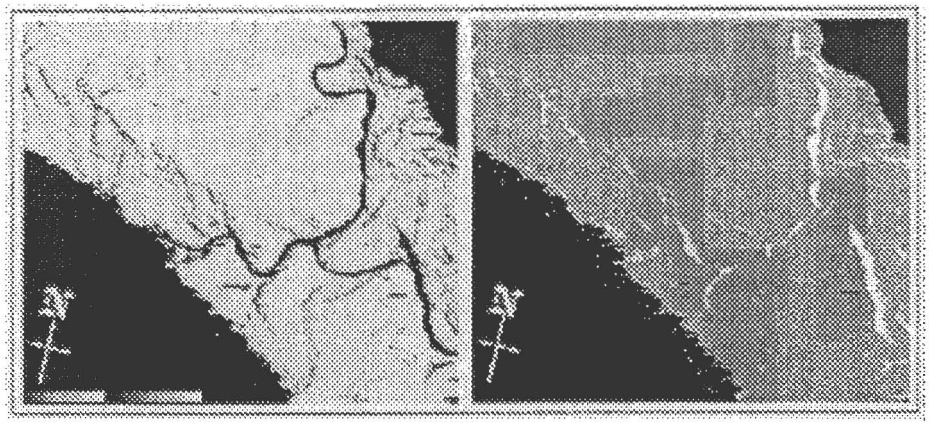

Coherence without SNR noise model (left), layover (right) images of Katse simuation.

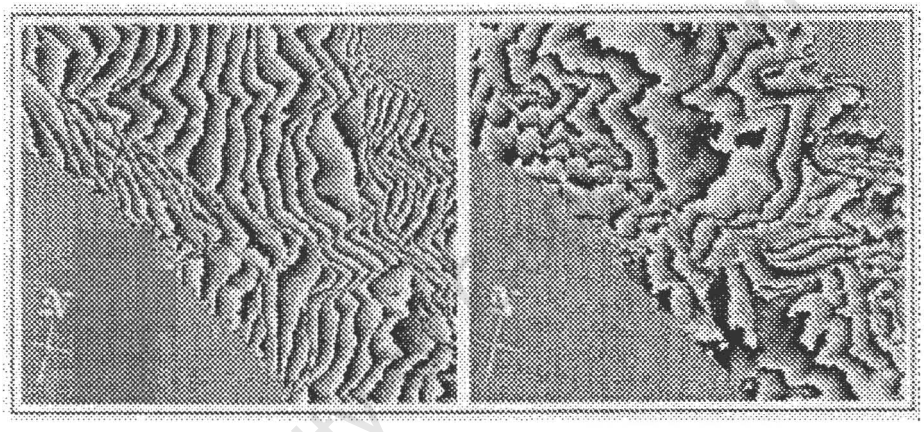

Clean phase (left), clean flattened phase (right) images of Katse simulation.

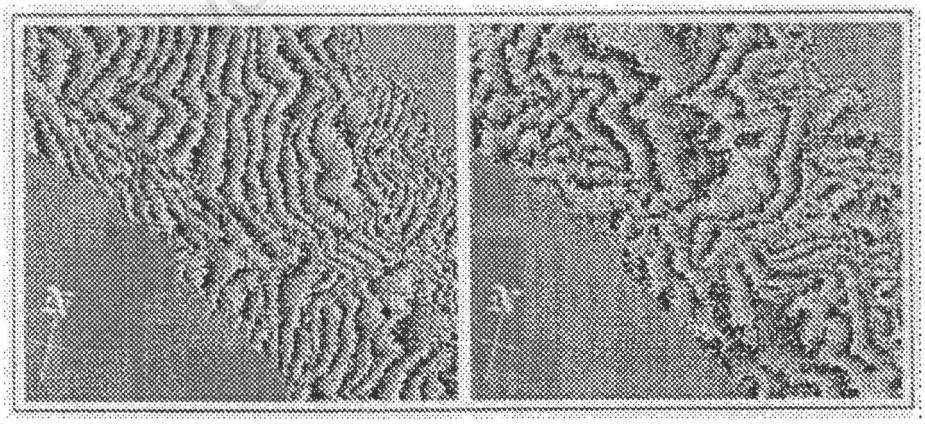

Noisy phase without SNR noise model (left), noisy flattened phase (right) images of Katse simulation.

Appendix B

Simulator Input Parameter File Examples

Samples of the two types of input parameter files, INPUT_PARAMS_TYPE1.PRO and INPUT_PARAMS_TYPE2.PRO are given, with the changeable parameters marked in bold face type.


```
PRO INPUT_PARAMS_TYPE1, STARTUP_PARAMS
startup_params.r_sp = 7.9050 * 1.
startup_params.az_sp = 4.4048 * 5.
startup_params.row_subset = [0,499]
startup_params.rownum = 100
startup_params.ant1_height = 796000.
startup_params.ant2_height = 796000.
startup_params.rot_angle = 0.
startup_params.rot_pixel_x = -1
startup_params.rot_pixel_y = -1
startup_params.h_baseline = 100.
startup_params.bandwidth = 15.E6
startup_params.lambda = .0566
startup_params.snr_sar_spec = 20.
startup_params.r_spec = 864000.
startup_params.rcs_spec = 10.
startup_params.coh_window = 3. ; must be 2 or greater...
```

```
startup_params.coh_scale = 1
startup_params.coh_time_scale = 1
startup_params.coh_baseline_scale = 1
startup_params.logfile_name = '/MSc_Thesis/InSIM/
output/Cape_Pen/log.txt'
startup_params.output_dir = '/MSc_Thesis/InSIM/
output/Cape_Pen/'
startup_params.code_dir = '/MSc_Thesis/InSIM/code/'
startup_params.rnear = 850000.
startup_params.r_samples = 4000
; choosing which output files to write to disk:
; "0" for no, "1" for yes
; ================================================
; complex coherence, magnitude, slant range:
startup_params.OP_0 = 1
; terrain phase, wrapped, clean, with earth component, slant
range:
startup_params.OP_1 = 1
; terrain phase, wrapped, clean, without earth component, slant
range:
startup_params.OP_2 = 1
; geoid absolute phase, slant range:
startup_params.OP_3 = 0
; geoid wrapped phase, slant range:
startup_params.OP_4 = 1
; terrain absolute phase, slant range:
startup_params.OP_5 = 1
; binary shadow map, slant range:
startup_params.OP_6 = 1
; layover map, slant range:
startup_params.OP_7 = 1
; single look complex (SLC) image from antenna 1, slant range:
startup_params.OP_8 = 0
; single look complex (SLC) image from antenna 2, slant range:
startup_params.OP_9 = 0
; complex interferogram, magnitude, slant range:
```

```
startup_params.OP_10 = 1
; terrain phase, wrapped, with noise, slant range:
startup_params.OP_11 = 1
; terrain phase, wrapped, flattened, with noise, slant range:
startup_params.OP_12 = 1
; single look complex (SLC image) from antenna 1, flattened, slant
range:
startup_params.OP_13 = 0
; RCS calibrated values, slant range:
startup_params.OP_14 = 1
; RCS values without area effect, slant range:
startup_params.OP_15 = 1
; DEM subset of area used, ground range:
startup_params.OP_16 = 1
; DEM subset of area used, slant range:
startup_params.OP_17 = 1
; coherence factor due to changes over time, slant range:
startup_params.OP_18 = 1
; coherence factor due to baseline (or geometric coherence), slant
range:
startup_params.OP_19 = 1
; coherence factor due to SNR
startup_params.OP_20 = 1
PRO INPUT_PARAMS_TYPE1, STARTUP_PARAMS
startup_params.code_dir = '/MSc_Thesis/InSIM/code/'
startup_params.rnear = 850000.
startup_params.r_samples = 4000
; choosing which output files to write to disk:
; "0" for no, "1" for yes
; ================================
; complex coherence, magnitude, slant range:
startup_params.OP_0 = 1
; terrain phase, wrapped, clean, with earth, slant range:
startup_params.OP_1 = 1
; terrain phase, wrapped, clean, without earth, slant range:
startup_params.OP_2 = 1
```

; geoid absolute phase, slant range:
startup_params.OP_3 = 0
; geoid wrapped phase, slant range:
startup_params.OP_4 = 1
; terrain absolute phase, slant range:
startup_params.OP_5 = 1
; binary shadow map, slant range:
startup_params.OP_6 = 1
; layover map, slant range:
startup_params.OP_7 = 1
; SLC image from antenna 1, slant range:
startup_params.OP_8 = 0
; SLC image from antenna 2, slant range:
startup_params.OP_9 = 0
; complex interferogram, magnitude, slant range:
startup_params.OP_10 = 1
; terrain phase, wrapped, with noise, slant range:
startup_params.OP_11 = 1
; terrain phase, wrapped, flattened, with noise, slant range:
startup_params.OP_12 = 1
; SLC from antenna 1, flattened, slant range:
startup_params.OP_13 = 0
; RCS calibrated values, slant range:
startup_params.OP_14 = 1
; RCS values without area effect, slant range:
startup_params.OP_15 = 1
; DEM subset of area used, ground range:
startup_params.OP_16 = 1
; DEM subset of area used, slant range:
startup_params.OP_17 = 1
; coherence factor due to changes over time, slant range:
startup_params.OP_18 = 1
; coherence factor due to baseline, slant range:
startup_params.OP_19 = 1
; coherence factor due to SNR
startup_params.OP_20 = 1

```
return
end


PRO INPUT_PARAMS_TYPE2, STARTUP_PARAMS
startup_params.r_sp = 7.905000 * 1.
startup_params.az_sp = 4.048000 * 5.
startup_params.row_subset = [0,549]
startup_params.rownum = 175
startup_params.ant1_height = 796000.
startup_params.ant2_height = 796000.
startup_params.rot_angle = 168.
startup_params.rot_pixel_x = -1
startup_params.rot_pixel_y = -1
startup_params.h_baseline = 100.
startup_params.bandwidth = 15.E6
startup_params.lambda = 0.0566
startup_params.snr_sar_spec = 20.
startup_params.r_spec = 864000.
startup_params.rcs_spec = 10.
startup_params.coh_window = 0
startup_params.coh_scale = 1
startup_params.coh_time_scale = 1
startup_params.coh_baseline_scale = 1
startup_params.logfile_name = '/MSc_Thesis/InSIM/
output/Cape_Pen2/log.txt'
startup_params.output_dir = '/MSc_Thesis/InSIM/
output/Cape_Pen2/'
startup_params.code_dir = '/MSc_Thesis/InSIM/code/'
startup_params.theta_mid = 23.
startup_params.yswath = 25000.
; choosing which output files to write to disk:
; "0" for no, "1" for yes
; ================================
```

; complex coherence, magnitude, slant range:
startup_params.OP_0 = 1
; terrain phase, wrapped, clean, with earth, slant range:
startup_params.OP_1 = 1
; terrain phase, wrapped, clean, without earth, slant range:
startup_params.OP_2 = 1
; geoid absolute phase, slant range:
startup_params.OP_3 = 1
; geoid wrapped phase, slant range:
startup_params.OP_4 = 1
; terrain absolute phase, slant range:
startup_params.OP_5 = 1
; binary shadow map, slant range:
startup_params.OP_6 = 1
; layover map, slant range:
startup_params.OP_7 = 1
; SLC image from antenna 1, slant range:
startup_params.OP_8 = 1
; SLC image from antenna 2, slant range:
startup_params.OP_9 = 1
; complex interferogram, magnitude, slant range:
startup_params.OP_10 = 1
; terrain phase, wrapped, with noise, slant range:
startup_params.OP_11 = 1
; terrain phase, wrapped, flattened, with noise, slant range:
startup_params.OP_12 = 1
; SLC from antenna 1, flattened, slant range:
startup_params.OP_13 = 1
; RCS calibrated values, slant range:
startup_params.OP_14 = 1
; RCS values without area effect, slant range:
startup_params.OP_15 = 1
; DEM subset of area used, ground range:
startup_params.OP_16 = 1
; DEM subset of area used, slant range:
startup_params.OP_17 = 1

```
; coherence factor due to changes over time, slant range:
startup_params.OP_18 = 1
; coherence factor due to baseline, slant range:
startup_params.OP_19 = 1
; coherence factor due to SNR
startup_params.OP_20 = 1
return
end
```

Appendix C

Sample Log File

The simulator produces an ASCII text log file named log.txt which captures all relevant simulation parameters, statistics, timing tests and possible errors.


```
**************************************************
INTERFEROMETRIC SAR SIMULATOR
**************************************************
University of Cape Town
Electrical Engineering, Radar Remote Sensing Group
L.S. Wray December 1999
**************************************************
SIMULATION STARTED: Thu Sep 28 16:46:59 2000
Datafile name: dem_katse.dat
Program code located in: /MSc_Thesis/InSIM/code/
Program input files located in : C:/MSc_Thesis/InSIM/input/Katse/
Program output files located in : /MSc_Thesis/InSIM/output/Katse/
==================================================
DIGITAL ELEVATION MODEL:
*** DEM filename: dem_katse
```

*** Endian: 0:386, 1:Sun 0

*** 510 rows x 544 columns

*** Row pixel dimension (m): 25

*** Column pixel dimension (m): 25

*** Reading rows (indexed from 0): 0 to 509

*** Diagnostic Plotting Window showing row: 205

*** DEM rotation angle (degrees): 5.0

*** DEM rotation centre point, (x,y): -1, -1

if (x,y) = (-1,-1), rotation is about the centre of DEM

*** Width of ground range coverage (m): 13600.00

==========

ASSOCIATED MASKS:

DEM Validity Mask:

*** DEM validity filename: dem_katse_validity.msk

*** Endian: 0:386, 1:Sun 0

*** Validity mask contents:

*** min: 0.0

*** max: 1.0

DEM Terrain Type Files:

*** DEM terrain type filename: dem_katse_terrain.msk

*** Endian: 0:386, 1:Sun 0

*** Terrain mask contents:

*** min: 0.0

*** max: 1.0

*** DEM terrain type definitions filename: dem_katse_terrain_defn.txt

*** Mask_gamma_time (coherence due to time) contents:

*** Type: 0 coherence = 0.9000

*** Type: 1 coherence = 0.1000

*** Sigma Nought Equations:

*** TYPE SIGMA_NOUGHT(theta_inc) equation

*** 0 sigma_n = -88.5930 + 99.0000 * exp(- 0.3260 *theta_inc) +

9.5740*cos(1.9690*theta_inc + -3.1420)

*** 1 sigma_n = -88.5930 + 99.0000 * exp(- 0.3260 *theta_inc) +

9.5740*cos(1.9690*theta_inc + -3.1420)

==========

Antenna information:

*** Antenna 1 height(m): 796000.00

*** Antenna 1 is master (reference) antenna

*** azimuth (m): 0.00

*** range (m): 0.00

*** Antenna 2 height(m): 796000.00

*** Antenna 2 is slave antenna

*** azimuth (m): 0.00

*** range (m): 100.00

*** Horizontal Baseline (m): 100.00

*** Vertical Baseline (m): 0.00

==========

Ground Range Distances to Swath:

*** Ground range from nadir to near swath (m): 330881.94

*** Ground range from nadir to mid swath (m): 337881.94

*** Ground range from nadir to far swath (m): 344881.94

Slant Range Distances to Swath:

*** Slant range from antenna 1 to near swath (m): 862031.81

*** Slant range from antenna 1 to mid swath (m): 864742.81

*** Slant range from antenna 1 to far swath (m): 867501.94

Incident Angles across Swath:

*** Incident angle to near swath (degrees): 22.57

*** Incident angle to mid swath (degrees): 23.00

*** Incident angle to near swath (degrees): 23.43

Swath Widths:

*** Width of ground range swath (m): 14000.00

*** Width of slant range swath (m): 5470.13

Receiver Parameters:

*** Receiver Bandwidth (MHz): 15.0000

*** Observing Wavelength (m): 0.0566

*** Simulated range spacing (m): 7.9050

*** Simulated azimuth spacing (m): 20.2400

Receiver Noise Model (SNR) Parameters:

*** Slant range R_spec for SNR value (m): 864000.0000

*** SNR at slant range R_spec (linear, not dB): 20.0000

*** RCS at slant range R_spec: 10.0000

==========

Selected Files for Output

*** /MSc_Thesis/InSIM/output/Katse/coh

*** /MSc_Thesis/InSIM/output/Katse/phs_terrain_wrap_clean

*** /MSc_Thesis/InSIM/output/Katse/phs_terrain_wrap_clean_flat

*** /MSc_Thesis/InSIM/output/Katse/shadow

*** /MSc_Thesis/InSIM/output/Katse/layover

*** /MSc_Thesis/InSIM/output/Katse/slc1

*** /MSc_Thesis/InSIM/output/Katse/complex_interf_mag

*** /MSc_Thesis/InSIM/output/Katse/phs_terrain_wrap_noisy

*** /MSc_Thesis/InSIM/output/Katse/phs_terrain_wrap_noisy_flat

*** /MSc_Thesis/InSIM/output/Katse/RCS

*** /MSc_Thesis/InSIM/output/Katse/RCS_per_area

*** /MSc_Thesis/InSIM/output/Katse/DEM_subset_gr

*** /MSc_Thesis/InSIM/output/Katse/DEM_subset

*** /MSc_Thesis/InSIM/output/Katse/coh_time

*** /MSc_Thesis/InSIM/output/Katse/coh_baseline

*** /MSc_Thesis/InSIM/output/Katse/coh_snr

Temporary Files:

CODE: 0 1 2 3 4 5 6 7 8 9 10 11 12 13 14 15 16 1 18 19 20

User Spec: 1 1 1 0 0 0 1 1 1 0 1 1 1 0 1 1 1 1 1 1 1

Temp Files:1 1 1 1 0 0 1 1 1 1 1 1 1 1 1 1 1 1 1 1 1

Number of slant range samples: 692

Time to end of Solver Module: 4.1908333 minutes

Resampling to desired slant range pixel sizes

1 x 1.2352in range x az

*** ADD_SPECKLE.PRO ROUTINE RUN ***

Time to end of Add_Speckle Module: 4.3821667 minutes

==========

Output File Information

Note: All slant range image statistics have been computed

only for the region in which valid data exists.

filename: /MSc_Thesis/InSIM/output/Katse/coh and *.txt

** stats: mean: 0.604189

** min, max, stdev: 0.000000 0.972248 0.261704

filename: /MSc_Thesis/InSIM/output/Katse/phs_terrain_wrap_clean and *.txt

** stats: mean: -0.0217724

** min, max, stdev: -3.14159 3.14158 1.78023

filename: /MSc_Thesis/InSIM/output/Katse/phs_terrain_wrap_clean_flat and *.txt

** stats: mean: -0.0555591

** min, max, stdev: -3.14159 3.14159 1.82445

filename: /MSc_Thesis/InSIM/output/Katse/shadow and *.txt

** stats: mean: 0.000000

** min, max, stdev: 0 0 0.000000

filename: /MSc_Thesis/InSIM/output/Katse/layover and *.txt

** stats: mean: 1.14253

** min, max, stdev: 1 11 0.559811

filename: /MSc_Thesis/InSIM/output/Katse/slc1 and *.txt

** MAGNITUDE: stats: mean: 4.19718

** min, max, stdev: 0.000000 54.9873 3.66244

** PHASE: stats: mean: 0.00394471

** min, max, stdev: -3.14155 3.14159 1.81357

filename: /MSc_Thesis/InSIM/output/Katse/complex_interf_mag and *.txt

** stats: mean: 26.1734

** min, max, stdev: 0.000000 1872.83 56.3453

filename: /MSc_Thesis/InSIM/output/Katse/phs_terrain_wrap_noisy and *.txt

** stats: mean: -0.000245537

** min, max, stdev: -3.14151 3.14159 1.81198

filename: /MSc_Thesis/InSIM/output/Katse/phs_terrain_wrap_noisy_flat and *.txt

** stats: mean: -0.00345672

** min, max, stdev: -3.14156 3.14159 0.853252

filename: /MSc_Thesis/InSIM/output/Katse/RCS and *.txt

** stats: mean: 31.0649

** min, max, stdev: 0.000000 857.808 51.3099

filename: /MSc_Thesis/InSIM/output/Katse/RCS_per_area and *.txt

** stats: mean: 0.194161

** min, max, stdev: 0.000000 5.36139 0.320692

filename: /MSc_Thesis/InSIM/output/Katse/DEM_subset_gr and *.txt

** stats: mean: 2677.07

** min, max, stdev: 1.64792e-005 2924.36 384.560

filename: /MSc_Thesis/InSIM/output/Katse/DEM_subset and *.txt

** stats: mean: 2390.57

** min, max, stdev: 1883.07 2973.71 362.236

filename: /MSc_Thesis/InSIM/output/Katse/coh_time and *.txt

** stats: mean: 0.809387

** min, max, stdev: 0.000000 1.00000 0.256908

filename: /MSc_Thesis/InSIM/output/Katse/coh_baseline and *.txt

** stats: mean: 0.927087

** min, max, stdev: 0.000000 1.00000 0.0847928

filename: /MSc_Thesis/InSIM/output/Katse/coh_snr and *.txt

** stats: mean: 0.784211

** min, max, stdev: 0.000000 1.00000 0.286106

==========

SIMULATION ENDED AT Thu Sep 28 16:51:30 2000

SIMULATION LASTED 270.56000 Seconds

= 4.5093333 Minutes

= 0.075155556 Hours

==========

Appendix D

Listing of Program Source Code Files

The following is a listing of all program source code files. The arrangement is that of a program tree with the main program listed on the far left. Each subprogram called is noted as indented from the parent program.

INSIM.pro
    STARTUP.pro
    READ_DEM.pro
    SETUP_SR.pro
    SOLVER.pro
        SOLN.pro
        VALID_SLANT_SOLUTION.pro
        SCENE_COH.pro
            GEO_COH.pro
    RX_NOISE.pro
    GEOID_PHASE.pro
    PLOT_DIAGNOSTICS.pro
        MIN_NO_ZERO.pro
    PROCESSING.pro
        WRITE_ONE_FILE.pro
        READ_ONE_FILE.pro
    ADD_SPECKLE.pro

PROCESSING_TWO.pro
ADD_SCALE.pro
WRITE_ALL_HDRS.pro

Bibliography

[1] L. Alexander. The Planning of a South African Airborne Synthetic Aperture Radar Measuring Campaign. Master's thesis, University of Cape Town, Electrical Engineering Department, 1994.

[2] A. Amit. personal communication, 1999.

[3] R. Balmer and P. Hartl. Synthetic Aperture Radar Interferometry. *Inverse Problems*, 14:R1–R54, 1998.

[4] M. Bulmer. *Principles of Statistics.* General Publishing Company, Toronto, Ontario, 1979.

[5] C. Camporeale and G. Galati. Digital Computer Simulation of Synthetic Aperture Systems and Images. *European Transactions on Telecommunication and Related Technologies*, 2(3):343–352, 1991.

[6] J. Curlander and R. McDonough. *Synthetic Aperture Radar Systems and Signal Processing.* John Wiley and Sons, New York, 1991.

[7] G. Domik and F. Leberl. Image Based SAR product simulation. In *Proc. American Society of Photogrammetry and Remote Sensing*, pages 355–364, 53rd Annual Convention. Baltimore, MD, 1987.

[8] G. Doyle, A. Wilkinson, and M. Inggs. Contending with High Relief and Temporal Decorrelation in an InSAR Study of the Effects of Reservoir Loading. In *Proceedings of the International Geoscience and Remote Sensing Symposium (IGARSS)*, Hamburg, 1999.

[9] W. P. et al. The Geometry of the Radarscope. Technical Report 107, Ohio State University, Mapping and Charting Laboratory, 1950.

[10] G. Francheschetti, M. Migliaccio, and D. Riccio. On Ocean SAR Raw Signal Simulation. *IEEE Trans. on Geoscience and Remote Sensing*, 36(1):84–100, Jan. 1999.

[11] G. Francheschetti, M. Migliaccio, D. Riccio, and G. Schirinzi. SARAS: A Synthetic Aperture Radar (SAR) Raw Signal Simulator. *IEEE Trans. on Geoscience and Remote Sensing*, 30(1):110–123, Jan. 1992.

[12] M. Gelautz, H. Frick, J. Raggam, J. Burgstaller, and F. Leberl. SAR Image simulation and analysis of alpine terrain. *ISPRS Journal of Photogrammetry and Remote Sensing*, 53:17–38, 1998.

[13] R. Goldstein, H. Zebker, and C. Werner. Satellite radar interferometry: two dimensional phase unwrapping.

[14] B. Guindon. Development of a SAR data acquisition planning tool (SAR-PLAN) based on image simulation. *Int. J. Remote Sensing*, 14(2):333–344, 1993.

[15] F. M. Henderson and A. J. Lewis. *Principles and Applications of Imaging Radar*, volume 2 of *Manual of Remote Sensing*. John Wiley and Sons, New York, third edition, 1998.

[16] J. Holtzman, V. Frost, J. Abbott, and V. Kaupp. Radar Image Simulation. *IEEE Trans. on Geoscience and Remote Sensing*, 16(4):296–303, July 1978.

[17] H. Kimura and N. Kodaira. Simulation and comparison of JERS-1 and ERS-1 SAR images. In *Proceedings of the International Geoscience and Remote Sensing Symposium (IGARSS)*, number 4, pages 1774–1776, Tokyo, 1993.

[18] F. Leberl. *Radargrammetric Image Processing*. Artech House, Norwood, MA, 1990.

[19] G. Marconi. SAR simulation concept and tools. Final Report MTR 84/34, Marconi Research Centre, Chelmsford, Essex, UK, 1984.

[20] C. Oliver and S. Quegan. *Understanding Synthetic Aperture Radar Images*. Artech House Remote Sensing Library. Artech House, Norwood, MA, 1998.

[21] A. Papoulis. *Probability, Random Variables and Stochastic Processes*. McGraw-Hill, Singapore, 1984.

[22] S. Quegan. Interpolation and Sampling in SAR Images. *IEEE Trans. on Geoscience and Remote Sensing*, 28:641–646, 1990.

[23] H. Resnikoff. *The Illusion of Reality.* Springer-Verlag, New York, 1989.

[24] M. Skolnik. *Introduction to Radar Systems.* Artech House, Norwood, MA, second edition, 1981.

[25] R. Touzi, A. Lopes, J. Bruniquel, and P. Vachon. Coherence Estimation for SAR Imagery. *IEEE Trans. on Geoscience and Remote Sensing*, 37(1):135–150, Jan. 1999.

[26] F. Ulaby, R. Moore, and A. Fung. *Microwave Remote Sensing: Active and Passive*, volume 3 of *The Artech House Remote Sensing Library.* Artech House, Norwood, MA, 1986.

[27] F. T. Ulaby and M. C. Dobson. *Handbook of Radar Scattering Statistics for Terrain.* The Artech House Remote Sensing Library. Artech House, Norwood, MA, 1989.

[28] A. J. Wilkinson. personal communication, 1999.

[29] A. J. Wilkinson. *Techniques for 3-D surface reconstruction using synthetic aperture radar interferometry.* PhD dissertation, University of London, Department of Electronic Engineering, 1997.

[30] A. J. Wilkinson. Synthetic Aperture Radar Interferometry: A Model for the Joint Statistics in Layover Areas. In *COMSIG '98: Proceedings of the 1998 South African Symposium on Communications and Signal Processing*, pages 333–338, Cape Town, South Africa, 1998.

[31] W. Xu and B. Cumming. Simulator for Repeat-Pass Satelite InSAR Studies. In *Proceedings of the International Geoscience and Remote Sensing Symposium (IGARSS)*, pages 1704–1706, Singapore, 1997.

[32] H. A. Zebker and R. M. Goldstein. Topographic mapping from interferometric synthetic aperture radar observations. *Journal of Geophysical Research*, 91(B5):4993–4999, Apr. 1986.